UNIVERSITY OF BRASILIA

MECHANICAL ENGINEERING DEPARTMENT

MASTERS DISSERTATION

ANALYSIS AND ESTIMATION OF EXTENSION OF THE FUSION ZONE AND SUB-REGIONS OF THE HEAT AFFECTED ZONE THROUGH NEURAL NETWORKS IN WELD BEADS PRODUCED BY GMAW PROCESS

Author: Leandro Bruno Alves Caio

Supervisor: Prof. Alysson Martins Almeida Silva, PhD

Co-supervisor: Prof. Guillermo Alvarez Bestard, PhD

Brasilia/DF

2021

Leandro Bruno Alves Caio

Analysis and estimation of extension of the fusion zone and sub-regions of the heat affected zone through neural networks in weld beads produced by GMAW process

Dissertation submitted to the Graduate Program in Mechatronic Systems of the University of Brasilia, as a partial requirement to obtain the title of Master in Mechatronic Systems.

Research Field: Welding Metallurgy and Control
Supervisor: Prof. Alysson Martins Almeida Silva, PhD
Co-supervisor: Prof. Guillermo Alvarez Bestard, PhD

Brasilia
University of Brasilia
Department of Mechanical Engineering
2021

Faculdade de Tecnologia

DISSERTAÇÃO DE MESTRADO

Analysis and estimation of extension of the fusion zone and sub-regions of the heat affected zone through neural networks in weld beads produced by GMAW process

Leandro Bruno Alves Caio

Relatório submetido ao Departamento de Engenharia Mecatrônica como requisito parcial para obtenção do grau de Mestre em Sistemas Mecatrônicos

Banca Examinadora

Prof. Alysson Martins Almeida Silva, Orientador, PhD, ENM/UnB _____

Prof. Louriel Oliveira Vilarinho, Examinador Externo, PhD, FEMEC/UFU _____

Prof. José Alfredo Ruiz Vargas, Examinador Interno, PhD, ENE/UnB _____

Prof. Guilherme Caribé de Carvalho, Examinador Externo, PhD, ENM/UnB _____

Brasilia
University of Brasilia
Department of Mechanical Engineering
2021

I dedicate this work to my parents, to my wife Lais, to my family and to my friends for the patience and words of encouragement.

“Para o espírito científico, todo conhecimento é resposta a uma pergunta. Se não há pergunta, não pode haver conhecimento científico. Nada é evidente. Nada é gratuito. Tudo é construído.”

Gaston Bachelard

ACKNOWLEDGEMENTS

I would like to thank to my wife Lais Soares Vieira for all the understanding and encouragement and for supporting the experiments and carrying out the research.

To my parents, my family and my friends, who for their dedication provided me with this unique moment.

To professor Dr. Alysson Martins Almeida Silva for his friendship, opportunity, guidance and the trust he has placed.

To Professor Dr. Guillermo Alvarez Bestard for his friendship, guidance and help with the experiments carried out.

To the professors Dr. Edson Paulo da Silva, Dr. Guilherme Caribé de Carvalho and Dr. Jones Yudi Mori for the opportunity to use the equipment, for the help, guidance and encouragement.

To Rafael from the Geology department, for the characterization of the samples via X-ray diffraction and teachings on the use of the equipment.

To Bruno Felipe, Elina Mylen, and all the members of the GRACO group for their friendship, solidarity and moments of relaxation in the laboratory.

To FAPDF, CAPES and CNPQ for financial support.

To the Automation and Control Group (GRACO) and the Materials Laboratory (LABMAT) for technical support and availability of equipment for making samples and performing microscopy analysis.

CONTENTS

FIGURES INDEX

TABLES INDEX

ABBREVIATIONS LIST

ADALINE	-	Adaptive Linear Element
AF	-	Acicular ferrite
AISI	-	American Iron and Steel Institute
ANN	-	Artificial Neural Network
B	-	Bainite
BCC	-	Body-centered cubic
BCT	-	Body-centered tetragonal
BM	-	Base Metal
BR	-	Bayesian Regularization ANN training mode
CCT	-	Continuous Cooling Transformation
CGHAZ	-	Coarse-grained Heat Affected Zone
CTWD	-	Contact tip - workpiece distance
EBSD	-	Electron Backscattered Diffraction
EBW	-	Electron Beam Welding
FC	-	Aggregate ferrite-carbide
FCC	-	Face-centered cubic
FGHAZ	-	Fine-grained Heat Affected Zone
FS(A)	-	Ferrite with aligned second phase
FS(NA)	-	Ferrite with non-aligned second phase
FWHM	-	Full width at half maximum
FZ	-	Fusion Zone
GBF	-	Grain boundary ferrite
GMAW	-	Gas Metal Arc-Welding
GMAW-S	-	Gas metal arc-welding with short-circuit transfer
HAZ	-	Heat-Affected Zone
IHAZ	-	Intercritical Heat Affected Zone
IIW	-	International Welding Institute
KS	-	Kurdjumov–Sachs crystal growth orientation relationship
LBW	-	Laser Beam Welding
LM	-	Levenberg-Marquardt ANN training mode
M	-	Martensite

MA	-	Martensite-Austenite constituent
MAG	-	Metal Active Gas
MIG	-	Metal Inert Gas
NW	-	Nishiyama-Wasserman crystal growth orientation relationship
OM	-	Optical Microscopy
P	-	Pearlite
P(D)	-	Degenerate pearlite
PAW	-	Plasma Arc-Welding
PF	-	Primary ferrite
PF(G)	-	Grain boundary primary ferrite
SAE	-	Society of Automotive Engineers
SAW	-	Submerged Arc-Welding
SEM	-	Scanning Electron Microscopy
SHAZ	-	Subcritical Heat Affected Zone
SMAW	-	Shielded Metal Arc-Welding
TWI	-	The Welding Institute
WF	-	Widmanstatten ferrite
XRD	-	X-ray Diffraction

SYMBOLS LIST

a	-	Slope coeficient
ΔG	-	Free energy variation
ΔG^*	-	Critical free energy variation
ΔG_v	-	Volumetric free energy per volume unit
ΔH_f	-	Fusion latent heat
$\Delta t_{7/3}$	-	Cooling time from 700°C to 300°C
$\Delta t_{8/5}$	-	Cooling time from 800°C to 500°C
$\sum$	-	Transfer function in Artificial Neural Network
A_0	-	Area covered by plasma column
A_{eL}	-	Embryo-liquid surface área
B	-	Generic dataset B in a generic study universe
D_c	-	Diffusivity of carbon in iron
e_k	-	Network error
F_c	-	Fuzzy combination
G	-	Gibbs free energy
H	-	Enthalpy
H_T	-	Total welding energy
H_L	-	Heat input
$H_{T[fusion]}$	-	Thermal energy of the material in molten state
$H_{T[initial]}$	-	Initial thermal energy of the material
I	-	Current
I_w	-	Welding current
k	-	Thermal conductivity coeficient
L	-	Length of the weld joint
MSE	-	Mean squared error
m_w	-	Mass of the molten metal to form the weld bead
net_j	-	Net input in Artificial Neural Network
o_j	-	Activation output in Artificial Neural Networrk
E_P	-	Electromagnetic pinch force
P	-	Weld Bead penetration
P	-	Pearlite

P_W	-	Welding power intensity
Q	-	Amount of energy generated by the welding power source
R_A	-	Anode reaction force
R	-	Embryo radius
r*	-	Critical embryo radius
RMSE	-	Root of Mean Squared Error
S	-	Entropy
T	-	Temperature
T_0	-	Initial or preheating temperature
t_a	-	Thermographic área
t_b	-	Thermographic base
t_c	-	residence time
T_c	-	Critical temperature
T_f	-	Fusion temperature
T_p	-	Peak temperature
t_p	-	Thermographic peak
t_v	-	Thermographic volume
t_w	-	Thermographic width
U	-	Voltage
U_G	-	Generic study universe
u_G	-	Colection of U_G objects
U_w	-	Welding voltage
V	-	Volumetric free energy per volume unit
w_f	-	Wire feed speed
w_{nj}	-	Weight relative to a x_n input in Artificial Neural Network
w_s	-	Travel speed
x	-	Element in a generic dataset or generic variable
x_n	-	Input in Artificial Neural Network
y_k	-	Network output
α	-	α-ferrite (α-iron)
γ	-	γ-ferrite (γ-iron)
δ	-	δ-ferrite (δ-iron)
η	-	Thermal efficiency

η_f	-	Fusion efficiency
σ	-	Surface free energy
σ_{ei}	-	Embryo-impurity surface tension
σ_{eL}	-	Embryo-liquid surface tension
σ_{iL}	-	Impurity-liquid surface tension
φ	-	Activation function in Artificial Neural Network
Φ	-	Cooling speed
Θ_j	-	Threshold in Artificial Neural Network

ABSTRACT

This study aims to evaluate the use of sensor fusion, based on neural networks, to estimate the extension of the fusion zone and of the sub-regions of heat affected zone in GMAW processes. Three samples were produced by depositing weld beads composed by AWS ER70S-6 wire on SAE 1020 steel plates varying the welding voltage, travel speed, and wire-feeding speed. Furthermore, the deposition parameters were varied during the deposition in each of the samples. The infrared radiation profiles emitted from the samples were gathered using the thermographic camera. The final microstructure was characterized by Optical Microscopy, Scanning Electron Microscopy and X-ray Diffraction. Finally, estimation models of the microstructure of weld beads are developed. The results obtained showed a gradual reduction in the fractions of the predominant phases of the fusion zone until the existence of only primary and perlite ferrite as the distance from the melting line increases. With the data obtained by thermography, microscopy and the welding parameters acquired by the interface, 6 network models (A to F) were proposed testing different configurations. The Model F with 17 and 15 neurons in the 1st and 2nd hidden layers trained with Bayesian Regularization and 4 training cycles showed good results in comparison with the other models (average error of 12.9%) and was satisfactory in terms of practicality in estimate of the microstructure of the welded region.

Keywords: sensor fusion, GMAW, microstructure prediction, artificial neural networks.

RESUMO

Este estudo tem como objetivo avaliar o uso da fusão de sensores, baseada em redes neurais, para estimar a extensão da zona de fusão e das sub-regiões da zona afetada pelo calor em processos GMAW. Três amostras foram produzidas depositando cordões de solda compostos por AWS ER70S-6 em placas de aço SAE 1020 variando a tensão de soldagem, velocidade de deslocamento e velocidade de alimentação do fio. Além disso, os parâmetros de deposição foram variados durante a deposição de cada uma das amostras. Os perfis de radiação infravermelha emitidos pelas amostras foram coletados por meio de câmera termográfica. A microestrutura final foi caracterizada por Microscopia Ótica, Microscopia Eletrônica de Varredura e Difração de Raios-X. Por fim, foram desenvolvidos modelos de estimativa da microestrutura de cordões de solda. Os resultados obtidos mostraram uma redução gradativa nas frações das fases predominantes da zona de fusão até a existência apenas de ferrita primária e perlita com o distanciamento da linha de fusão. Com os dados obtidos por termografia, microscopia e os parâmetros de soldagem adquiridos pela interface, 6 modelos de rede (A a F) foram propostos testando diferentes configurações. O Modelo F com 17 e 15 neurônios na 1ª e 2ª camadas ocultas treinados com Regularização Bayesiana e 4 ciclos de treinamento apresentou bons resultados em comparação aos demais modelos (erro médio de 12,9%) e foi satisfatório em termos de praticidade na estimativa da microestrutura da região soldada.

Keywords: fusão de sensores, GMAW, previsão microestrutural, redes neurais artificiais.

1. INTRODUCTION

Welding processes play a fundamental role in joining materials, repairing components and to building coatings on worn parts in several areas. Among the most used processes for joining metal devices or parts, the Gas Metal Arc-Welding (GMAW) process can be used in several applications - i.e. automotive, naval, aerospace industries and in the manufacture of devices and tools for industrial, domestic, medical and scientific applications - observing the limitations of dimensional precision (CRUZ, 2014). It represents a competitive alternative against manual welding processes to joining pipelines (BESTARD; ALFARO, 2015) which motivates the various studies that aim to improve the control of the numerous process variables [(BESTARD; ALFARO, 2016), (BESTARD; SAMPAIO; ALFARO, 2018), (PAULA; MODENESI; TRINDADE, 2018), (DE MIRANDA; SCOTTI; FERRARESI, 2007)]. The work conducted by Bestard and Alfaro (2016) presents a methodology for modeling, optimization and control of reinforcement height and width weld bead, allowing you to adjust the process parameters in real-time. For this purpose a fuzzy logic controller was used. Bestard, Sampaio and Alfaro (2018) developed a droplet detachment sensor aiming to implement a metal transfer control system. The final control system was capable of modifying parameters that provided stable transfer at one drop per pulse rate, from welds starting at inadequate pulse parameter conditions. A welding current prediction was carried out by Paula, Modenesi and Trindade (2018). The authors developed mathematical models which showed that welding current increased linearly with increasing wire feed speed and open-circuit voltage, whereas it decreased with increasing electrode stick out and preheat current. This way, mathematical models have been enhanced by a numerical optimization process leading to higher deposition rates under the same input conditions. De Miranda, Scotti and Ferraresi (2007) developed a numerical model with finite droplet height included. Furthermore, the energetic balance was analytically solved by the energy equation of the wire, including as boundary condition contact resistance between contact tip and wire. Quality and functionality of weld beads produced can be associated with the weld bead geometry (SHAHIAND; PANDEY, 2006). However, the evaluation and control of microstructure of weld beads in real time applied in arc-welding are a very complex challenge (TERASAKI; SIMPSON, 2005)(TERASAKI; SIMPSON, 2005)(TERASAKI; SIMPSON, 2005)(TERASAKI; SIMPSON, 2005). A possibility for performing these analyzes in real time is the use of noninvasive measurements such as thermography, ultrasound and spectrometry.

Nevertheless, it is still extremely difficult with current technology to measure and control the depth of weld beads (OLABI; ALASWAD; BENYOUNIS, 2014). Sensor fusion is based on obtaining data that cannot be acquired by direct measurements by the use of various indirect measurements given by different sensors (OLABI; ALASWAD; BENYOUNIS, 2014). Taking that into account, sensor fusion techniques can be applied in the estimation of physical quantities such as weld bead depth (OLABI; ALASWAD; BENYOUNIS, 2014) and extension of the Fusion Zone (FZ) and Heat Affected Zone (HAZ). Sensor fusion is also based on areas such as statistics and artificial intelligence (OLABI; ALASWAD; BENYOUNIS, 2014). That requires the use of tools that helps in decision-making, such as artificial intelligence techniques. A technique that can be implemented in this context is that of artificial neural network (ANN). They are based on the central nervous function of animals and are capable of machine learning as well as pattern recognition, which is very useful in proposing complex models. Just as humans learn more and more as they gain experience over their lives, neural networks need data to learn to recognize patterns through training. This tool can be used in robotic welding as a machine learning method, enabling the system to self-adjust and control metal deposition in real-time. This study aims at assessing the efficiency of sensor fusion, based on neural networks, to estimating the microstructural properties of the weld bead and modifications in the base material in GMAW processes. Weld beads of an AWS ER70S-6 wire will be deposited varying the welding voltage travel speed, and wire-feed speed. The characteristics of the thermal behavior of the material will be analyzed using the thermographic information from an infrared camera. The topography of the thermally affected zone will be analyzed by image processing techniques. The final microstructure will be characterized by Optical Microscopy, Scanning Electron Microscopy and X-ray Diffraction. Finally, estimation models of the microstructure of weld beads are presented using all the information gathered by the sensors and ANN algorithms.

2. OBJECTIVES

2.1. GENERAL OBJECTIVE

The objective of this work is to characterize the microstructure of weld beads and evaluate the efficiency of sensor fusion, based on neural networks, to estimate the microstructural characteristics of both the bead and the base material in GMAW processes.

2.2. SPECIFIC OBJECTIVES

To achieve the main objective the following specific objectives were proposed:

a) To evaluate the influence of the welding voltage, the wire feed speed and the welding speed on the microstructural characteristics of the weld bead.

b) To characterize the microstructure through metallographic tests, Optical Microscopy (OM), Scanning Electron Microscopy (SEM) and the chemical and phase composition by X-Ray Diffraction (XRD).

c) Develop new models (through neural networks) in order to estimate the microstructure of the weld bead.

3. LITERATURE REVIEW

3.1. MEASUREMENTS AND CONTROL OF GMAW PROCESS

GMAW is a welding process that uses an electric-arc between a continuous filler metal electrode and the weld pool above base metal. The process uses gas shielding protection. The basic concept of gas metal arc welding was developed in the 1920s. However, the process did not become commercially available until 1948. Initially, this process used a high-current-density, small-diameter, bare-metal-electrode and an inert gas for arc shielding (BRIEN, 1983).

3.1.1. Fundamentals of GMAW process

The GMAW (Gas Metal Arc Welding) welding process is characterized by the opening of an arc between the base metal and a consumable electrode under protected atmosphere. Basic GMAW welding equipment consists of a torch, an electrode wire, a wire feeder, a welding power source, cables and shielding gas (see Figure 3.1 and Figure 3.2). The electric-arc is established by inserting a determined value of electric tension between the wire and the workpiece and is responsible for ionizing environment gases and promoting the opening of a plasma column. The energy source of the arc welding process is the heat generated due to the formation of a plasma column between electrode wire and workpiece. This heat melts the electrode wire which is transferred in the liquid state to the workpiece. The displacement of the torch over the weld joint and the deposition of the filler material, form the weld bead. This method includes the use of protective gas (or gas mixture) that is responsible for protecting the weld pool against inclusions or aggressive atmosphere. (BRIEN, 1983).

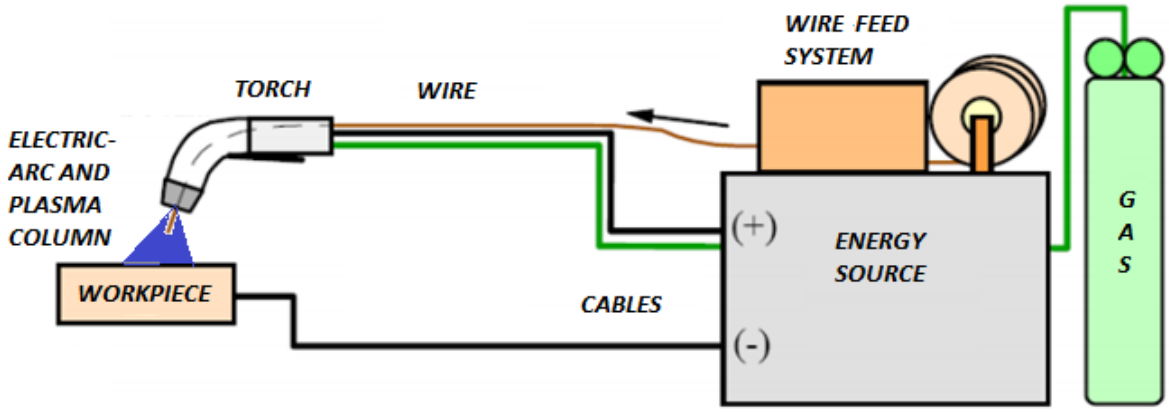

Figure 3.1 - GMAW basic components. Adapted from Bracarense, Marques and Modenesi (2011).

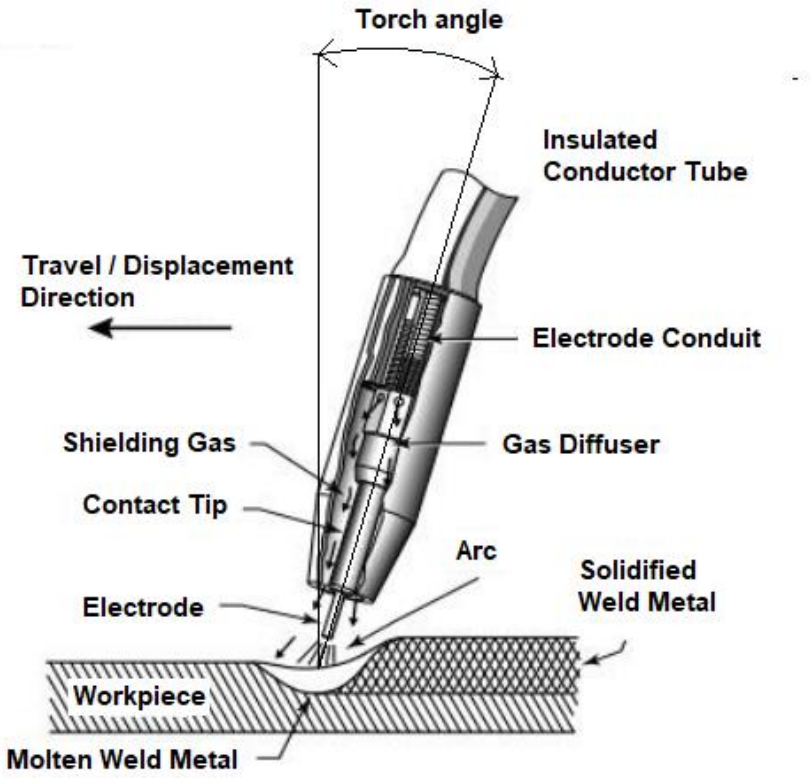

Figure 3.2 - GMAW torch scheme. Adapted from Bestard (2017).

GMAW process has great potential for use in automatic mode, being possible to execute operations in dedicated systems (fixed configurations) or robotic/programmable, which the programming provides great flexibility (BRACARENSE; MARQUES; MODENESI, 2011).

Some characteristics of this welding process are high deposition rate, high yield, formation of little or no slag, good penetration, ease of operation and field of possibilities to be explored. The polarity most used in GMAW welding processes is the reverse (positive electrode

wire) due to the better stability of the electric-arc. Direct polarity is more used in coating operations because it provides a higher deposition rate. Alternating current can be used, but the arc stability is not good (TEIXEIRA, 2011).

The transfer of metal in the GMAW process can be carried out, classically, in three main ways: short-circuit, globular and spray transfer (MODENESI; BRACARENSE, 2004). Figure 3.3 schematically presents the operational envelopes of these three metal transfer forms considering the current and welding voltage parameters for the GMAW process with positive electrode and an argon-based shielding gas.

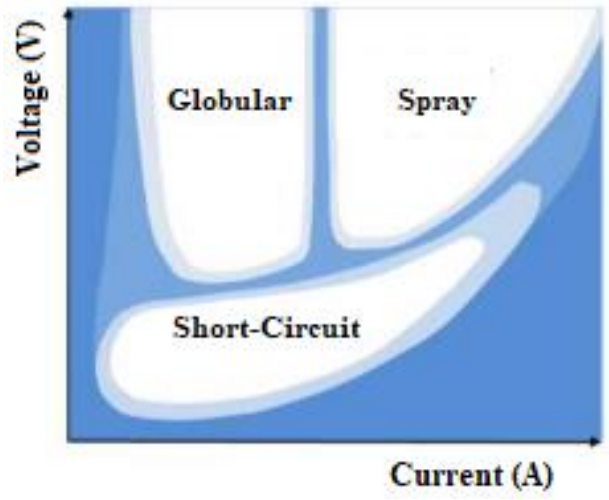

Figure 3.3 – Schematic representation for current and voltage conditions for the different transfer modes for GMAW welding with an argon-based shielding gas. Adapted from (MODENESI; BRACARENSE, 2004).

Gas metal arc welding with short-circuit transfer (GMAW-S) is one of the most used manufacturing processes by industries in the structural applications. It has a large number of advantages as high metallic transfer, high penetration, ease of operation in various positions and flexibility for automation (MENESES; SILVA; ALFARO, 2019). GMAW-S process encompasses the lowest range of welding currents and electrode diameters associated with gas metal arc welding. Metal transfer occurs when the molten metal from a consumable electrode is deposited during repeated short-circuits (MENESES; SILVA; ALFARO, 2019). This mode of transfer produces a small weld pool with fast solidification, that is generally suited for the joining of thin sections, for out-of-position welding, and for bridging large root openings (BRIEN, 1983).

Globular transfer occurs when the arc currents and voltages are between the voltage and current levels of the short circuit transfer and the spray transfer. The globular transfer is characterized by the transfer of molten metal in the form of large irregular drops of

approximately up to four times the diameter of the electrode, which drop into the weld bath by gravity (CRUZ, 2014).

In the spray transfer, the molten metal is propelled axially towards the workpiece through the arc in the form of a stream of small drops of an equal or smaller size than the diameter of the electrode.

3.1.2. Welding parameters and geometry

According to Karadeniz, Ozsarac and Yildiz (2007), welding parameters have a considerable influence on the quality of the produced beads (as is the case with geometry, penetration, mechanical and microstructural properties) and on the stability, productivity and costs of the deposition process. The welding parameters can be divided into primary and secondary. The group of primary parameters comprises current intensity, voltage and travel speed (CHAN; PACEY; BIBBY, 1999). The group of secondary parameters is formed by parameters such as contact tip – workpiece distance (CTWD), stick out (extension of the wire after the contact tip on the torch), wire feeding speed, shielding gas, wire diameter, base material (TEIXEIRA, 2011), torch angle, nozzle distance, free wire length, welding position and direction (IBRAHIM et al., 2012)

Initially, the permissible current range for material and diameter of electrode wire used must be known. Large diameters of electrode wires allow the use of higher current values, with greater penetration and fusion rate. Therefore, the choice of electrode wire diameter is associated with base metal thickness, desired penetration, deposition rate, welding position and weld bead geometry (TEIXEIRA, 2011).

The shielding gas influences the metal transfer mode, the arc stability, the welded joint mechanical-metallurgical properties, the welded joint geometry and appearance, the determination of the maximum travel speed, the cost of operation and the prevention of the appearance of defects such as undercuts and inclusions. The shielding gas flow must be laminar and have an adequate value. Low flow of shielding gas causes contamination of the fusion pool by atmospheric air. On the other hand, a turbulent flow resulting from a high gas flow combined with a low travel speed can cause air suction into the electric-arc (TEIXEIRA, 2011). Furthermore, the shielding gas also acts to prevent the formation of nitrides and oxides in the weld region. The choice of the appropriate shielding gas must take into account the materials to be welded (BESTARD, 2017).

The choice of the electrode to be used must take into account the material applied, the design of the joint to be welded, the surface conditions, the mechanical strength range and conditions of use (BESTARD, 2017).

According to Machado (1996), an excessive angle of displacement of welding torch can also induce penetration of air under the arc, it is not recommended that it exceeds around 25°. Argon is the most frequently used inert shielding gas, while carbon dioxide is the most widely used active shielding gas. Mixtures of inert and active gases are used to achieve a specific weld bead geometry (TEIXEIRA, 2011).

The next step is to adjust current, voltage and travel speed. The welding current has a direct influence on the deposition rate, in the metal transfer mode and in penetration. In addition, it influences the height of the weld bead reinforcement as a consequence of the almost linear relationship of the welding current with the wire melting rate. In constant-current welding sources, the current control has no relation to the wire feed speed (TEIXEIRA, 2011). In constant voltage type energy sources, current control occurs through the electrode wire feed speed. The welding voltage establishes an important relationship with the bead width and the transfer mode. In constant-voltage welding sources, the welding voltage is selected according to parameters such as welding current, desired geometry, wire material, gas composition, and in order to stabilize the arc (TEIXEIRA, 2011). The travel speed influences both deposition rate and bead geometry. The higher the travel speed, the greater the productivity of the process. However, the quality of the weld beads produced must be observed in order to avoid defects such as cracks by solidification. Furthermore, by increasing travel speed and setting the other parameters, is observed less deformation in welded structure, reduction of HAZ and refined grains in weld metal (TEIXEIRA, 2011).

The exact effect caused by changes in the stick out and torch angle is not generally known for anticipation. What can be predicted are the trends that such changes promote in the process and in the primary adjustable variables (MACHADO, 1996). When the stick out is increased, there is an increase in the electrode temperature by Joule effect due the increase of the electric resistance on welding circuit. Thus, by increasing the stick out, a reduction in penetration and an increase in the deposition rate are observed. The torch angle influences the weld bead penetration. A pushing travel angle, pushing the weld pool, will reduce the penetration, with the weld bead becoming wider and flatter. A dragging travel angle up to 65° provide an increase in penetration. If the dragging travel angle is lower than about 65° the penetration tends to decrease (TEIXEIRA, 2011).

3.1.3. Measurements in GMAW process

In order to produce weld beads that present geometry, strength and quality within a certain specification, it is necessary that the system is able to monitor or to estimate some variables in order to allow interventions to be made allowing for the control of the process. In addition, proper process control provides increased productivity and reduced costs while maintaining quality and design specifications on the welded joint.

The welding variables of the GMAW process can still be divided as to the intervention possibilities to change their values according to the measurement methods available with current technology (BESTARD, 2017). These possibilities can be:

- Fixed variable: cannot be modified by the operator and it is defined in process design.
- Online adjustable variable: can be modified during the process.
- Offline adjustable variable: can be modified only before starting the process.
- Online quantifiable variable: that is measurable during the process.
- Offline quantifiable variable: that is measurable only after the process ended

A list with some of these variables can be observed in Table 3.1

Table 3.1 - Main variables of automatic GMAW process to constant voltage. Adapted from Bestard (2017).

Fixed	Adjustable online	Adjustable offline (old welding power sources)	Quantifiable online	Quantifiable offline
Shielding gas composition	Welding Voltage	Inductance of the welding power source	Welding Voltage	Weld bead depth (penetration)
Position of the piece or pipe.	Inductance of the welding power source.	Shielding gas flow rate	Welding Current	Weld bead width
Wire Electrode characteristics	Wire-feeding speed		Weld bead width	Reinforcement (weld buildup)
Thickness of the base metal.	Travel speed		Reinforcement (weld buildup)	Weld bead microstructure
Physic properties of the base metal	Orbital angle (orbital welding)			
Polarity of the weld electric current	Torch angle and			
	Work angle to base metal surface			
	CTWD			
	Stickout			
	Nozzle to plate distance			
	Shielding gas flow rate			

a) Measurement and control of arc welding parameters

To measure arc welding parameters and to automate the welding process becomes more and more necessary in search of higher quality and productivity which motivates several studies. The quality required for a weld bead includes geometric and microstructural aspects that must be controlled by the parameters of the GMAW process (GANJIGATTI; PRATIHAR; ROY CHOUDHURY, 2008; KIM et al., 2003a).

The information of some parameters - i.e. welding current and welding voltage - can be obtained using analog/digital interfaces connected to the welding source. For measurements of other variables, more complex procedures may be necessary. In the case of measurements of weld bead geometry, for example, there are problems to be solved, such as powerful radiation emissions by electric-arc, in a long-range of the frequency spectrum, including high temperature and visible light. The main process control variables related to the characteristics of the electric-arc are welding current, welding voltage and, in some processes, wire feed speed, travel speed (torch displacement speed), gas flow and lead times, pre and post gas, source impedance and control of opening and closing arcs (BESTARD, 2017).

In many processes, it is necessary to know or control the CTWD (see Figure 3.4). Strategies for measuring this distance can be the positioning control of the robot that performs the workpiece-torch movement or a laser-based distance sensor.

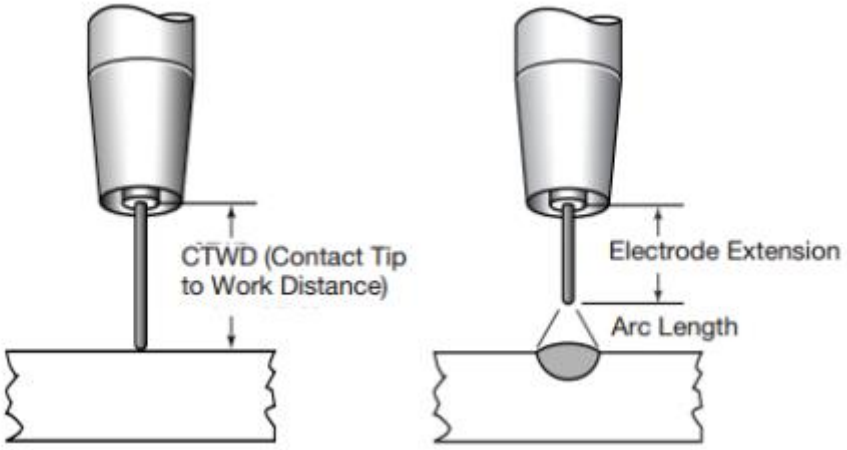

Figure 3.4 - Contact tip to work distance and electrical stick out (or electrode extension) differences (BESTARD, 2017).

Performing measurement and control through the positioning system of the robot control system is less costly and less accurate. In this method, variations in the material's surface and thickness can affect the accuracy of the CTWD measurement. This error is critical for the GMAW process, as small variations in CTWD can greatly alter the value of the welding circuit impedance and, consequently, the welding current and thermal input (BESTARD, 2017).

A fundamental group of parameters to determine the quality and functionality of weld beads are the geometric parameters known as reinforcement height, penetration and bead width – as shown in *Figure 3.5* and *Figure 3.6* (BESTARD, 2017).

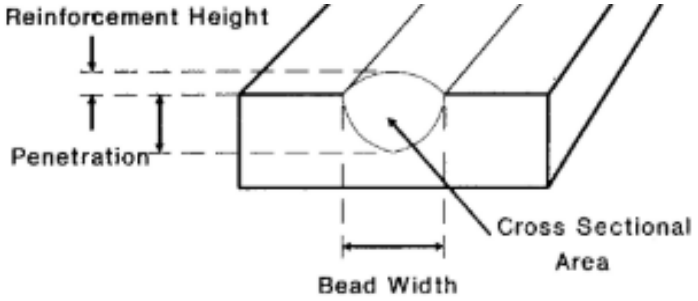

Figure 3.5 - Geometric parameters of a single weld bead without joint preparation. Adapted from Karsai et al. (1992).

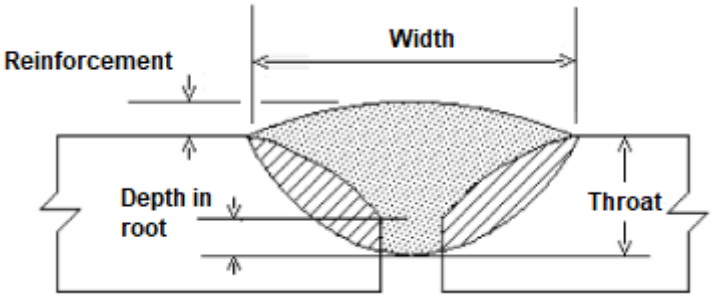

Figure 3.6 - Geometric parameters of a single weld bead with V-groove.

These geometric parameters influence characteristics such as functionality and mechanical properties of the welded joint. In manual welding processes, the visual information provided by the welding pool is used by the operator as process control parameters.

Furthermore, the thermal field imposed on the welding joint allows the formation of different microstructures in FZ and HAZ (see Figure 3.7). There are different microstructures at FZ and HAZ. The latter also has four subdivisions (which will be discussed in section 3.2.6) that have different mechanical behavior. The mapping of the size of these zones in real-time would be an extremely useful tool for the control of welding processes, making it possible to obtain adequate mechanical strength.

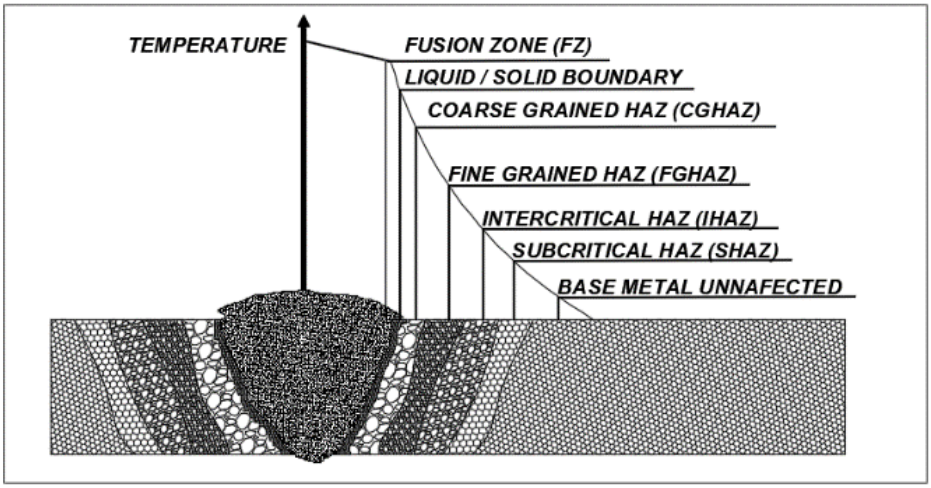

Figure 3.7 - Scheme of temperature influence in regions of weld joint.

However, it is currently extremely difficult to carry out real-time measurements of the extent (or area) of these different regions present in the microstructure due to technical limitations imposed on the collection of this information, especially in field welding.

b) Studies in measurements and modeling of geometry, microstructure and properties of weld beads

As well as determining the extent of microstructural zones, predicting the penetration of weld beads is also a complex task. The estimation of these microstructures has been motivating several academic studies aiming at the improvement of measurement and modeling techniques.

Kim, Basu and Siores (1996) studied the influence of the GMAW process parameters (wire diameter, gas flow, travel speed, current and tension) on the weld bead penetration. The authors observed an increase in the penetration of the weld bead with an increase in the wire diameter, arc current and welding voltage and a reduction in travel speed. The gas flow rate did not significantly affect the weld bead penetration. Murugan and Parmar (1994) used the Response Surface Methodology to define quadratic relationships between the stainless-steel bead geometry and the GMAW process parameters. The authors showed that the models developed can be used in automated or robotic surfacing in the form of a program for obtaining overlays of the desired high quality. Lee and Rhee (2000) used the multiple linear regression technique to establish the relationship between responses to the GMAW process parameters. Iordachescu et al. (2006) carried out a study of the influence of shielding gases and process parameters on material transfer. They also studied the shape of weld beads in joints welded with

inert gas. They concluded that shielding gases significantly affect convexity, color, brightness, smoothness and the formation of porosity in the weld beads. Palani and Murugan (2006) developed a mathematical model to predict the weld bead geometry in the stainless steel FCAW process. The results presented showed that the models developed can predict the bead geometries and dilution with reasonable accuracy. Balasubramanian, Jayabalan and Balasubramanian (2008) developed a mathematical model to predict the geometry of a weld bead and the hardness by welding titanium alloys. Ganjigatti, Pratihar and Roy Choudhury (2007) used cluster-wise regression to predict the geometry of the GMAW weld bead and obtained improved performance in relation to the global regression.

Kim et al. (2003b) analyzed the sensitivity of the GMAW process in order to assess the influence of measurement errors on the uncertainties of the estimated parameters through non-linear multiple regression to model the process. Kim et al. (2004) developed mathematical models based on linear and non-linear regressions to relate the geometry of the bead with the welding parameters based on two ANN training methods: error backpropagation algorithm and the Levenberg-Marquardt approximation algorithm. The authors demonstrate that the Levenberg-Marquardt approximation algorithm was more efficient, as it reduces the root of the mean sum of the square error (RMS). Elroğlu, Aksoy and Orhan (1999) studied the effect of weld bead size on microstructure, mechanical properties and HAZ morphology in low carbon steels. From toughness tests it was found that the maximum hardness and the HAZ decrease with increasing heat supplied. Kolhe and Datta (2008) studied microstructure, mechanical properties and extension of the HAZ in a multipass SMAW process in a carbon steel plate 16 mm thick. To study the quality of welded joints in multiple steps, Xiong et al. (2013) developed a model for weld bead geometry based on circular arc, parabola and cosine functions. The authors also proposed conditions for the occurrence of overlapping between the weld beads. Jorge et al. (2019) performed the microstructural characterization by OM, SEM and Electron Backscattered Diffraction (EBSD) and occurrence of carbides in high-strength steels in GMAW and SMAW processes with post-weld heat treatment (PWHT) at 600°C and as welded.

Pavlyk and Dilthey (2004) studied the solidification conditions during Gas Tungsten Arc Welding (temperature gradient, local solidification rate, weld pool shape). The authors developed a numerical macroscopic finite element modelling calculation of the weld pool fluid flow and of the temperature distribution furthermore the simulations with spatial resolution of the microstructure. However, they pointed that the application of direct microstructure

modelling to real welding conditions requires a coupling between macroscopic heat and fluid flow modelling in the weld pool and micro-modelling techniques.

Yang and Debroy (1999) studied fluid flow and heat transfer during gas-metal-arc welding using HSLA-100 steel through a transient, three-dimensional, turbulent heat transfer and fluid flow mathematical model. The results presented by the authors demonstrate significant promise for understanding both macro-and microstructures of steel welds with relative low error.

Dhas and Kumanan (2013) proposed the modeling and prediction of dimensions of Heat-Affected Zone for SAW process using Finite Element Analysis (FEA) and Artificial Neural Network (ANN). The modeling was relatively accurate, although it does not distinguish between the sub-regions of HAZ.

Gunaraj and Murugan (2002) developed mathematical models for study the effects of welding parameters and heat input on the HAZ of submerged arc welds in structural steel pipes. The modeling was very efficient with an accuracy of 97% in some cases.

Zhang et al. (2018) developed a three-dimensional (3D) finite element model to simulate the welding temperature field of a Ti-6Al-4V alloy using different welding currents based on a Gaussian heat source model. They calculated the microstructure evolution of the weld pool through the macro-micro coupling cellular automaton-finite different (CA-FD) method and obtained good results comparing with experiments carried out by GTA welding.

Gutiérrez et al. (2016) developed a comparison between theoretical and experimental thermal fields as well as a microstructural behavior and residual stresses applying multiple weld beads in the joint of two API 5L X52 pipe sections. The results showed that the simulation method can be used efficiently to determinate with accuracy the optimum welding parameters of this kind of weld applications.

The above works are some examples of studies carried out on the modeling of important characteristics of weld beads. However, it is noteworthy that studies on predicting characteristics such as penetration of weld beads and microstructure of welded joints are still very incipient. In the case of HAZ modeling, most of these studies use a purely mathematical approach. This reinforces the importance of the work presented here due to the use of process data to model the behavior of the microstructure of welded joints.

3.1.4. Sensor fusion in welding processes

The evolution of automated welding processes makes it possible to increase the productivity and quality of the joints (MODENESI; MARQUES; SANTOS, 2012). The development of instrumentation with estimation algorithms using sensory fusion techniques in real time is already a reality in the industry (BESTARD; ALFARO, 2015).

However, the development of these techniques is in full swing and in the hands of large companies with captive know-how and its application in the welding processes is still incipient (BESTARD et al., 2018).

Sensor fusion algorithms and indirect sensing techniques allow estimating measurements of variables that are impossible or very difficult to measure directly. In order to obtain optimized results in estimations by sensor fusion, it is necessary to combine several measurement technologies taking full advantage of each one (BESTARD, 2020).

Sensor fusion techniques have many applications as aerial and ground navigation of mobile robots, environmental monitoring systems, visual sensor networks, medicine, security, fault detection, and quality control, among others (BESTARD; ALFARO, 2015). A very promising application for sensor fusion is weld bead geometry and microstructural behavior estimation. Despite it is a relatively new research area, it is the third method used for the indirect monitoring of the welding process, as shown in Figure 3.8.

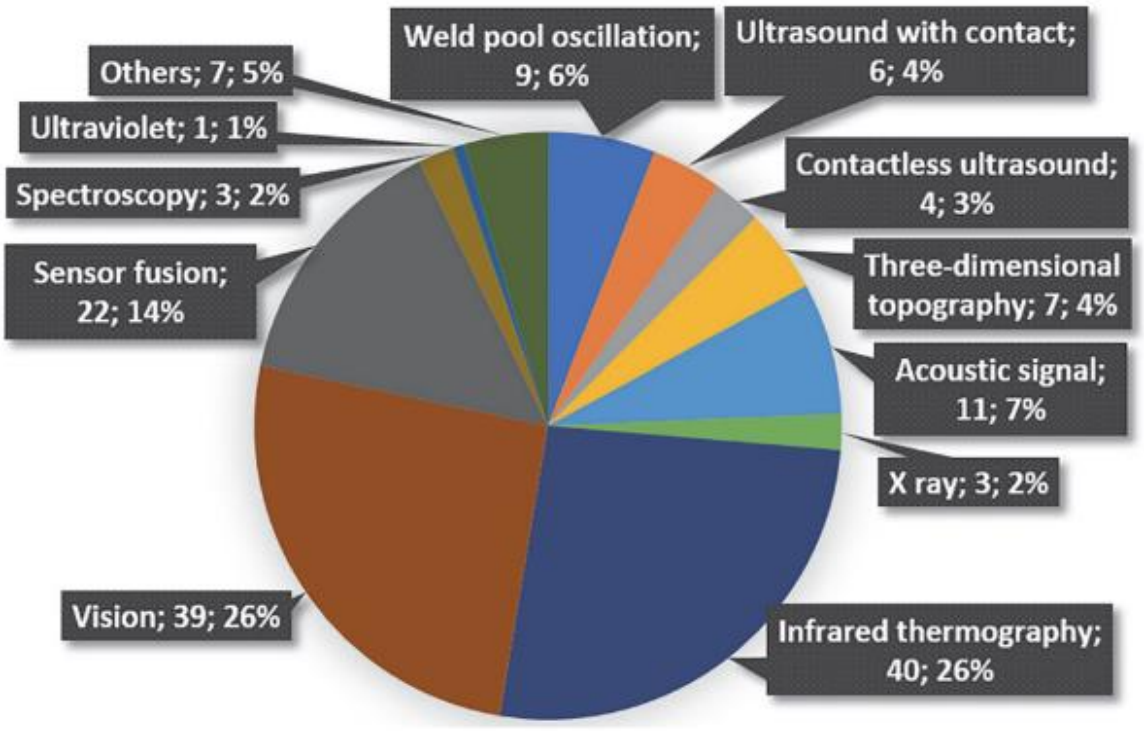

Figure 3.8 - Literature review statistics about indirect monitoring technologies used to obtain measurements of the weld bead geometry (BESTARD; ALFARO, 2018).

There are different sensor fusion classifications as reported by Sotela (2010). One of the most representative classifications for welding processes is according to the relationships of the input data, which defines how the information relates between the sensors. These relationships can be in three modes: complementary, competitive or redundant, and cooperative (see *Figure 3.9*).

In complementary fusion occurs the fusion of incomplete information that is obtained starting from different sources. For example, combining the weld pool thermographic information (A) gathered by an infra-red camera (S1) and the weld bead dimensions (B) obtained from a video camera (S2) is possible to calculate the weld pool dimensions (a+b). This mode occurs in fusion of information of several sensors which measures different parts of an atmosphere or phenomenon, covering a larger area and allowing a more complete and more global vision of the process.

In competitive or redundant fusion all the sensors are monitoring the same area, working redundantly and competitively. These sensors may have the same or different measurement principles. An example is the dimensional information (B) about the weld bead obtained from two CCD cameras (S2 and S3) used to calculate the weld bead dimensions (b).

Finally, in cooperative or coordinated fusion the information from independent several sensors to obtain new information, for example, the combination of the information of the weld bead (C) obtained from a vision system (S4) and pyrometer (S5) to estimate the weld bead penetration value (c).

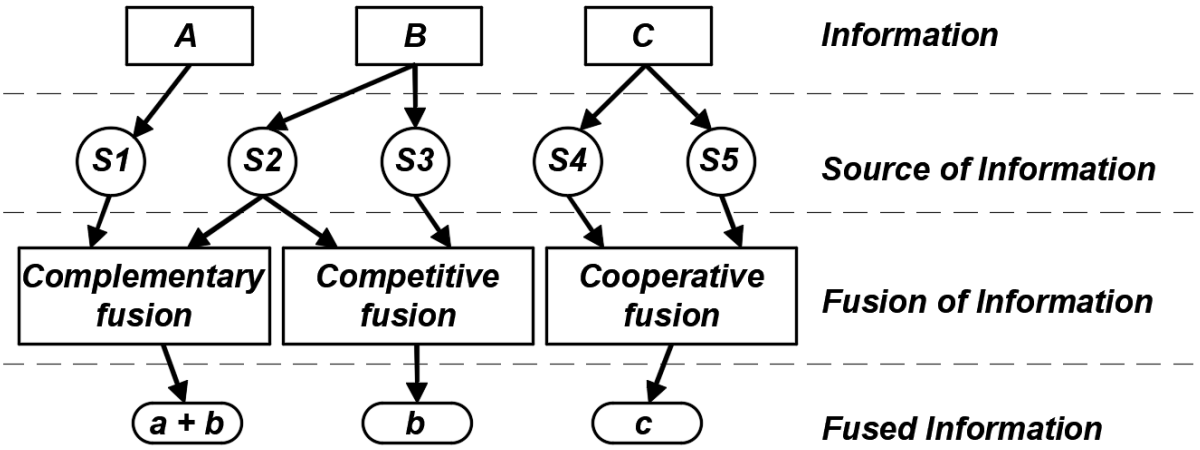

Figure 3.9 - Schematic representation of input relationships and of levels of information fusion process. Adapted from (BESTARD, 2020)

Figure 3.9 shows four levels of the fusion process. The following list exemplifies welding process parameters:

• Information level represents the input magnitudes and zones that are measured by sensors, for example, the weld bead and weld pool thermographic data along the welding process and the microstructural information gathered in microscopy analysis.

• Source of information is the sensors installed on the process, for example, the thermographic camera and the microscopes used.

• The fusion of information is the algorithms used to obtain the fused information, for example, neural network algorithms.

• Fused information is the final result, for example, the weld bead microstructure profile in several regions of their cross-section.

Artificial intelligence is a versatile tool that can be defined as an association between mathematics and computer science that aims to design artificial intelligent systems. This way, these systems can interpret stimuli from the environment and make decisions autonomously and continue to adapt to the new conditions (CRUZ, 2014). Among the artificial intelligence techniques, we can highlight fuzzy logic and artificial neural networks (ANN).

Fuzzy (or diffuse) logic is a model that aims to determine inaccurate quantities, however, in a systematic way. Instead of using a complex mathematical model, industrial controllers based on fuzzy logic can be related to the experimental knowledge of trained human operators. This way, fuzzy logic controllers can make control actions as good as human's actions and always consistent (CRUZ, 2014).

Artificial neural networks (ANN) use a working principle similar to biological neurons to resolve conflicts based on learning processes. Figure 3.10 shows a scheme of an artificial neuron.

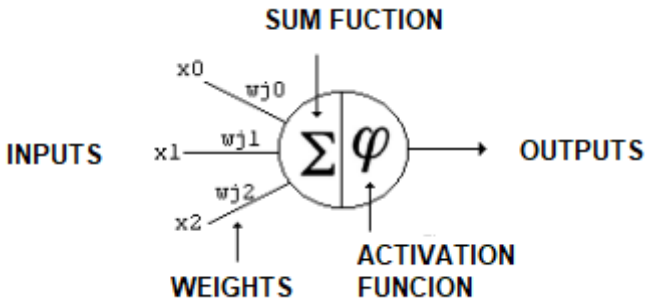

Figure 3.10 - Artificial neuron scheme. Adapted from Cruz (2014).

3.1.5. Artificial Neural Networks

Artificial neural networks uses the continuous interaction with the external environment improves the solution of a given problem, making this technique interesting to solve issues

where there is no analytical model or problems where the analytical model is very complex, such as controlling welding parameters (CRUZ, 2014). Synapses have an associated weight which is adapted as the environment sends new stimuli in order to establish relationships between such stimuli and the desired outputs. This is called training (learning) process. In this way, the algorithm operates with the least human intervention and makes its own decisions according to its learning and experiences. Therefore, the knowledge of the network is stored in the weight of the connections and learning corresponds to the adjustment of the weights so that the network behaves properly (CRUZ, 2014).

The determining factors for the functioning of the network are dataset for training and verification, network topology, activation function and learning strategy. Choosing the dataset should be careful to avoid problems like ambiguity or discrepancies in addition to taking into account the most representative data for solid and comprehensive results (CRUZ, 2014).

An important parameter of ANN is the number of neuron layers. Single-layer networks have only one layer of neurons between inputs and outputs. Multilayer networks have layers of intermediate (or hidden) neurons between inputs and outputs (CRUZ, 2014). Network topology involves the way in which artificial neurons are organized. These provisions are similar to the standards adopted by the human brain.

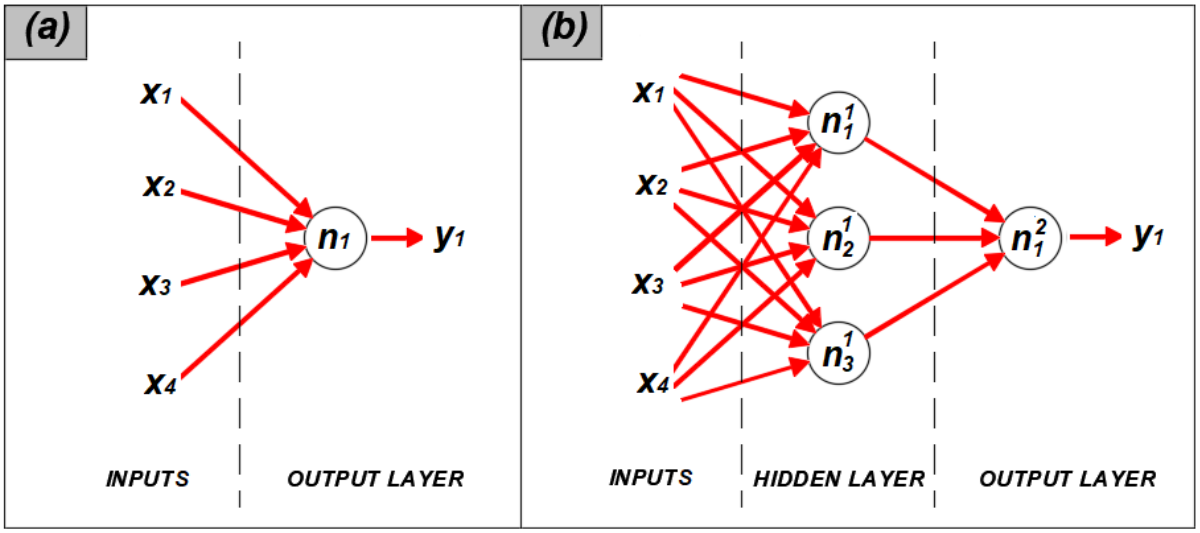

Figure 3.11 - Scheme of (a) single layer network and (b) multilayer network (Author).

There are two fundamental models of ANN topology: direct networks (feedforward) and recurrent networks (feedback). In direct networks (represented in Figure 3.11), there are no communication cycles between neuron layers, as in perceptron, *Figure 3.12*, multilayer perceptron and ADALINE (Adaptive Linear Element) networks, *Figure 3.13*. An important difference between the Perceptron and ADALINE networks is that the first uses a binary

response value (as a result of classification, for example) to calculate an error used to update the weights. The ADALINE network uses a continuous response value to update the weights (therefore, before the binary output is produced) (AI; ZHOU; XU, 2007).

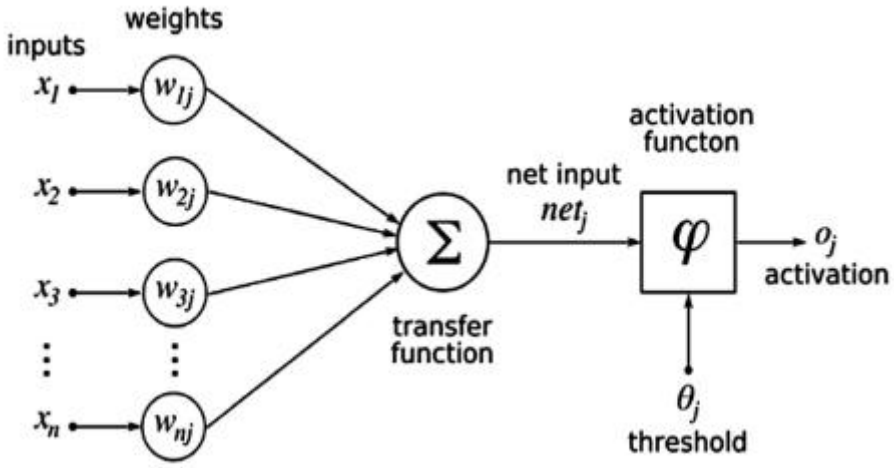

Figure 3.12 - A tipical multilayer perceptron.(AHMED, 2017)

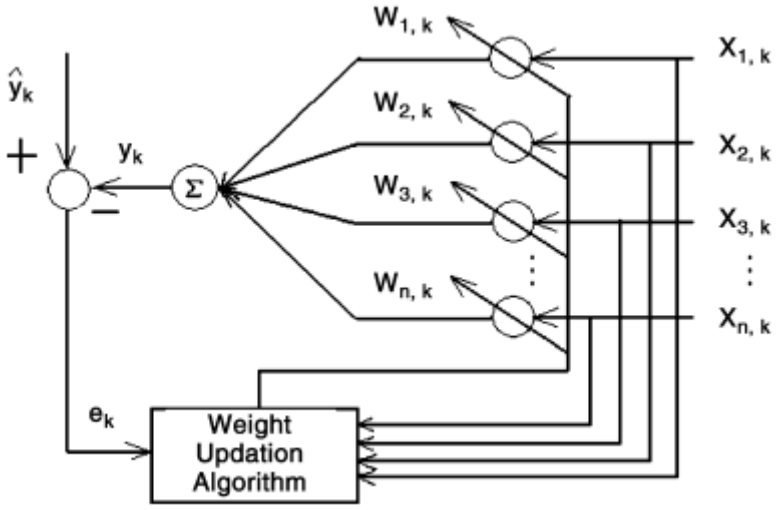

Figure 3.13 - Architecture of ADALINE network (AI; ZHOU; XU, 2007).

In feedback networks (see Figure 3.14), there is at least one cycle in communication between neurons. In addition, the connections between neurons are not restricted.

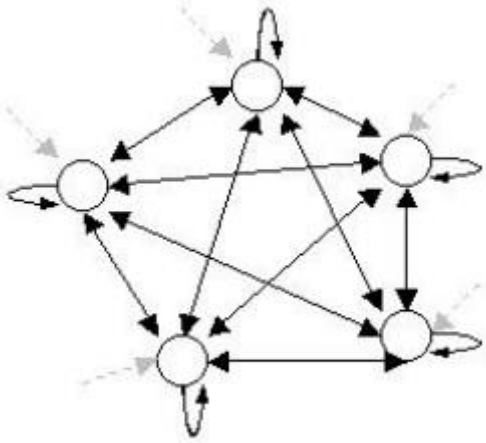

Figure 3.14 – Hopfield Networks are an example of feedback network (CRUZ, 2014).

The activation function defines what the next activation state of the unit will be based on the internal input and the current state. If the activation state to be established depends on dynamic properties, differential equations (continuous result) or finite difference methods (discrete results) are applied in their definition. In order to simplify processing, algebraic functions are generally used (SILVA, 1998).

In linear functions with a slope of 1, the output is equal to the input signal. In logistic functions, the range of variation of the derivative of the function is limited due to a saturation effect. However, this type of function presents activation values only in the interval (0, 1). As an option to the logistic function, there are two other functions with a similar shape, which are the hyperbolic tangent function and the tangent arc function, with intervals (-1, 1) and (-π/2, π/2), respectively, as shown in Figure 3.15 (CRUZ, 2014).

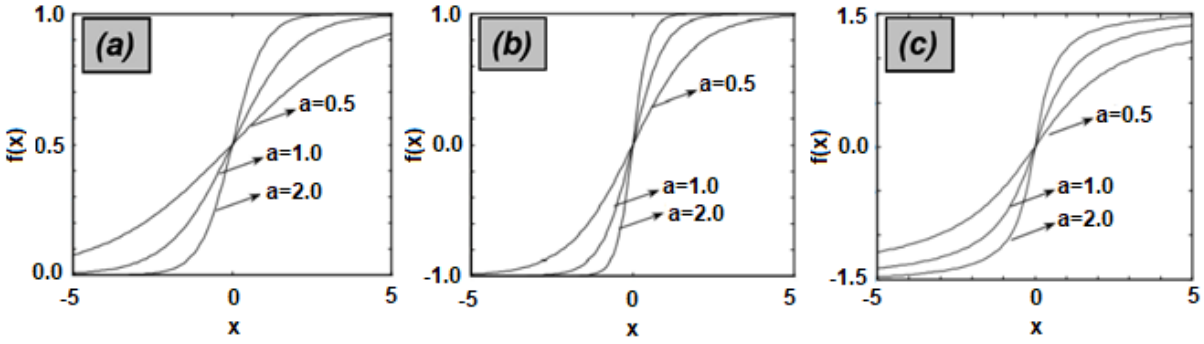

Figure 3.15 - Representations of the functions (a) logistics, (b) hyperbolic tangent and (c) tangent arc (CRUZ, 2014).

The main ANN classification is given by the algorithm or learning process applied in training (XAVIER, 2005). These algorithms or processes can be supervised or unsupervised. According to Medeiros (1999), supervised learning is characterized by the continuous provision of entry standards and their respective exits to ANN. In this way the adjustment of the weights

is done through comparisons between the supplied output and the desired value until a tolerable error is reached. The main networks of supervised learning are perceptron and ADALINE

Medeiros (1999) also mentions that in unsupervised learning, ANN receives the dataset, establishes some properties (such as regularity, patterns and correlations) of the sets, divides them into classes and learns to reflect these properties in the output. Thus, the properties learned by the network vary with the type of architecture and the form of learning adopted. Examples of these types of networks are Kohonen's Self-Organizing Map, Hopfield Networks and Bidirectional Associative Memory.

Several times the ANN designer does not have all the basic information to determine the topology, activation function and training algorithm to be used. Therefore, the training and analysis process can bring good approximations by adopting successive trial and error steps (CRUZ, 2014).

3.2. LOW CARBON AND LOW ALLOY STEELS USED IN WELDING

Steels can be classified by different systems and characteristics, such as: (TOTTEN, 2006):

- Compositions: carbon, low-alloy, and alloy steels;
- Manufacturing methods: oxygen converter, electric furnace, or electroslag remelting methods;
- Application or main characteristic: structural, tool, stainless steel, or heat resistant steels;
- Finishing methods: hot rolling, cold rolling, casting, or controlled rolling and controlled cooling
- Product shape: bar, plate, strip, tubing, or structural shape;
- Oxidation practice employed: rimmed, killed, semi-killed, and capped steels;
- Microstructure: ferritic, pearlitic, martensitic, and austenitic;
- Required strength level, as specified in the American Society for Testing and Materials (ASTM) standards;
- Heat treatment: annealing, quenching and tempering, air cooling (normalization), and thermomechanical processing;
- Quality descriptors and classifications, such as forging quality and commercial quality.

Among the above classification systems, the chemical composition is the most widely used basis. Fine-grained structural steels have mechanical properties in the "hot-rolled" condition without special care that characterizes processing as controlled rolling or thermomechanical processing (SOARES, 2015).

Structural steels are widely used in various sectors of the industry (pipelines, gas pipelines, pipelines, ships, oil platforms, storage tanks, among others). Within the refineries, these tanks store raw material for supplying the units, an intermediate product that is the final product of one unit and raw material of another, in addition to the final product that is ready for distribution. In all these segments we perceive an intense search for the improvement of the quality of the welded joints in the manufacture of these structures to avoid the risk of accidents such as a rupture since most of these tanks store products that are harmful to the environment and people's health who work there (LIMA JÚNIOR, 2013).

3.2.1. Classification of steel microstructures

While the development of regression and neural network models requires good quality database information, the development of sophisticated physical modeling for microstructure prediction in steels has led to a need for accurate calibration data. However, the microstructures observed in steel products are complex. A large number of reaction products may form at austenite grain boundary sites in thermomechanically processed or heat-treated steels (THEWLIS, 2004).

In the fusion zone of welds, the simultaneous and competitive formation of a variety of phases from both austenite grain boundary and intragranular sites may occur while, in the parent plate HAZ, steep thermal gradients may give rise to a wide range of transformation products. A scheme is thus required for classifying and quantifying complex steel microstructures (THEWLIS, 2004).

A scheme for identifying the various ferrite morphologies in isothermally transformed steels was first used in 1958 (TOTTEN, 2006). However, the effect of continuous cooling was to render the distinguishing morphological features much less distinct.

Classifying and quantifying the microstructures of steels has long been a contentious issue (THEWLIS, 2004). Depending on the plane of observation, constituents that are part of the same main structure may appear morphologically different giving rise to sub-category

components. Depending on the nucleation process, ferrite can be named with different terminologies like as:

- Allotriomorphic ferrite;
- Ferrite veins;
- Primary ferrite;
- Idiomorphic ferrite;
- Widmanstätten ferrite;
- Acicular ferrite;
- Ferrite with aligned second phase;
- Ferrite with non-aligned second phase.

The International Welding Institute (IIW) has developed a scheme (see Table 3.2) to assist the task of assigning nomenclatures to the main microstructures found in carbon steels used in welding processes (THEWLIS, 2004).

Table 3.2 - IIW microstructure classification system. Adapted from Thewlis (2004).

Principal structure classification	Category terminology			Component structure description
	Overall	Main	Sub	
Reconstructive transformations (diffusion controlled, with slow rates of reaction)				
Ferrite	PF*	PF(GB)	PF(G)*	Grain boundary primary ferrite Allotriomorphic ferrite Polygonal ferrite Ferrite veins
			PF(NA)	Polygonal primary ferrite non-aligned
		PF(I)	PF(I)	Idiomorphic ferrite
Pearlite	P*	P*	FC(P)*	Lamellar pearlite Degenerate pearlite Fine colony pearlite
			FC*	Ferrite–carbide aggregate
Displacive transformations (shear dominated, with rapid rates of reaction)				
Widmanstätten ferrite	WF	WF(GB)	FS(A)*	Widmanstätten ferrite with aligned microphase Widmanstätten ferrite sideplates
			FS(NA)*	Widmanstätten ferrite with non-aligned microphase
		WF(I)	FS(I)	Intragranular Widmanstätten ferrite sideplates
			FP(I)	Intragranular Widmanstätten ferrite plates
			AF*	Widmanstätten acicular ferrite
Bainite	B	B(GB)	FS(A)*	Bainitic ferrite with aligned carbide Bainite sheaves
			FS(NA)*	Bainitic ferrite with non-aligned carbide
			FS(UB)*	Upper Bainite
			FS(LB)*	Lower bainite
		B(I)	FS(I) FP(I) AF*	Intragranular bainite sheaves Intragranular bainite plates Bainitic acicular ferrite
Martensite	M*	M*	M(L)*	Lath martensite
			M(T)*	Twin martensite

In low alloy weld metals, care has to be taken in identifying primary ferrite due to stereological effects. Ferrite allotriomorphs growing from prior austenite grain boundaries beneath the plane of observation may appear as polygonal ferrite grains in the intragranular regions. If these ferrite allotriomorphs are of a size approximately three times greater than those of surrounding acicular ferrite laths or grains, they are likely the constituent PF(I) described in the IIW scheme. It is unlikely that such large grains are idiomorphic ferrite, PF(I), nucleated on inclusions as referenced in the literature since the latter tend to nucleate at lower temperatures with relatively little time for growth.

Allotriomorphic ferrite morphologies were readily identified and also various sideplate morphologies (often classed as bainite). Widmanstätten ferrite was difficult to place but was regarded as a generically similar structure to bainite. Intragranular component phases such as acicular ferrite posed a much greater degree of difficulty (THEWLIS, 2004).

a) Allotriomorphic ferrite

When analyzing the Fe-Fe_3C diagram it is possible to see that austenite turns into perlite in a wide range of temperatures.

Allotriomorphic ferrite nucleates in the grain contours of the primary austenite at high temperatures (close to the A1 line) and grows laterally along the contour, and may even acquire the appearance of a ferrite shaft, as shown in Figure 3.16 (OLIVEIRA, 2014). Quasi-polygonal ferrite resembles allotriomorphic. The term “allotriomorph” means that the internal structure is crystalline, but the external aspect does not have straight faces (OLIVEIRA, 2014).

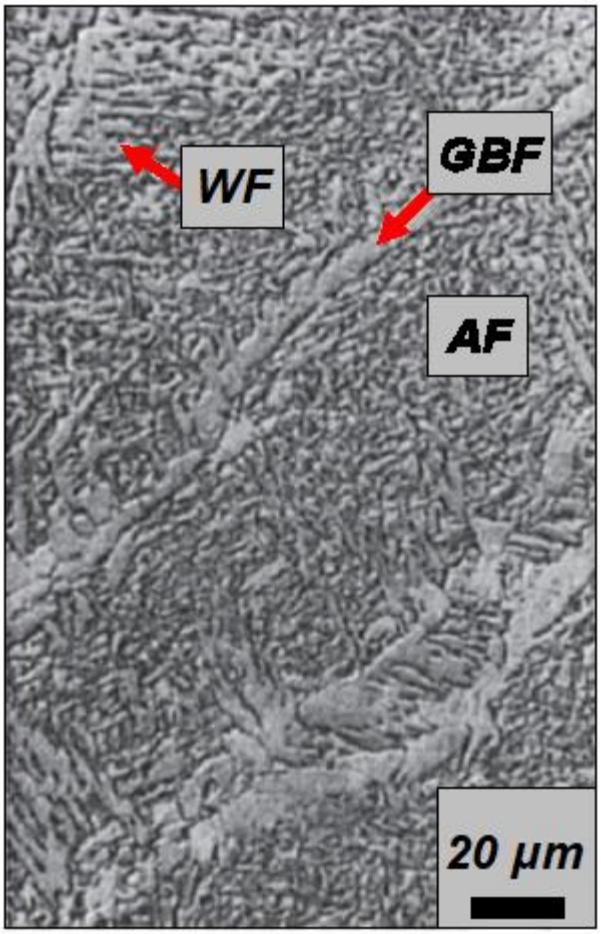

Figure 3.16 - Microstructure obtained in the scanning electron microscope of a welded steel joint Adapted from Bhadeshia and Honeycombe (2017).

Allotriomorphic ferrite usually nucleates along the austenite – austenite grain boundary (THEWLIS, 2004). It first grows laterally along the boundary and then can proceed perpendicularly into the austenite grain. The nucleation and growth involve a reconstructive process which the crystal structure change that leads to an absence of any macroscopic shape change, and only a volume change is observed. During nucleation, the allotriomorphic ferrite crystals exhibit a preferred orientation relationship with one of the austenite grains. The orientation relationship is usually of the Kurdjumov–Sachs (KS) type: $\{1\,1\,1\}_\gamma // \{1\,1\,0\}_\alpha$ and $\{1\,\bar{1}\,0\}_\gamma // \langle 1\,\bar{1}\,1\rangle_\alpha$ (TOTTEN, 2006).

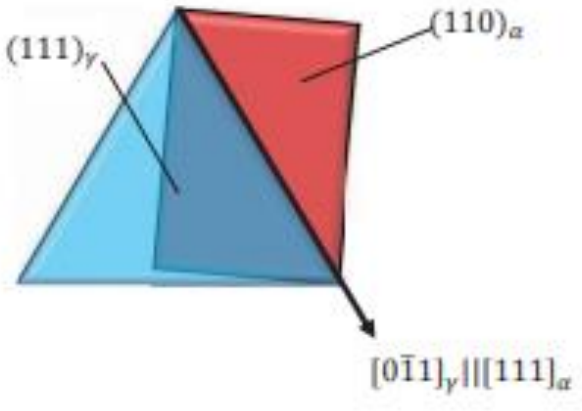

Figure 3.17 - Kurdjimov-Sachs orientations scheme (OLIVEIRA, 2014).

KS relationship indicates that the compacted planes of austenite and ferrite are parallel to each other and that the compacted directions of austenite and ferrite are parallel to each other. Eventually, the ferrite may deviate slightly from having parallel directions, as shown by the Nishiyama-Wasserman (NW) orientation relationship: $\{1\,1\,1\}_\gamma // \{1\,1\,0\}_\alpha$ and $\{11\,\bar{2}\}_\gamma // \langle 1\,\bar{1}\,0\rangle_\alpha$ (TOTTEN, 2006).

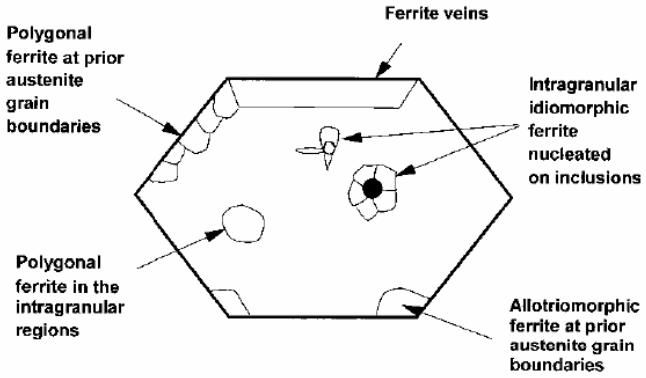

Figure 3.18 - Schematic representation of allotriomorphic and idiomorphic ferrites from an austenitic grain (THEWLIS, 2004).

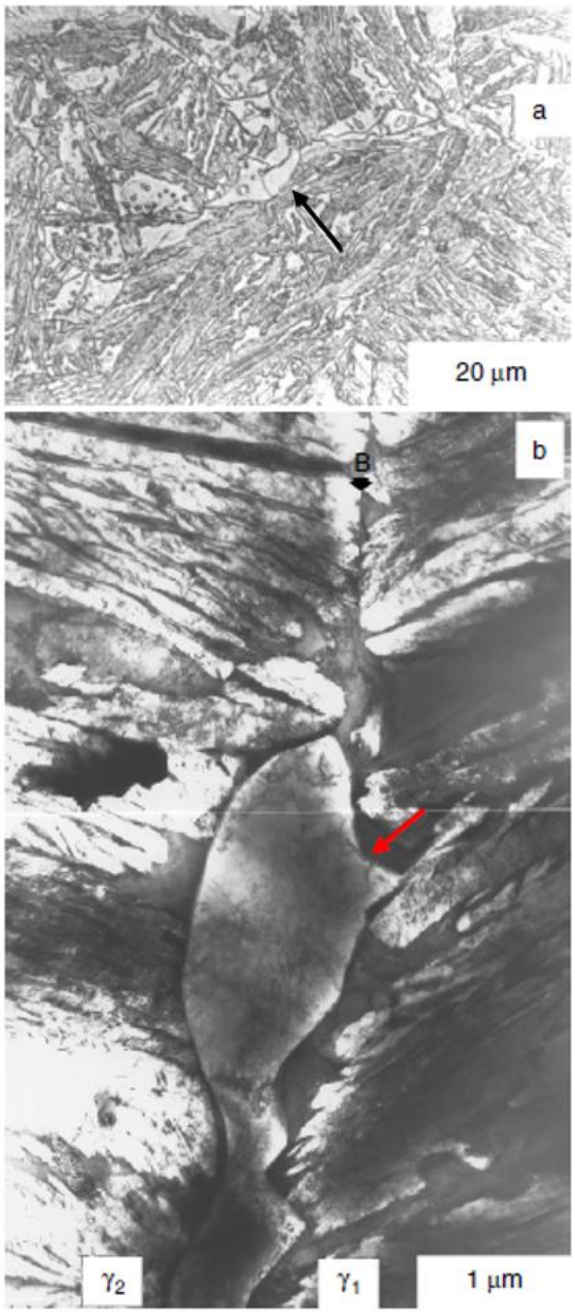

Figure 3.19 - (a) Optical micrograph showing the presence of allotriomorphic ferrite (marked by arrow) and bainite microstructure in an Fe–C–Si–Mn steel. (b) Transmission electron micrograph showing the presence of allotriomorphic ferrite along an austenite grain boundary (γ_1 and γ_2) marked by b. The orientation relationship between allotriomorphic ferrite and the g1 grain was close to a KS–NW orientation relationship and was in a random orientation relationship with the γ_2 grain (TOTTEN, 2006).

The KS or NW orientations allow for the existence of a semicoherent boundary between austenite and ferrite and thereby minimize the surface energy required to nucleate the ferrite at the austenite boundary (TOTTEN, 2006).

Firstly, the meaning of the term coherence in terms of atomic arrangement must be emphasized. A coherent interface occurs when two crystals fit perfectly in the interfacial plane so that the networks are continuous through the interface. This can only be achieved if the

interfacial plane has the same atomic configuration in both phases, which requires that the crystals are oriented in a special way in relation to each other. In a perfectly coherent interface, the atomic mismatch is accommodated by the elastic distortion of the networks. When the distance between the atoms at the interface is not identical, it is still possible to maintain coherence by expanding the atomic spacing. The result of the distortion of the networks is known as deformation of coherence (ANDRADE, 2003).

Semicoherent interfaces occur for high values of atomic mismatch or of interfacial area, which makes the creation of discrepancies to accommodate the mismatch in the interface energetically more favorable than the increase of elastic deformation in the network. The atomic mismatch between two networks, δ, can be accommodated by an arrangement of disagreements that generally occurs in two dimensions and the coherence stresses can be relieved if the interface has two non-parallel arrangements of disagreements with spacings $D_1 = b_1/\delta_1$ and $D_2 = b_2/\delta_2$, where b is the Burgers vector. If the spacing between the discrepancies is greater than D1 and D2, the stresses will be partially relieved and there will be long-range residual stress fields (ANDRADE, 2003).

When the interfacial plane presents a very different configuration in the union phases, there is no possibility of good crystallographic continuity around the interface. The pattern of atoms can be quite different in the two phases or, if similar, the interatomic distances must be different by a factor greater than 25%. In both cases, the interface is considered incoherent. In general, incoherent interfaces result when two crystals of different and randomly oriented structures come together in an interfacial plane (ANDRADE, 2003).

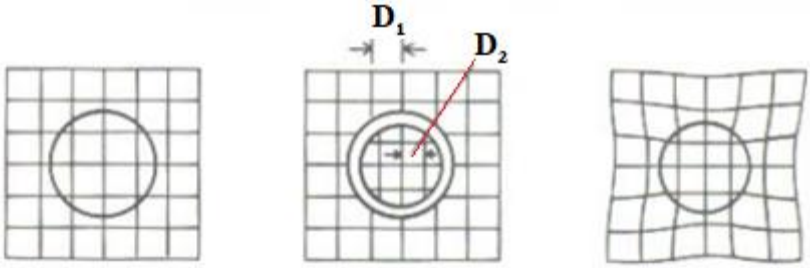

Figure 3.20 - Types of interfaces: a) coherent b) semicoherent and c) incoherent (ANDRADE, 2003).

Lower free energy is sufficient to satisfy the KS and NW orientations with one of the austenite grains for the nucleation of ferrite, and then the ferrite can grow into the adjacent austenite grain (γ_2) with no specific orientation relationship. On the latter side of the interface, which shows the random orientation, a disordered boundary will exist and rapidly grow into the austenite. Further detailed observation also showed small steps in the interface along the

protuberances on the γ_1 side of the allotriomorphic ferrite. However, the interface on the γ_2 side showed disordered boundary with no specific structure (TOTTEN, 2006).

The rate of growth on the γ_2 side is more rapid than that on the γ_1 side. The observed semicoherent boundary on only one side of the austenite grain also plays a critical role in the development of secondary Widmanstätten ferrite, which is described in the following section (TOTTEN, 2006).

b) Widmanstätten ferrite

Widmanstätten ferrite has the shape of side plates or slabs of ferrite and grows in austenite grains with a KS orientation ratio. Slat ferrite, which forms from the boundary of austenite grains, is referred to as primary Widmanstätten ferrite. The ferrite nucleated in the pre-existing allotriomorphic ferrite is called secondary Widmanstätten ferrite (TOTTEN, 2006). The nucleation of the secondary Widmanstätten ferrite occurs mainly at the semicoherent interphase boundary between ferrite and austenite.

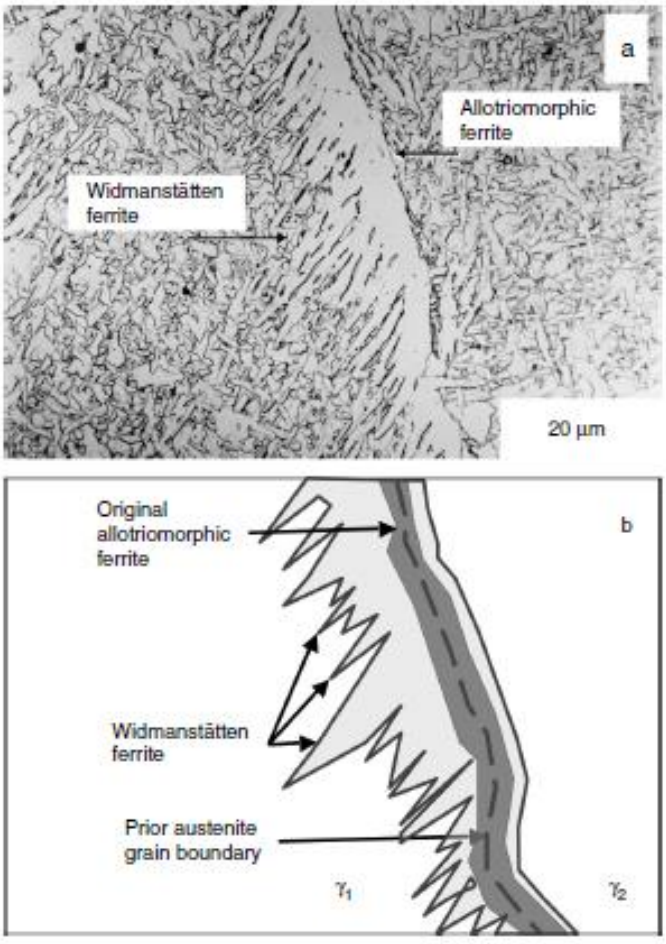

Figure 3.21 - A typical microstructure of the secondary Widmanstätten ferrite in a steel weld is shown in Figure 3.21a. A schematic illustration of an evolution of this microstructure is shown in Figure 3.21b (TOTTEN, 2006).

As the steel cools to a high temperature, the allotriomorphic ferrite forms with a KS-NW relationship with the austenite γ_1 grain and has a semi-coherent interface limit. With additional cooling, the secondary nucleus Widmanstätten ferrite on the γ_1 side of the allotriomorphic ferrite and grows in the austenite grain. This process of nucleation and growth leads to an apparent morphology of the sawtooth (TOTTEN, 2006).

Two growth mechanisms of Widmanstätten ferrite have been proposed. In the first mechanism, the growth is attributed to the lateral movement of semicoherent interfaces by small steps (ledges) in the interface (TOTTEN, 2006). In the second mechanism, the Widmanstätten ferrite may grow through a displacive transformation mechanism (BHADESHIA, 1981). Many experimental results are in agreement with the second mechanism (TOTTEN, 2006). Thin, wedge-shaped Widmanstätten ferrite is produced due to cooperative back-to-back growth of two ferrite crystallographic variants. The Widmanstätten ferrite plates grow into untransformed austenite by extension along their length. Since Widmanstätten ferrite forms at temperatures well below that for allotriomorphic ferrite, growth occurs by a paraequilibrium mode (i.e., the ratio of the iron concentration to the substitutional atom concentration is frozen in both the parent and the product phases). The rate of growth is controlled only by carbon diffusion in the austenite ahead of the plate. It is possible to estimate the growth rate of Widmanstätten ferrite with diffusion-controlled growth models of Bhadeshia, Svensson, Gretoft (1985) by considering only the carbon diffusion.

c) Acicular ferrite

Acicular ferrite is formed by nucleating in an intragranular and heterogeneous way, mainly from non-metallic inclusions, often present in welded regions of low alloy steels. The presence of alloying elements and non-metallic oxides favors the formation of inclusions in these steels. In joints welded by electric-arc, elements such as silicon, manganese and oxides give rise to inclusions in the order of 10^{18} m^3, with a size greater than 0.05μm and an average size of 0.4μm (BHADESHIA, 2001).

The first studies regarding acicular ferrite show that the formation process of this microstructure is predominantly triggered by shear, just as it occurs in the formation of the bainitic microstructure. However, this displacement transformation is followed by a diffusional stage. Acicular ferrite initiates nucleation at sites in the intragranular region of austenite through shear transformation, without modification of composition, that is, without diffusion. In the next stage, growth occurs with the formation of secondary nuclei from the interface of the initially formed ferrite (CASTRO, 2012).

Acicular ferrite is formed at a relatively high temperature, forcing excess carbon atoms to migrate from the acicular ferrite formed to the remaining austenite to reestablish the composition balance. Finally, the reaction is stopped when the carbon-enriched austenite reaches equilibrium for the temperature at which the reaction occurs (CASTRO, 2012).

Both acicular ferrite and bainite can be formed from the same isothermal treatment under identical conditions in the same steel with the presence of inclusions (BHADESHIA, 2001). However, bainite is preferentially formed when the austenitic grain size is small, as its nucleation occurs preferably from the contours and grows towards the interior of the austenite grain, suppressing the nucleation of the acicular ferrite. When the grain size of the austenitic microstructure is large, the number of inclusions density becomes high when compared to the nucleation sites in the grain boundaries, thus favoring the intragranular formation of the acicular ferrite (CASTRO, 2012).

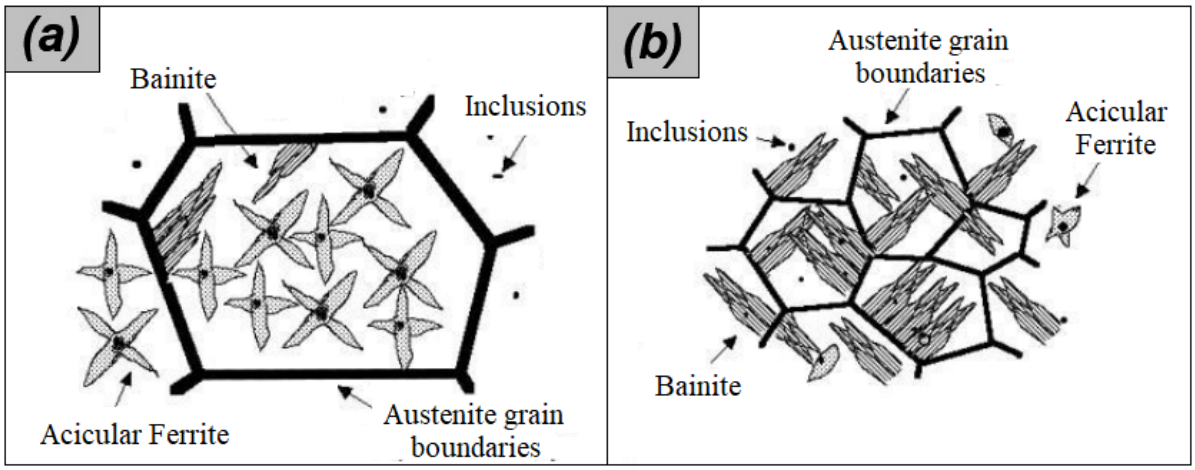

Figure 3.22 -Effect of austenite grain size on the development of steel microstructure with the presence of inclusions: (a) large austenitic grain and (b) small austenitic grain. Adapted from Bhadeshia (2001b).

Acicular ferrite is recognized as an intragranular nucleated morphology of ferrite in which there are multiple impingements between grains (BHADESHIA, 2015). The type of ferrite nucleates on inclusions inside the prior austenite grains during the $\gamma \rightarrow \alpha$ transformation. Provided there is a high density of inclusions, a fine interlocking structure (generally <5 mm) can be produced (THEWLIS, 2004).

Acicular ferrite was thought to be a single transformation product for a long period of researches (THEWLIS, 2004). Early researches (RICKS; HOWELL; BARRITTE, 1982) suggested that it was intragranularly nucleated Widmanstätten ferrite and later work (BHADESHIA, 2015) provided evidence for intragranularly nucleated bainite. However, recent

research by Thewlis, Whiteman and Senogles (1997) has demonstrated that the nature of acicular ferrite may be as shown schematically in Figure 3.23.

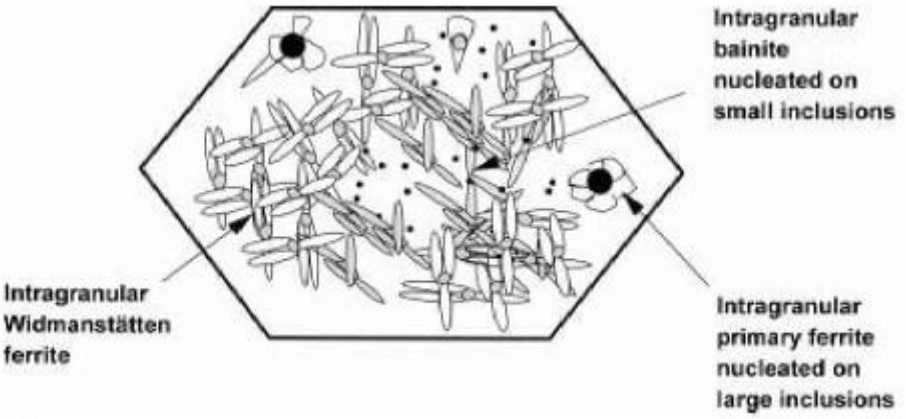

Figure 3.23 - Schematic representation of components of acicular ferrite grain formed from an austenitic grain (THEWLIS, 2004).

Different reaction products may nucleate on intragranular inclusions at reconstructive and displacive transformation temperatures during continuous cooling depending on the origin, size and amount of inclusions grain (THEWLIS, 2004). Acicular ferrite results from multiple influences of the different transformation products and the sequence of transformations is consistent with the theoretical activation energy barrier to nucleation of the different sites. Acicular ferrite development may thus be defined in terms of conventional steel transformation products and CCT diagrams incorporating both intragranular and grain boundary transformations. Under continuous cooling transformation conditions: AF = PF(I) + WF(I) + B(I) (THEWLIS, 2004). This leads to acicular ferrite that may have a variety of forms depending on steel composition, cooling rate and inclusion characteristics. Figure 3.24 shows that acicular ferrite may consist of mixtures of different intragranular transformation products (THEWLIS; WHITEMAN; SENOGLES, 1997).

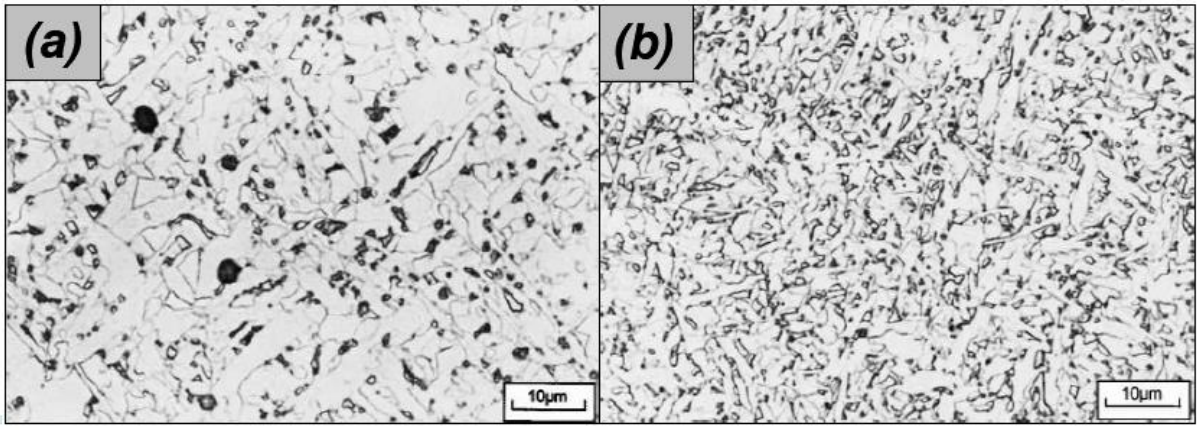

Figure 3.24- Two forms of acicular ferrite: (a) intragranular primary ferrite – Widmanstätten ferrite in C–Mn weld metal and (b) intragranular Widmanstätten ferrite – bainite in Ti –Mo–B alloyed weld metal. Adapted from Thewlis (2004).

Acicular ferrite is usually observed as a fine interlocking ferrite structure interspersed with microphases (see Figure 3.24). Alternatively, Widmanstätten acicular ferrite (RICKS; HOWELL; BARRITTE, 1982) or bainitic acicular ferrite may form by itself (BHADESHIA, 2015). However, if reactions are completed at purely reconstructive transformation temperatures, it may be preferable to use the term idiomorphic primary ferrite instead of acicular ferrite to describe the microstructure, since intragranular primary ferrite is likely to be coarse and non-acicular in morphology. Idiomorphic ferrite nucleates inside austenitic grains, usually in non-metallic inclusions present in steels (see Figure 3.25). It forms without contact with the surface of the austenitic grain (THEWLIS, 2004; BHADESHIA; HONEYCOMBE, 2017).

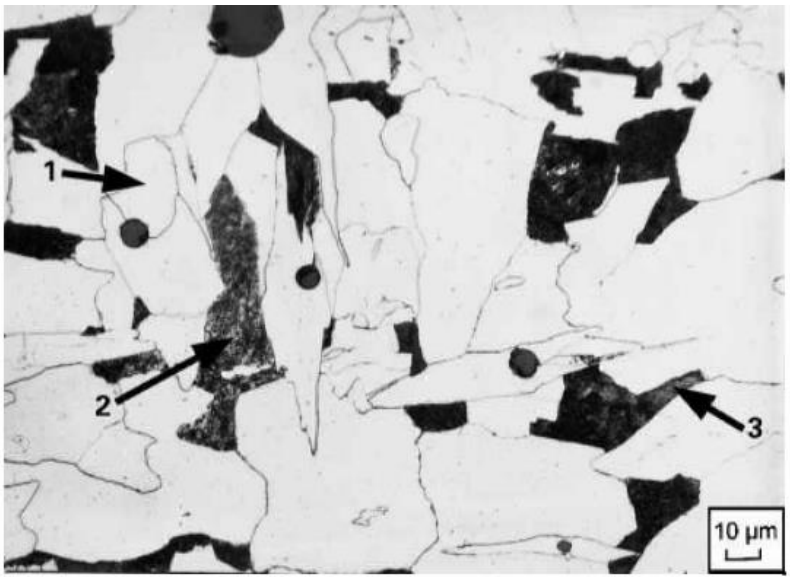

Figure 3.25 - Intragranular primary ferrite and pearlite in as cast, 0.13%C, 2.0%Mn, cerium sulfide particle dispersed steel where (1) indicates idiomorphic ferrite, (2) indicates ferrite - carbide aggregate and 3 indicates irresolvable pearlite Thewlis (2004).

The shape of the ferrite plates may not appear to exactly needles as the use of the term ‘acicular’ would imply. This is because the different ferrite morphologies cannot grow very far before mutual hard impingement. It is evident from Figure 3.24 that the degree of refinement of the acicular ferrite is dependent on the nature of the transformation products inherent in its formation (THEWLIS, 2004).

Distinguishing the intragranular transformation products that compose acicular ferrite, AF in the IIW scheme, is likely to be very difficult compared with identifying the structure itself. It is recommended, therefore, that for the purposes of calibrating models, a pragmatic solution be adopted. Thus, measured volume fractions of acicular ferrite should be compared with the sum of the intragranular constituents PF(I) + WF(I) + B(I) predicted by modeling. However, care should be taken to distinguish between acicular ferrite, AF, where multiple

existence among the different intragranular ferrite morphologies, and the intragranular transformation products PF(I), WF(I) and B(I), which may grow relatively unimpeded and may be identified in their own right (THEWLIS, 2004).

d) Polygonal Ferrite

Polygonal ferrite is normally considered to be one of the simplest microstructures of Fe-Fe_3C system, and is usually is not fully studied for mechanical property analysis. Frequently, the grain size of the polygonal ferrite is the only feature which is measured. Since polygonal ferrite is formed at relatively high temperatures the dislocation density is often overlooked when considering contributions to strength. The strength is normally assumed to be caused by the combination of grain size and solutes (WU et al., 2007).

If austenite has a grain size much larger than the ferrite being formed in its contours and there are sites for intragranular nucleation, ferrite grains can be formed inside the austenite (CASTRO, 2012). The transformation of polygonal ferrite from austenite is in general controlled by diffusion of carbon and substitutional alloying elements, it proceeds relatively slowly (KIM; LEE; KIM, 2008). Nevertheless, the formation of polygonal ferrite is related in some way to the evolution of the microstructure of the acicular ferrite. The formation of acicular ferrite can be characterized as a two-stage reaction: (i) nucleation of acicular ferrite and (ii) the coarsening of pre-existing acicular ferrite and the formation of polygonal ferrite near prior-austenite grain boundaries (KIM; LEE; KIM, 2008).

Kim, Lee and Kim (2008) submitted samples of a steel Fe + 0.05C + 0.24Si + 1.7Mn + 0.05 (Ti + Nb) + 0.25Ni + others to dilatometric analysis with predominant microstructure of acicular ferrite and found that the time required for the decomposition of austenite into acicular ferrite for a temperature of 600 ºC it was 13s. This means that the reaction occurs in a very short time when compared to diffusion reactions, strengthening the conclusion that it is a predominantly shear reaction. However, the subsequent diffusion of carbon from ferrite to austenite is not excluded (CASTRO, 2012).

Analyzing the transformed fraction of acicular ferrite in the isothermal treatment at 600 ºC Kim and the guys demonstrated that after 50 s, having already formed the acicular ferrite, the growth of the grains occurs and starts, starting from the grain contours of the primary austenite, the formation of polygonal ferrite. According to Castro (2012), the transformation of the acicular ferrite can be understood as a reaction in two stages in which the transformation of

the acicular ferrite, of a shearing character, first occurs, followed by a reaction of a diffusional character.

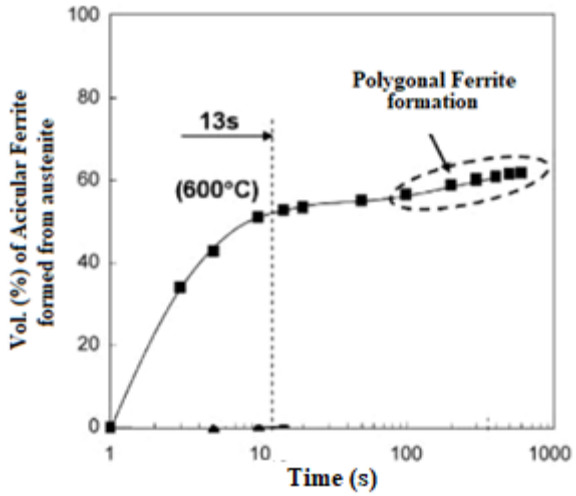

Figure 3.26 - Transformation of acicular ferrite during isothermal treatment at 600 ºC followed by the formation of polygonal ferrite. Adapted from Kim, Lee and Kim (2008).

The CCT diagram showed by Tang and Stumpf (2008) conducted a study where the samples were solubilized at 1225 ºC for 15 min., followed by cooling to 980 ºC at a cooling rate of 5 $ºCs^{-1}$ and maintained at that temperature for 5 min. before being cooled continuously at rates of 0.1 to 20 $ºCs^{-1}$. This work confirms that the acicular ferrite is obtained at around 600 ºC, with a cooling rate ranging from 15 to 0.1 $ºCs^{-1}$ (see Figure 3.27). Figure 3.27 also shows that polygonal ferrite is obtained at temperatures above 600 ºC, with a cooling rate below 5 $ºCs^{-1}$, which hardly occurs in welding processes without post-heating treatment.

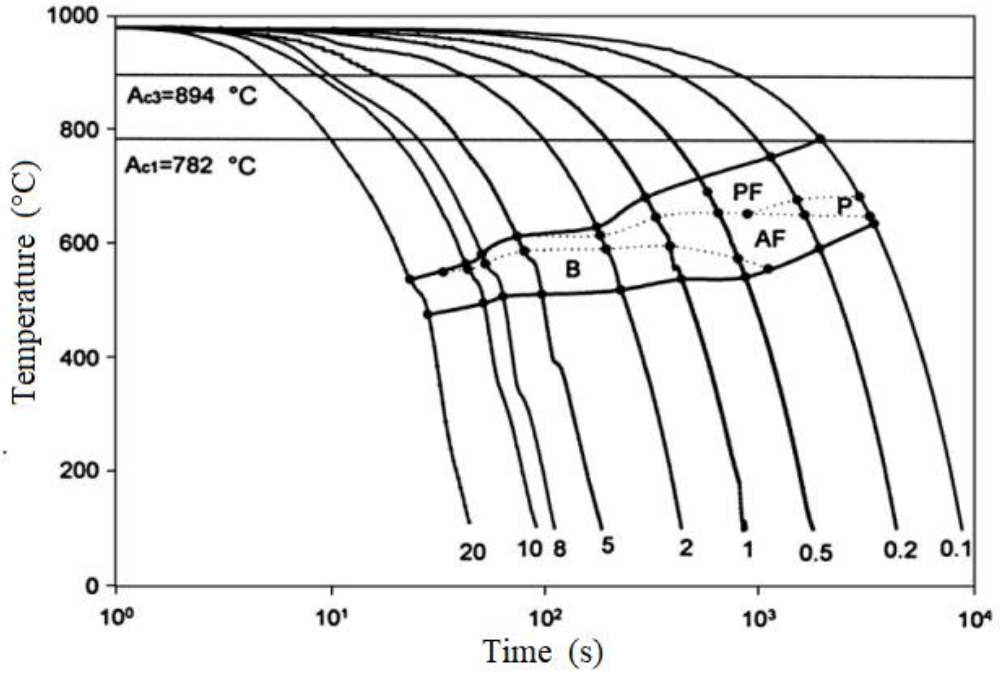

Figure 3.27 - CCT diagram for Fe-0.05C-0.025Si-1.14Mn-0.22Mo-0.055Nb0.021Ti-0.065Al steel. P = pearlite, B = bainite, AF = acicular ferrite, PF = polygonal ferrite (TANG; STUMPF, 2008).

Figure 3.28 represents the microstructural evolution and nucleation stages of ferrite in the weld metal. This diagram confirms that the cooling rates in welds are high to the point of promoting the nucleation of intergranular acicular ferrite in austenite instead of polygonal ferrite.

During welding, in the melting pool, dissolved oxygen and deoxidizing elements react in the molten material (between 2000 - 1700 ºC) and form inclusions of oxides (see Figure 3.28a) with an average size of 0.1 to 1 μm (CASTRO, 2012). Figure 3.28b shows the solidification step of the weld joint where δ ferrite (CCC) solidifies (at temperatures between 1700-1600 ºC) and then becomes austenite, phase γ (CFC). Oxide inclusions play a fundamental role in this step because they actively participate in the heterogeneous nucleation of austenitic grains. The inclusions content provides a greater surface area of the substrate for the formation of austenite grains to occur (CALLISTER JR., 2008). Thus, the inclusions act as refiners of austenite grains, which will be very important for the final microstructure of the joint. In the temperature range between 1200 and 800 ºC, Figure 3.28c, austenite grains may grow. Between 800 and 300 ºC (see Figure 3.28 (d) to (g)) austenite decomposes into ferrite (CCC) with different morphologies. This transformation begins with the nucleation (Figure 3.28d) and growth (Figure 3.28e) of allotriomorphic ferrite in the grain contours of austenite. Figure 3.28f shows Widmanstätten ferrite nucleation at the α/γ grain boundaries and extends into the interior of the untransformed austenite grain as cooling continues. Subsequent cooling, at low

temperatures, provides the nucleation of the acicular ferrite in the inclusions (see Figure 3.28g). If there are not enough inclusions, the formation of bainitic ferrite instead of acicular ferrite will occur from the remaining austenite. With subsequent cooling, to temperatures close to room temperature, part of the austenite can be completely or partially transformed into martensite. This mixture of Martensite-Austenite phases is called MA constituent.

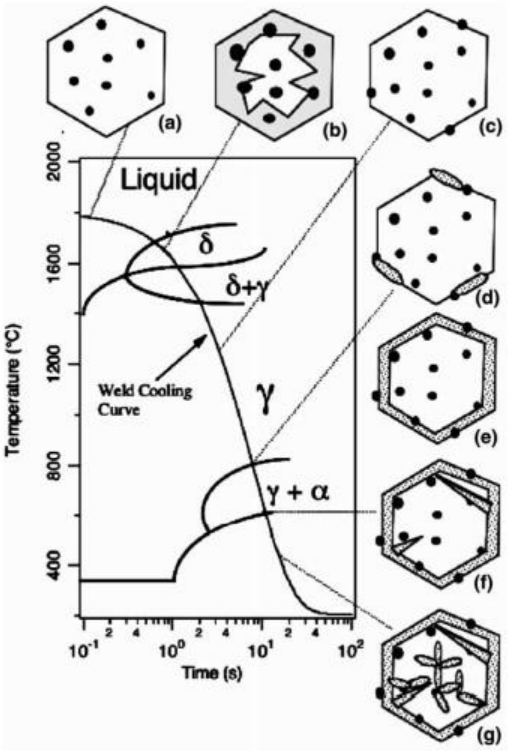

Figure 3.28 - Schematic weld metal cooling curve and a hypothetical continuous cooling transformation diagram shows different phase transformations that may occur as the weld metal cools to room temperature (BABU, 2004).

An important variation of polygonal ferrite is called massive ferrite (or quasi-polygonal ferrite). The microstructure of the almost polygonal ferrite is characterized by the existence of coarse ferrite plates whose contours are irregular and wavy. Its formation occurs at a temperature range of 610 to 670 ° C. Quasi-polygonal ferrite is sometimes called massive ferrite due to its formation occurring from a transformation controlled by several crystal interface processes with different structures and with similar compositions (massive transformation) (OLIVEIRA, 2014). In addition, this transformation occurs without any relationship of crystallographic orientation during rapid cooling. Thus, the short-range diffusion between the austenite and ferrite interfaces results in the same composition between these two phases. As the growth is mainly carried out by a non-cooperative atomic transfer through an incoherent high-energy interface, ferrite consumes the primary grains and grows at a high rate of equal rate in all directions (OLIVEIRA, 2014).

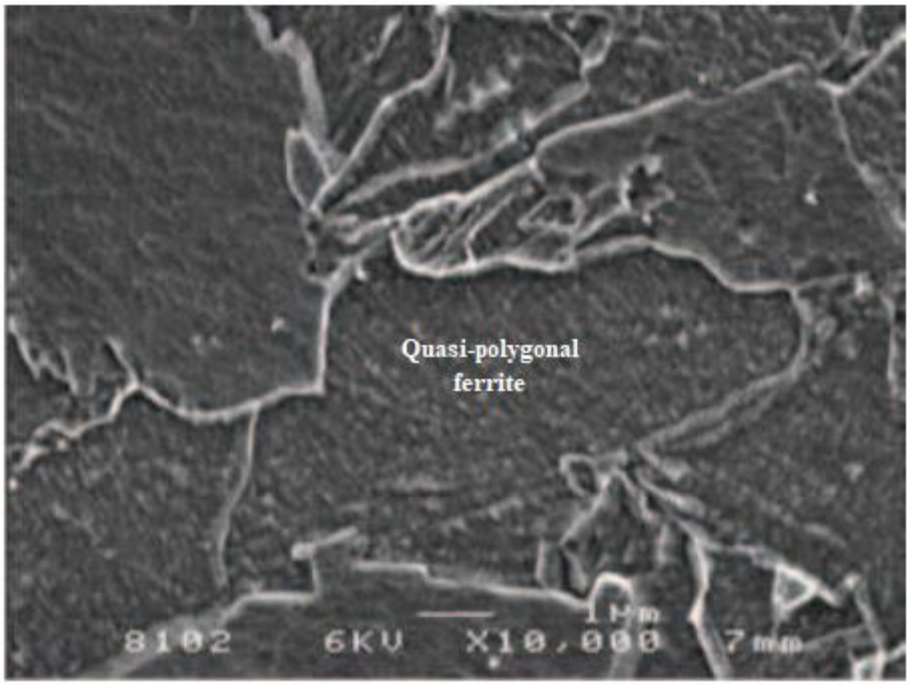

Figure 3.29 - Quasi-polygonal ferrite formed in an AISI 1144 steel. Adapted from (OLIVEIRA, 2014).

Upper bainite, on the other hand, forms at temperatures similar to the formation of acicular ferrite, occurring mainly in welds with high cooling, very low oxygen content, or very high alloying element content (MODENESI, 2012). Under the optical microscope, it is presented as a series of ferrite sheets, formed from the austenitic grain contours, or the grain contour ferrite. It is also observed the existence of carbon-rich constituents between the blades and is very similar to Widmanstätten ferrite.

When observed by electron microscopy, the upper bainite it can, generally, be distinguished by presenting a greater density of crystalline defects (displacements) and, in general, an internal precipitation of carbides. Like Widmanstätten ferrite, upper bainite is generally undesirable because it has low toughness.

e) Ferrite with aligned second phase (FS(A)) and ferrite with non-aligned second phase (FS(NA));

The microstructure of FS(A) consists of two or more parallel ferrite plates. If there are only two plates, the aspect ratio must be greater than 4: 1. If the operator is safe, this constituent can be subclassified as a ferrite side plate, upper bainite or bottom, FS(SP), FS(UB) or FS(LB).

This morphology comprises constituents that tend to have a very similar appearance when observed by optical microscopy, particularly Widmanstätten ferrite and bainite (in general, superior bainite) (MODENESI, 2012). Both constituents can nucleate and begins to

growth directly from the austenite grain boundary or from previously formed grain boundary ferrite grains (see Figure 3.30).

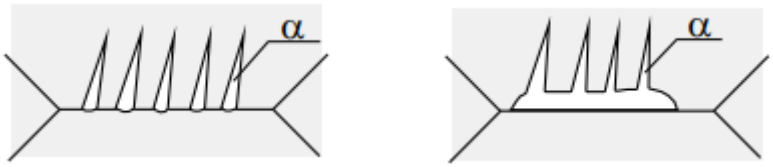

Figure 3.30 - Schematic representation showing the morphology of the ferrite side plates in an austenitic matrix. (MODENESI, 2012).

The austenite regions between the plates of Widmanstätten ferrite undergo an increase in carbon content during their growth and give rise to adjacent regions of perlite or other carbon-rich constituents. The formation of this microstructure is favored by larger grain size of austenite, by intermediate carbon levels (between 0.2 and 0.4 wt.%) and, mainly, by super-cooling, in relation to the A3 temperature, greater than the one associated with the formation of bainite (MODENESI, 2012).

The microstructure composed of Widmanstätten ferrite has relatively coarse grains with small crystalline orientation differences between them. Furthermore, it is observed the presence of films of carbon-rich constituents and fragile in their contours. This fact, together with the characteristics described above, that this form of ferrite is considered to have little desired characteristics in the weld ZF that must have a high tenacity (MODENESI, 2012).

The FS(NA) is constituted of ferrite completely involving or:

- "microphases" (carbides or the constituent AM - austenite-martensite) approximately equiaxial and randomly distributed or;
- grains of acicular ferrite.

FS(NA) resembles bainite, However, its microstructure may be a product of a particular cut of bainite packages (the microstructure develops in three dimensions and what is observed under the microscope is only a two-dimensional section of it) (MODENESI, 2012).

Figure 3.31 shows examples of microstructures with several of the microconstituents described above. It is possible to observe the distinction between FS (A) and FS (NA).

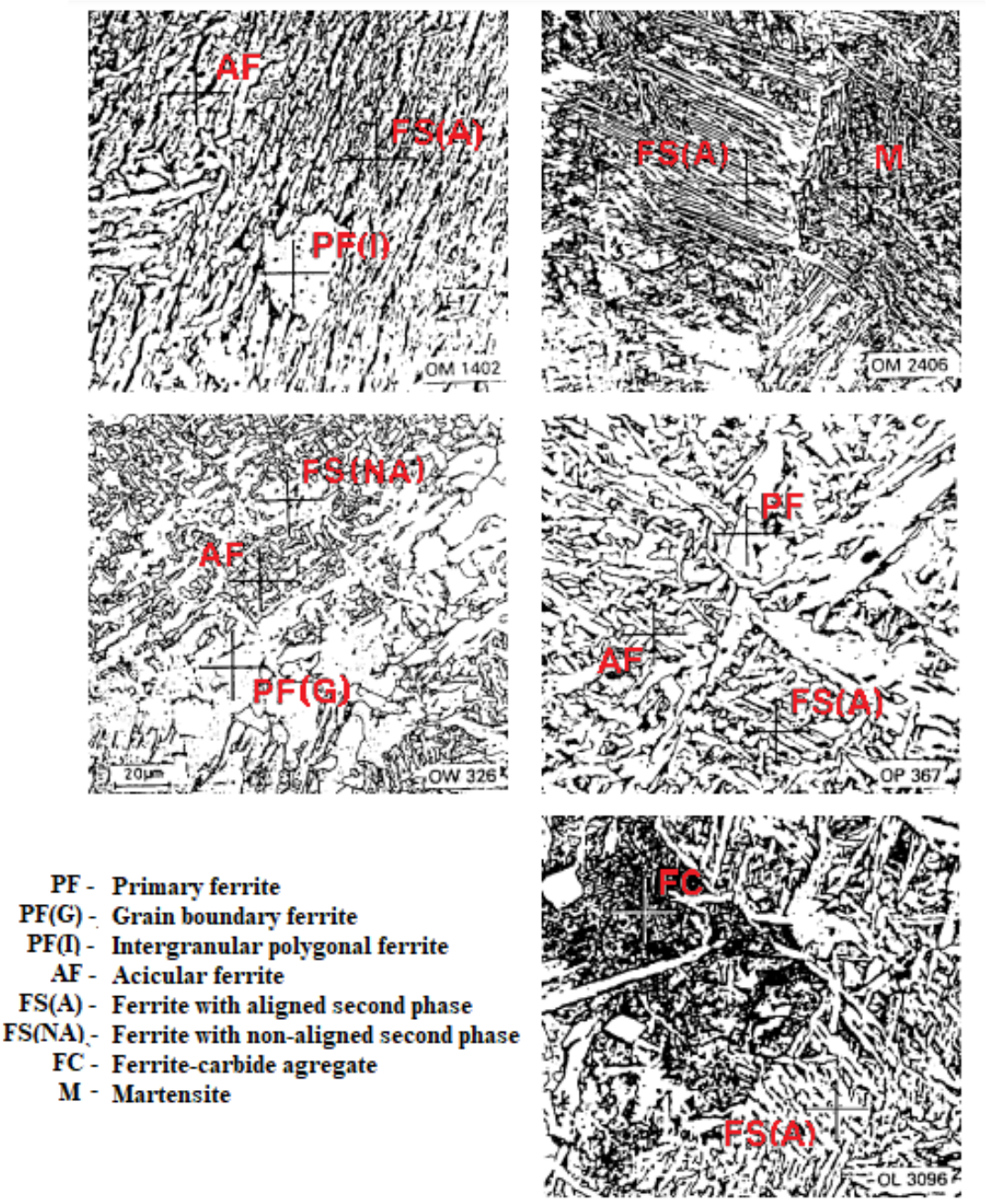

Figure 3.31 - Microstructure of the unaltered weld metal showing different microstructural constituents. Adapted from Modenesi (2012).

Figure 3.32 and Figure 3.33 present diagrams to help researchers and operators to identify, respectively, grain boundary and intragranular phases and microconstituents previously discussed.

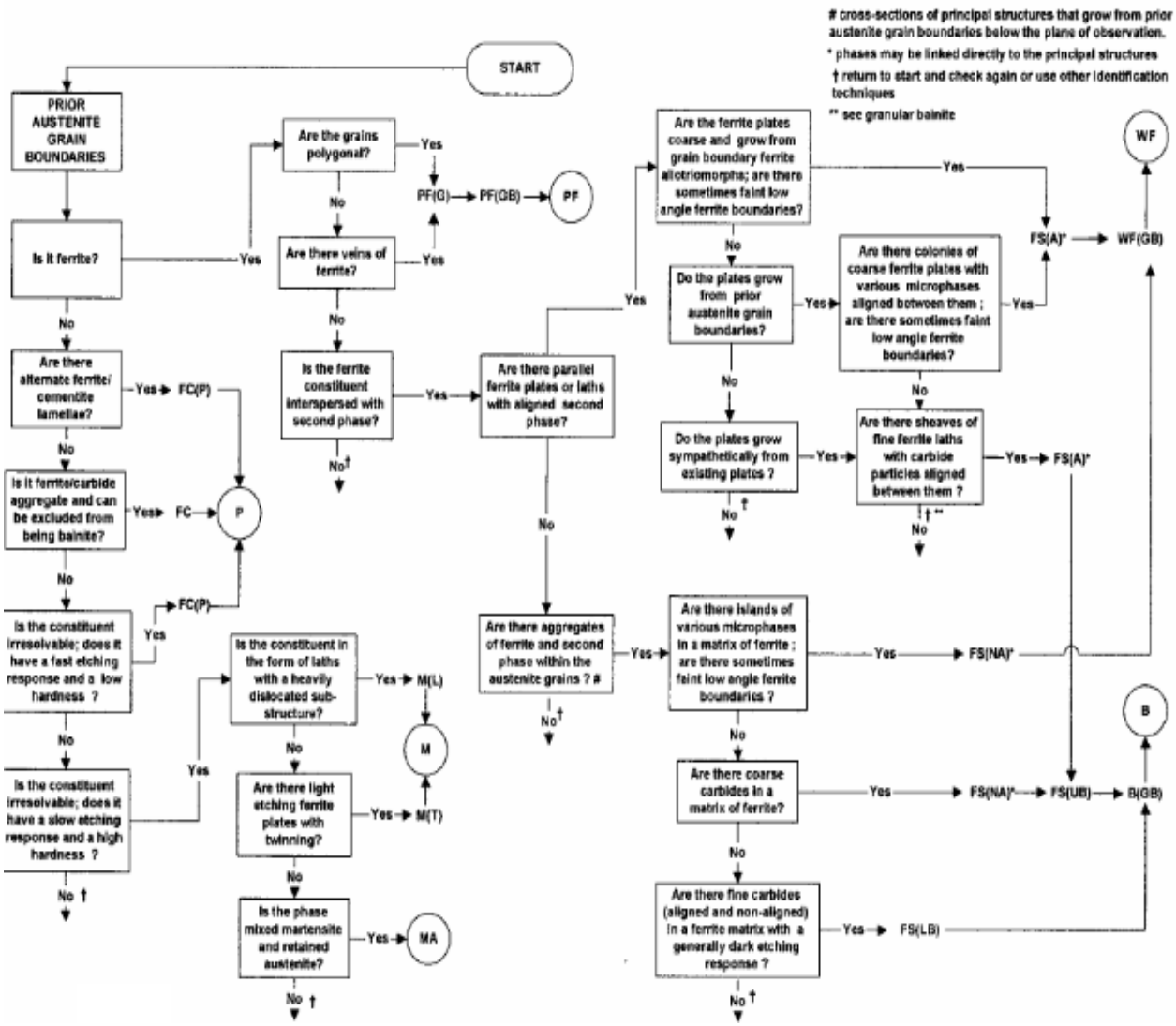

Figure 3.32 - Scheme for identification of prior austenite grain boundary constituents. Adapted from Thewlis (2004).

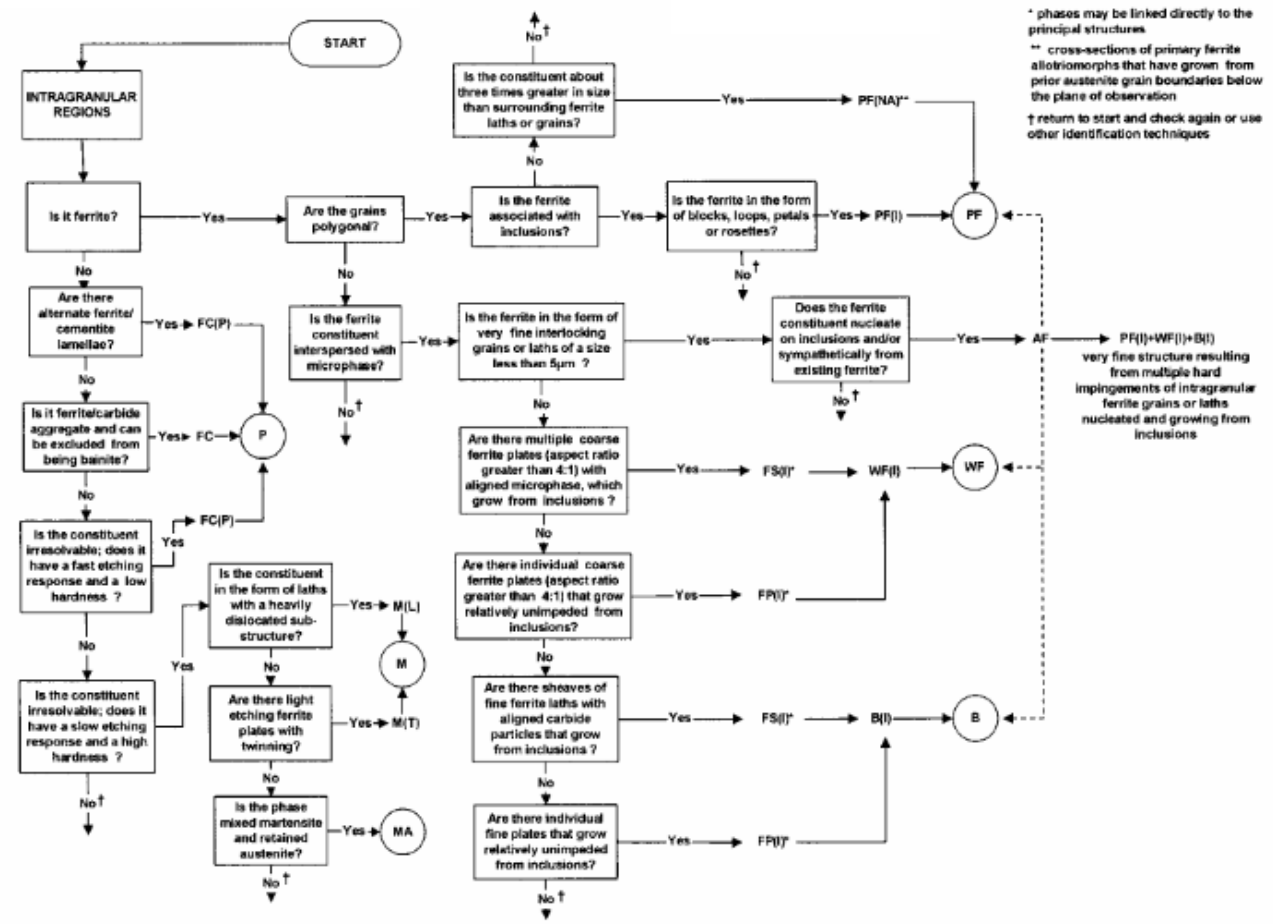

Figure 3.33 - Scheme for identification of intragranular constituents. Adapted from Thewlis (2004).

3.2.2. Solidification of the welding pool

For there to be a transformation between two determined phases, the final phase must be surrounded by an initial phase in a metastable (or supersaturated) state. However, this does not mean that the phase transformation will be instantaneous (PASQUA, 2003). The time interval of a phase stays in a metastable state reveals the fact that such a state must overcome an energy barrier to achieve stability.

The solidification process essentially involves two stages: nucleation and growth of the nuclei. The nucleation stage involves the appearance of small regions with an ordered arrangement of atoms (in metallic materials) or molecules (for other types of materials) up to a certain size and their stabilization as nuclei. The growth stage is defined as the increase in the size of the nuclei thus forming crystals of the new phase (MANRICH; ZANOTTO; HAGE JR., 1992).

The two main nucleation mechanisms are defined as homogeneous nucleation and heterogeneous nucleation. Homogeneous nucleation occurs in some materials of high purity. In this mechanism, which occurs under specific thermodynamic conditions, the very disordered movement of atoms or molecules results in the organization of the material's structure (CALLISTER JR., 2008). On the other hand, in heterogeneous nucleation, the ordering process is catalyzed due to the presence of heterogeneities, or substrates present at the solid-liquid interface (MANRICH; ZANOTTO; HAGE JR., 1992).

a) Homogeneous nucleation

In crystalline materials, below the melting temperature the free energy (G) of the solid state is lower than that of the liquid state (MANRICH; ZANOTTO; HAGE JR., 1992). Free energy is a function of other thermodynamic parameters, including the internal energy of the system measured through enthalpy (H), entropy (S) and temperature (T) (CALLISTER JR., 2008). An important analysis in the study of phase transformation in materials is the variation of the free energy of the system (ΔG). In a system that undergoes a phase transition, the process will occur spontaneously only if ΔG is negative (CALLISTER JR., 2008).

$$\Delta G = H - T\Delta S \qquad \text{(Eq. 3.1)}$$

For the case of transformation of phases into a substance, there is the variation of the energy free ΔG, which can be described by (Eq. 3.2).

$$\Delta G = G_s - G_L \qquad \text{(Eq. 3.2)}$$

Where G_S is the free energy of the solid, G_L is the free energy of the liquid (SILVA, 2015). The phase transition process begins with the formation of a cluster of unit cells of the new phase (or embryo) of radius r. Upon overcoming a critical radius (r*) and capable of overcoming the energy barrier, the embryo is treated as a critical nucleus and when r is greater than the measure of r*, the nucleus nomenclature is adopted (PASQUA, 2003).

In phase transformations, it is not possible to take into account only the free volumetric energy associated with each phase, as there is an interfacial surface being generated separating the crystal from the liquid (MANRICH; ZANOTTO; HAGE JR., 1992). When considering the formation of a solid phase embryo inside the liquid phase presenting spherical geometry, atomic packaging similar to that found in the solid phase (CALLISTER JR., 2008) and without changes in the chemical composition (MANRICH; ZANOTTO; HAGE JR., 1992), the barrier (ΔG*)

will be the sum between the reduction of volumetric free energy per volume unit (ΔG_V) and the increase in specific surface free energy (σ) accordingly Figure 3.34.

$$\Delta G = \frac{4}{3}\pi r^3 \Delta G_V + 4\pi r^2 \sigma \qquad \text{(Eq. 3.3)}$$

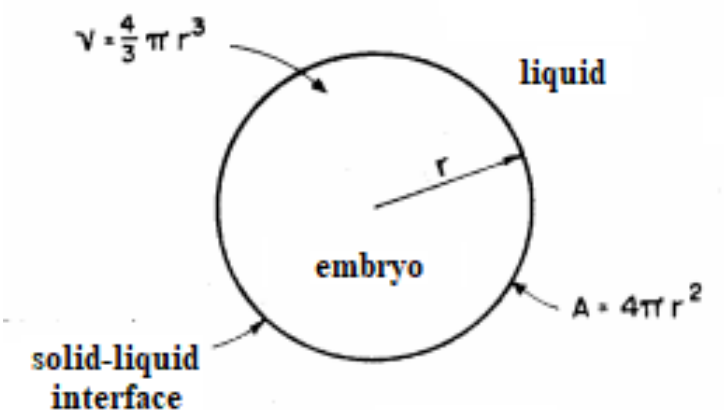

Figure 3.34 - Representation of a crystalline embryo with radius r, formed by cooling the liquid of the same chemical composition. Adapted from composition Manrich, Zanotto and Hage Jr. (1992).

As the free volumetric energy of the crystalline phase is always less than the liquid phase, ΔG_V always assumes negative values. Thus, the first term of the (Eq. 3.3 always decreases by establishing a relationship with r^3. The solid/liquid surface free energy, in turn, always assume positive values leading to an increase proportional to r^2 of the second term of the (Eq. 3.3 (MANRICH; ZANOTTO; HAGE JR., 1992). It can be inferred from these statements that, as a result of this sum, ΔG increases at first, reaches a critical value ΔG_V * at a radius r * and only then decreases with the increase of the nucleus (see Figure 3.35).

The growth stage starts only in embryos that become nuclei (with size greater than or equal to r *), because in these conditions there is a reduction of dG with the increase of r. The value of r * varies according to the degree of supercooling (dT). Supercooling is defined as the difference between the fusion temperature (T_F) and the material temperature (T) at a given position (MANRICH; ZANOTTO; HAGE JR., 1992).

$$\Delta T = T_F - T \qquad \text{(Eq. 3.4)}$$

The greater the supercooling, the smaller the measure of r *, since the difference in free volumetric energy between the liquid and the solid is greater.

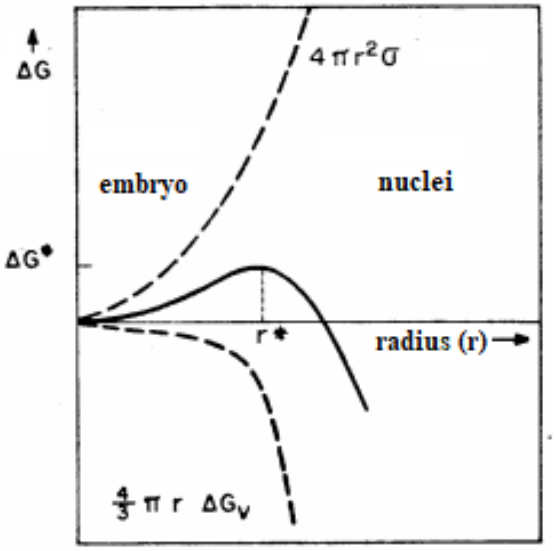

Figure 3.35 - Variation of the free energy of the system, of the free volumetric energy and of the free surface energy according to embryo radius. Adapted from composition Manrich, Zanotto and Hage Jr. (1992).

b) Heterogeneous nucleation

The heterogeneous nucleation of the material on surfaces occurs more frequently than the homogeneous one. These surfaces are characterized by the container that holds the liquid, impurities present in the material or agents added intentionally in order to increase the nucleation rate (MANRICH; ZANOTTO; HAGE JR., 1992).

In this nucleation mechanism, a radius of curvature of the embryo greater than r* is obtained with less free solid-liquid interfacial energy, compared to that required for homogeneous nucleation, as shown in Figure 3.36 (MANRICH; ZANOTTO; HAGE JR., 1992).

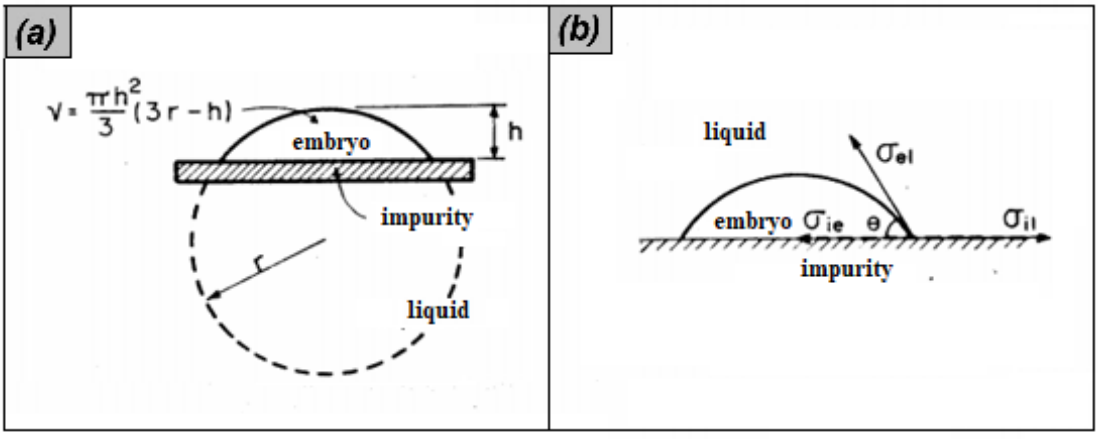

Figure 3.36 - Schematic representations (a) of the formation of an embryo on an impurity particle and (b) of the surface tension components acting. Adapted from composition Manrich, Zanotto and Hage Jr. (1992).

In this case, the thermodynamic barrier is reduced by the existence of surfaces that have good “wettability” by the liquid and the solid. The total free energy is obtained by (Eq. 3.5),

where V is the volume of the embryo/nucleus, A_{eL} is the surface area of the embryo/liquid boundary, and σ_{eL}, σ_{ei} and σ_{iL} are, respectively, the surface tension values in embryo/liquid, embryo/impurity and impurity/liquid interfaces (MANRICH; ZANOTTO; HAGE JR., 1992).

$$\Delta G = V\Delta G_V + A_{eL}\sigma_{eL} + \pi r^2\sigma_{ei} - \pi r^2\sigma_{iL} \quad \text{(Eq. 3.5)}$$

Applying the trigonometric relation in which $\sigma_{eL}\cos\theta = \sigma_{iL} - \sigma_{ei}$, the ASBAA equation can be rewritten as (Eq. 3.6).

$$\Delta G = V\Delta G_V + A_{eL}\sigma_{eL} + \pi r^2\sigma_{ei} - \pi r^2\sigma_{iL} \quad \text{(Eq. 3.6)}$$

In heterogeneous nucleation, the σ_{eL} value is much lower than sigma in homogeneous nucleation, providing smaller nuclei. In addition, nuclei from heterogeneous nucleation are more easily formed and at lower levels of supercooling. Therefore, in heterogeneous nucleation, a crystalline embryo that forms on a substrate reaches the critical radius with fewer atoms or molecules, as well as with less increase in surface free energy.

During a process of depositing metal through welding, with the displacement of the previously deposited liquid metal weld pool solidifies giving rise to the weld bead (MODENESI; MARQUES; SANTOS, 2012). The study of the weld pool solidification will be described in a simplified way without, however, evaluating more fundamental aspects of this important process.

However, in welding processes, the conditions to which the weld pool is subjected are unfavorable to the formation of the coiled region and of equiaxial grains and the weld structure tends to be formed, in general, only by the columnar grains region (MODENESI; MARQUES; SANTOS, 2012).

In many ways, the weld pool can be considered as a small-scale ingot. However, weld pool has its own characteristics that result in significant differences in terms of the solidification structure and, consequently, of properties, as summarized below (MODENESI; MARQUES; SANTOS, 2012):

- In welding, a large number of solid cores are not formed as occurs in the chilled region of a cast workpiece. In the weld pool, the liquid metal perfectly wets the grains of the base metal that form the wall of the pool and they are heated to temperatures very close to their melting point, not providing the formation of a chilled zone.
- The solidification speed in welding processes can be some orders of magnitude higher than those usually found in castings. When using a high travel speed, solidification

speeds of up to 10^3 mm/s can be achieved. In welding, the cooling speed can also be much higher than in conventional casting.

- The thermal gradients observed in the weld pool are also very high and can reach 10^2 ºC / mm or more. These high thermal gradients and the small volume of the pool make it difficult, in most welding processes, to form the equiaxial region.
- The geometry of the solid-liquid interface varies gradually over time in casting processes. However, in mechanized welding processes and without weaving (similar to continuous casting), this interface remains basically the same.

Solidification begins at the line that passes between the points of the maximum width (points A and B, figure 5.15) and maximum depth of the melt pool. Savage, Lundin and Aronson (1965) carried out a study on the beginning of solidification in the melt pool and the influence of the grain size of the base metal adjacent to the molten zone (FZ) and its crystalline orientation on the weld solidification structure. It was observed that the grains in the FZ are formed as an extension of the grains of the base metal, not needing the nucleation of new grains and called this process of epitaxial growth (SAVAGE; LUNDIN; ARONSON, 1965).

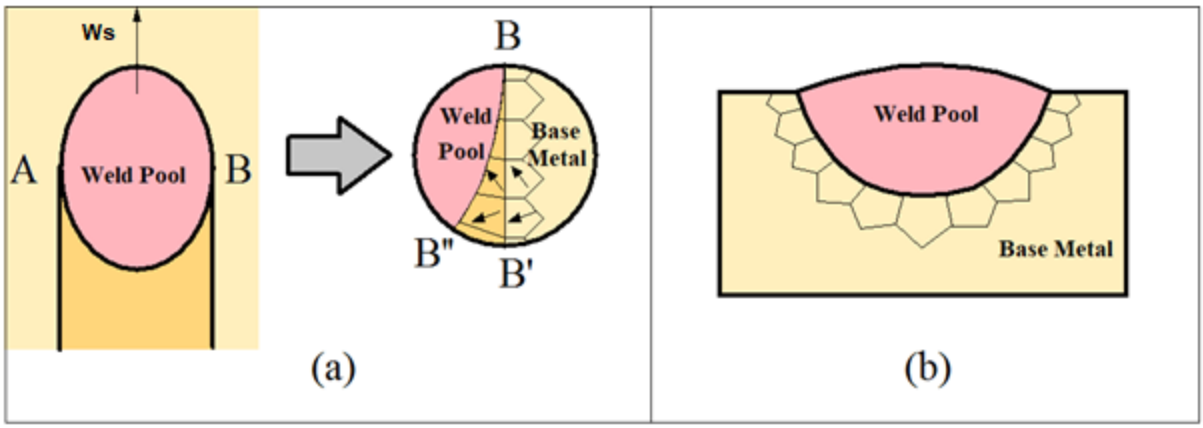

Figure 3.37 - Start of solidification of the melting pool: (a) seen from above, (b) cross section in AB where w_s is travel speed, BB 'is the melting line and BB' '- is the solidification front. The arrows inside the grains in (a) schematically indicate their crystalline orientations. Adapted from Modenesi, Marques and Santos (2012).

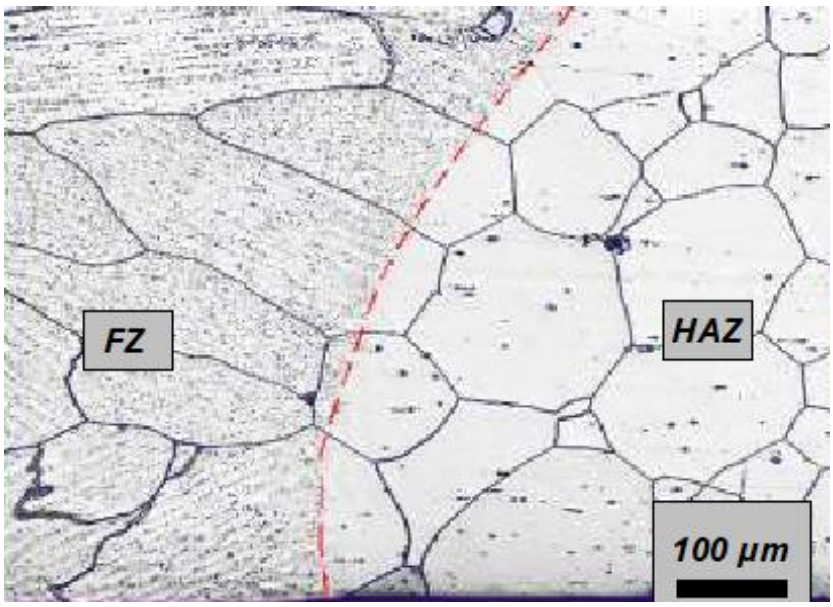

Figure 3.38 - Epitaxial growth of grains from an autogenous weld on a ferritic stainless steel. The dotted line marks the border between HAZ and FZ Adapted from Modenesi, Marques and Santos (2012).

This mechanism of epitaxial growth occurs due to the conditions presented by the weld pool as:

- high thermal gradients;
- heating the metal in solid state in contact with the weld pool to temperatures close to the melting point;
- direct contact between liquid and solid metals with similar chemical compositions and;
- after solidification, contact between two areas of metals with the same crystalline structure.

The nucleation of new grains in the liquid metal is hampered by the conditions set out above. In addition, the conditions mentioned above provide direct growth of the solid in the liquid from the grains of HAZ in contact with the liquid with minimal supercooling (about 1ºC). Therefore, the FZ grains have a similar width and the same crystalline orientation as the base metal grains of which they are extensions. Considering that the grain size at HAZ depends on the metallurgical characteristics of the base metal and the imposed thermal cycle, it can be concluded that the primary grain size at the FZ also depends on the welding parameters that affect the thermal cycle, particularly, the energy of welding (MODENESI; MARQUES; SANTOS, 2012).

When the chemical composition of the weld is substantially different from that of the base metal and, mainly, the crystalline structures of the base metal and the resulting FZ during its solidification are different, the epitaxial growth can be inhibited and solidification, in this

case, can start by nucleating new grains. An example of this is when welding dissimilar metals or when the composition of the filler metal is quite different from the base metal (MODENESI; MARQUES; SANTOS, 2012).

As in casting processes, the weld pool solidification occurs with local changes in chemical composition (segregation). The most common forms of material segregation are: intercellular and interdendritic segregation, segregation in grain boundaries, central segregation, segregation in the weld bead crater and cross-sectioning. This last form of segregation is very characteristic of welding, being observed in both manual and automatic processes, with or without filler metal. The transverse banding is characterized by the existence of successive regions along the bead, enriched and depleted in solute and seems to be associated with periodic undulations on the weld surface, observed even when automatic processes are used. This form of segregation is associated with an intermittent displacement of the solidification front due to the need for periodic evolution of latent heat, periodic variations in the energy source and pulsations in the melt pool (MODENESI; MARQUES; SANTOS, 2012).

So far it has been assumed that the solidification of the melt pool starts exactly on one surface (melting line). However, several materials used in welding solidify over a considerable range of temperatures. In addition, the composition of the filler metal may differ significantly from that of the base metal. In such cases, the FZ may have the following regions (MODENESI; MARQUES; SANTOS, 2012):

- Mixed region: the largest portion of the weld bead and has a composition resulting from the complete mixing of the base metal and the filler metal in the melt pool.
- Unmixed region: corresponds to a region of small thickness (50 to 150 μm) subsequent to the melting line, where the molten base material has not mixed with the filler metal. This region can generate defects in some materials, such as microcracks in tempered and tempered steels of high strength.
- Partially Fused Region: this region corresponds to the transition HAZ/FZ and is characterized by a partial fusion during welding, and can be a potential source of microcracks. In this region, the material experiences peak temperatures between the limits of the liquid and solid curves of the base metal.

3.2.3. Macrostructure and microstructure of welded joints

As shown, the properties of the materials are significantly changed according to the temperature and with small changes in the content of some alloying elements present. In most

welding processes, for example, the materials to be joined require heating to an appropriate temperature. In welding by fusion particularly, it is common to use heat sources (the electric-arc or a flame, for example) of high temperature (1,000 to 20,000°C), acting on small surfaces (a few square millimeters) and, therefore, of high intensity (see table 3.3), which, when moved along the joint, result in the chemical union of the parts due to the formation of the weld by melting and solidification (MODENESI; MARQUES; SANTOS, 2012).

Table 3.3 - Typical values for intensity of welding power sources. Adapted from Modenesi, Marques and Santos (2012).

Welding Process	Welding Source Intensity (GW/m²)
SMAW	from 0.005 to 0.5
GMAW	from 0.005 to 0.5
PAW	from 0.005 to 50
EBW / LBW	from 50 to 5000

The welding power intensity (P_W) of an energy source can be defined by (Eq. 3.7).

$$P_W = \frac{\eta q}{t A_0} \qquad \text{(Eq. 3.7)}$$

where q is the amount of energy generated by the source, η is the thermal efficiency of the source (the fraction of the generated energy that is transferred to the part) and t is the time (MODENESI; MARQUES; SANTOS, 2012). In the case of electrical sources, such as the arc, the energy generated per unit of time is given by the product of voltage U and current I. Thus, for these processes, the specific power is given by (Eq. 3.8).

$$P_W = \frac{\eta (UI)}{A_0} \qquad \text{(Eq. 3.8)}$$

To be used in fusion welding, a source must have a specific power between about 10^6 and 10^{13} W/m². In this relationship, 10^6 W/m² has low penetration and large affected area and 10^{13} W/m² large penetration and small area A_0 (MODENESI; MARQUES; SANTOS, 2012).

This transfer of heat from the source to the workpiece generates temperature changes in the weld and in the adjacent regions of the base metal, which depend on how the heat is diffused to the rest of the material being welded.

Such temperature variations cause, besides the melting and solidification of the weld bead, dimensional variations and localized microstructural changes that can induce residual stresses, dimensional distortions, deterioration of mechanical properties (hardness, toughness,

mechanical resistance, etc.), the appearance of cracks and changes in physical/chemical properties (MODENESI; MARQUES; SANTOS, 2012).

The difficulty of measuring the intensity of energy supplied by a welding source makes it more convenient to use the parameter welding energy (H_T). H_T (see (Eq. 3.9)) is the measure of the energy generated by the source per unit length of the weld joint.

$$H_T = \frac{q}{L} = \frac{q/t}{L/t} = \frac{P}{w_s} \qquad \text{(Eq. 3.9)}$$

where L is the length of the joint, P is the power (energy/time) generated and w_s is the travel speed. H_T is, in general, expressed in kJ/mm or kJ/cm. In arc welding, in conditions where the I and U values are relatively constant, H_T can be calculated according to (Eq. 3.10).

$$H_T = \frac{UI}{w_s} \qquad \text{(Eq. 3.10)}$$

When analyzing the welding energy, it is important to consider that only part of it is transferred to the workpiece. In this case, the imposed energy of welding (H_L) or heat input according to (Eq. 3.11) is used as a parameter.

$$H_L = \eta H_T \qquad \text{(Eq. 3.11)}$$

Heat input is an important parameter to assess welding conditions. However, in the case of electric-arc welding, I, U and w_s have a different influence on the arc behavior. In this way, with the same process and identical welding energy, it is possible to obtain welds of completely different shapes by varying the welding parameters individually (MODENESI; MARQUES; SANTOS, 2012).

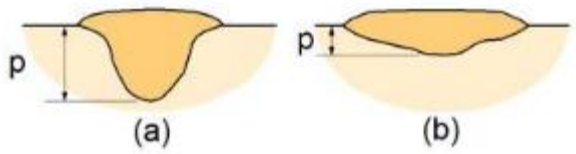

Figure 3.39- Effect of changes in welding parameters on the geometry of weld beads deposited with a welding energy of approximately 1.8 kJ/mm (schematic) (3..3). Welding conditions: (a) 800 A, 26 V and 12 mm/s and (b) 125 A, 26 V and 1.7 mm/s (MODENESI; MARQUES; SANTOS, 2012).

The fusion efficiency (η_f) of the process is also analyzed several times (ratio between the minimum theoretical energy required to obtain the weld bead through the melting of the material and the energy effectively spent in the process):

$$\eta_f = \frac{m_w[(H_{T[fusion]} - H_{T[initial]}) + \Delta H_f]}{q} \qquad \text{(Eq. 3.12)}$$

where m_w (kg) is the mass of the molten metal to form the weld bead, the portion ($H_{T[fusion]}$ - $H_{T[initial]}$) is the amount of energy (J/kg) needed to heat the bead material from its initial temperature to its melting temperature and ΔH_f (J/kg) is its fusion latent heat. In electric-arc welding, the fusion efficiency typically varies between about 5 and 50%. Melting efficiency increases when the values of q and the travel speed are increased simultaneously (MODENESI; MARQUES; SANTOS, 2012).

Thermal welding cycle at a given point is given by the temperature variation during welding and cooling. Each point is subjected to a particular thermal cycle that depends, among other factors, on the location, the peak temperature (T_p), the residence time (t_c) above a critical temperature (T_c) and the cooling speed (Φ).

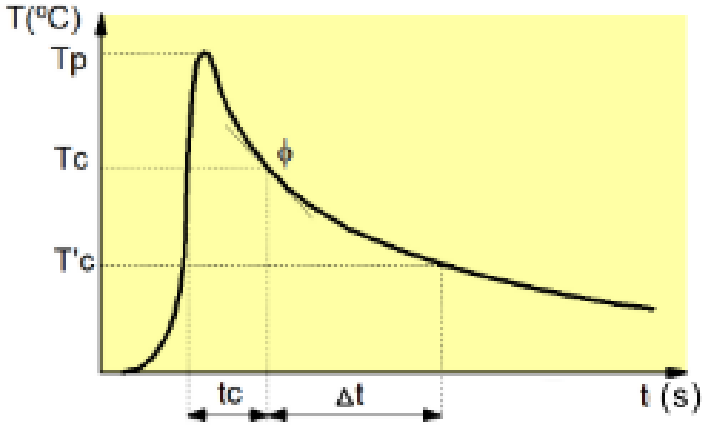

Figure 3.40 - Schematic representation of the thermal cycle in single-pass welding (MODENESI; MARQUES; SANTOS, 2012).

Another parameter that may be is the cooling time relative to a temperature range ($\Delta t_{[Tc/T'c]}$, see Figure 3.40). This range is usually around 800 and 500ºC or 700 and 300ºC ($\Delta t_{8/5}$ or $\Delta t_{7/3}$). dt is inversely proportional to the cooling speed. The cooling time ($\Delta t_{8/5}$) for thick plates (three-dimensional heat flow) can be obtained by the (Eq. 3.13). For thin sheets (three-dimensional heat flow), $\Delta t_{8/5}$ is given by (Eq. 3.14).

$$\Delta t_{8/5} = \frac{H_L}{2\pi k}\left(\frac{1}{500 - T_0} - \frac{1}{800 - T_0}\right) \qquad \text{(Eq. 3.13)}$$

$$\Delta t_{8/5} = \frac{{H_L}^2}{2\pi k \rho c h^2}\left(\frac{1}{(500 - T_0)^2} - \frac{1}{(800 - T_0)^2}\right) \qquad \text{(Eq. 3.14)}$$

where k is the thermal conductivity of the material, T_0 is the initial or preheating temperature, h is the thickness of the workpiece, k, ρ and c are the thermal conductivity, the specific mass of metal and the specific heat of the material.

For carbon steels, these range of temperatures from 800°C to 500°C determines the region where austenite is transformed into perlite and/or bainite. In these circumstances, knowing the time interval can give a direction as to what will be the microstructure formed in a cooling process.

The operational parameters of a welding process can affect the heat flow in the part and, therefore, the associated thermal cycles at various points. Among the main parameters we can mention:

- Thermal conductivity of workpiece

Materials with high thermal conductivity, such as aluminum and copper, dissipate heat better, making localized fusion difficult. Generally, in these cases, preheating is performed or more intense heat sources are used to obtain an adequate fusion.

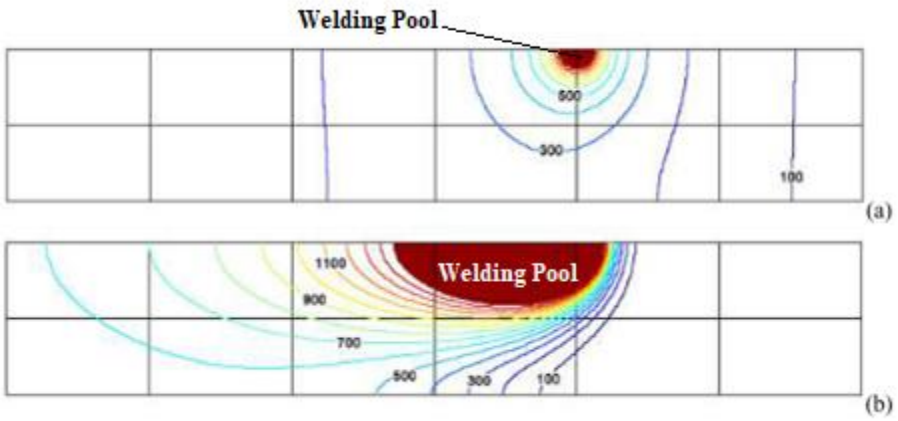

Figure 3.41 - Theoretical temperature distribution around the melting pool for (a) a high thermal conductivity metal (copper) and (b) a low metal (austenitic stainless steel). Thickness: 10 mm. Welding energy: 0.6 kJ / mm (MODENESI; MARQUES; SANTOS, 2012).

- Thickness and geometry of the joint

The thicker the joint, the faster it will tend to cool down during welding due to better conduction heat dissipation. For full penetration welding, where the heat flow is predominantly two-dimensional, the cooling speed in the center of the plate varies with the square of the joint thickness. When the thickness of the joint becomes much greater than the dimensions of the pool, a three-dimensional flow of heat becomes predominant and the cooling speed becomes practically independent of the thickness. The geometry of the joint is also important. For example, the cooling rate will be higher when welding “T” joints than at butt joints, when the process variables, including the thickness of the joint components, are similar.

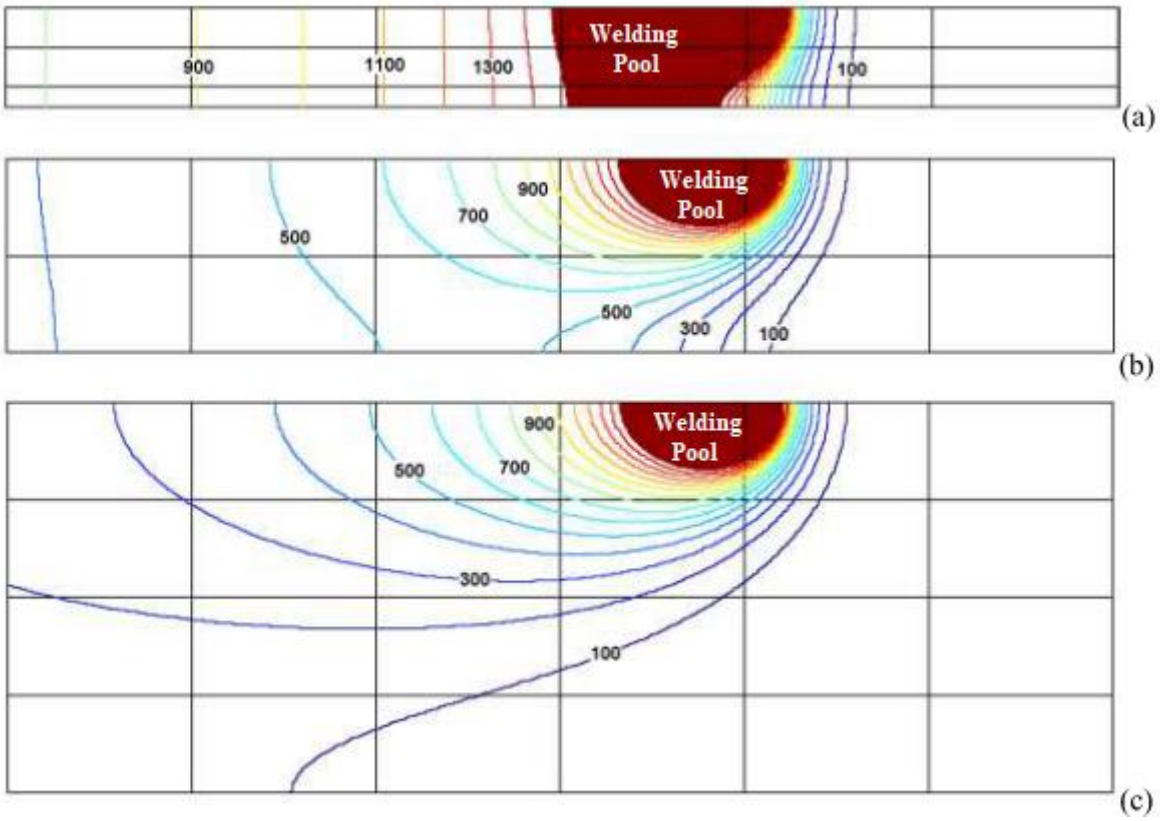

Figure 3.42 - Theoretical temperature distribution around the melting pool for carbon steel plates of (a) 5, (b) 10 and (c) 20 mm thick. Welding energy: 0.6 kJ/mm.(MODENESI; MARQUES; SANTOS, 2012)..

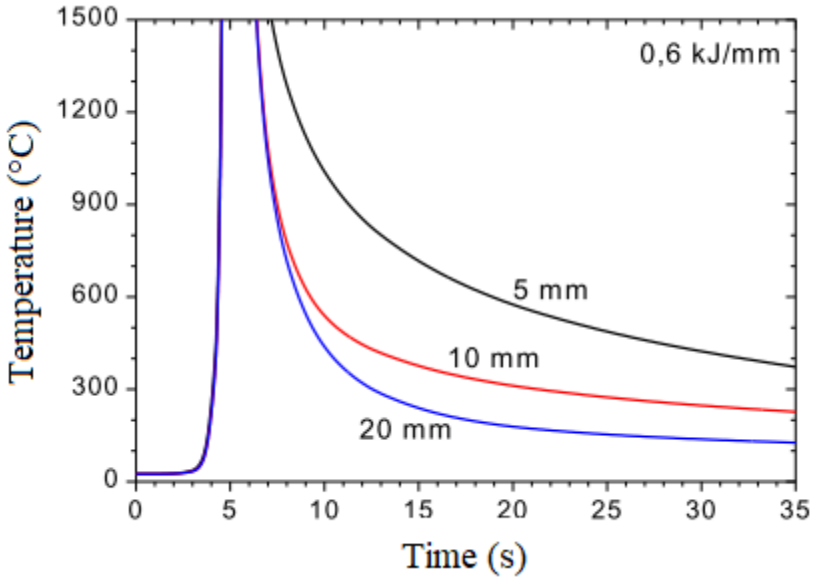

Figure 3.43 - Thermal cycles in the center of the bead for welding sheets of different thicknesses. Welding energy: 0.6 kJ/mm (MODENESI; MARQUES; SANTOS, 2012).

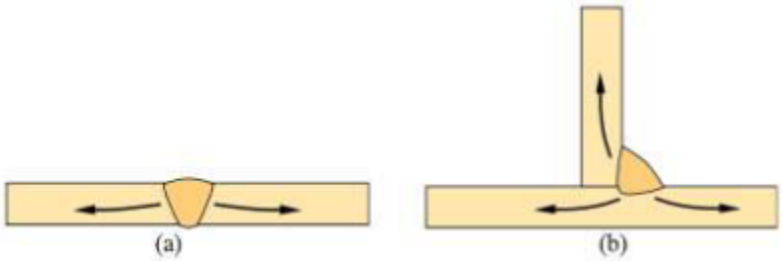

Figure 3.44 - Heat dissipation when welding (a) top and (b) “T” joints (MODENESI; MARQUES; SANTOS, 2012).

- Heat input

The weld cooling rate (Figure 3.45) tends to decrease and the thermal distribution (Figure 3.46) to become more open with an increase in welding energy. However, the limitations of the HL parameter that were discussed earlier must be analyzed.

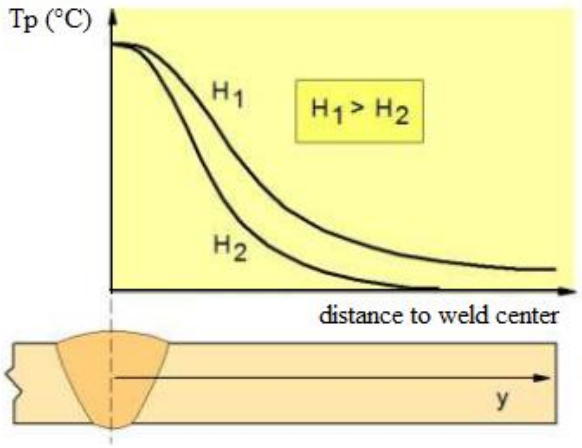

Figure 3.45 - Temperature distribution profile from the center of a weld bead considering two distinct levels of heat input (MODENESI; MARQUES; SANTOS, 2012).

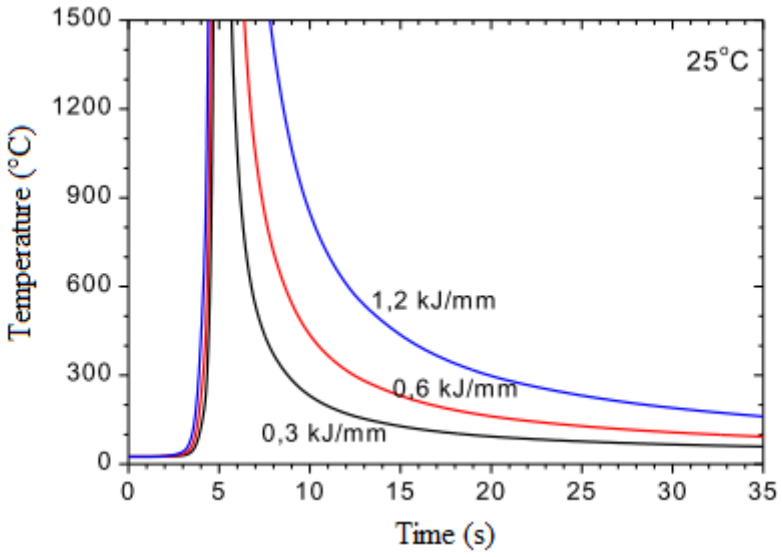

Figure 3.46 - Examples of the influence of the variation of the thermal input in the thermal cycles in the center of the bead for welding with thick plates (MODENESI; MARQUES; SANTOS, 2012).

- Preheating temperature

Measurement of the initial temperature at which the entire part or joint where the welding will be carried out is submitted before the start of the welding operation. As with welding energy, the use of preheating provides reduction in cooling speed (mainly at lower temperatures), as shown in Figure 3.47, and in thermal gradients.

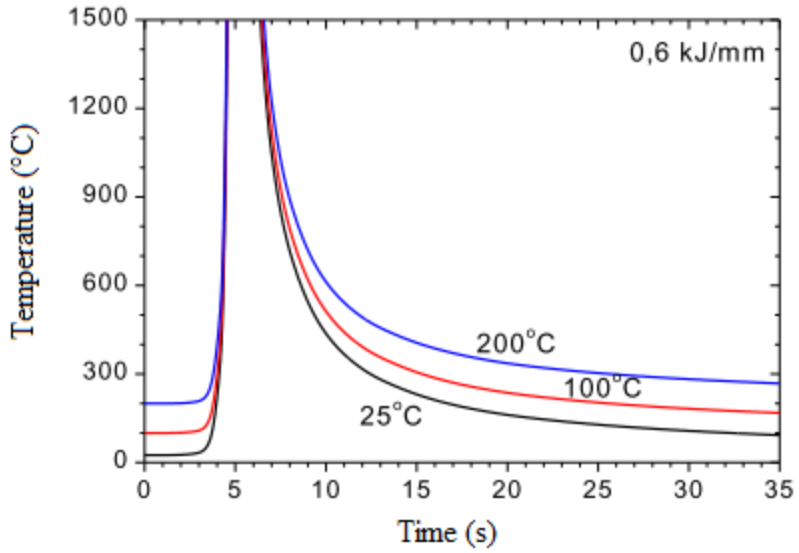

Figure 3.47 - Examples of the influence of pre-heating temperature in thermal cycles in the center of the bead for welding with thick plates (MODENESI; MARQUES; SANTOS, 2012).

In general, heat input and pre-heating temperature are the parameters on which the welding operator has a greater degree of freedom to act. Thus, the correct selection of these allows a certain control over the cooling speed of the weld region and, therefore, over its macrostructural and microstructural properties. In the case of fusion welding processes, we can highlight three important distinct macrostructures: FZ, HAZ and base metal (BM) (MODENESI; MARQUES; SANTOS, 2012).

In the fusion zone, the material was subjected to temperatures above its melting point during welding. In arc welding processes - and more specifically in the GMAW process - this is the case for the added metal (electrode) that is transferred and the base metal fused in the weld pool.

Heat affected zone is the non-fused region of the base metal, but whose microstructure and / or properties have been altered by the thermal welding cycle. Peak temperatures are higher than T_c characteristic of the base metal.

Last and not least, base metal is the furthest regions from the weld that have not been altered by the thermal cycle. Its peak temperatures are below T_c.

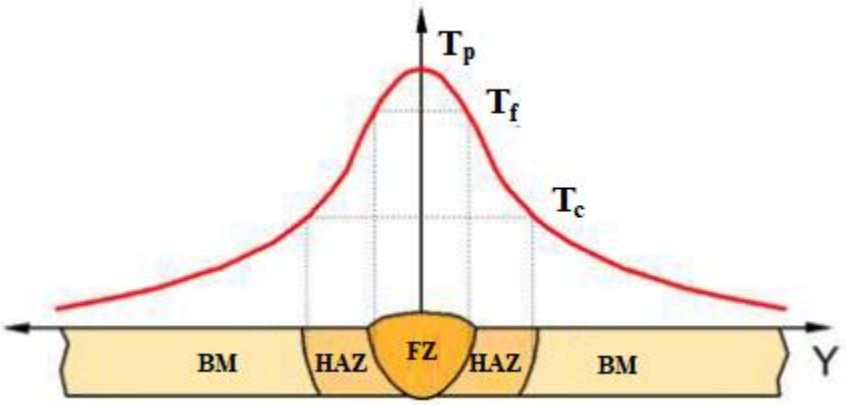

Figure 3.48 - Schematic representation of the macrostructure of the cross section of a welded joint and its relationship with temperature (MODENESI; MARQUES; SANTOS, 2012).

It is important to note that in the event of multi-pass welding, the various points belonging to the welded joint may experience several successive thermal cycles and making the analysis of the macrostructures complex - each new weld bead influences the previously formed FZ and HAZ.

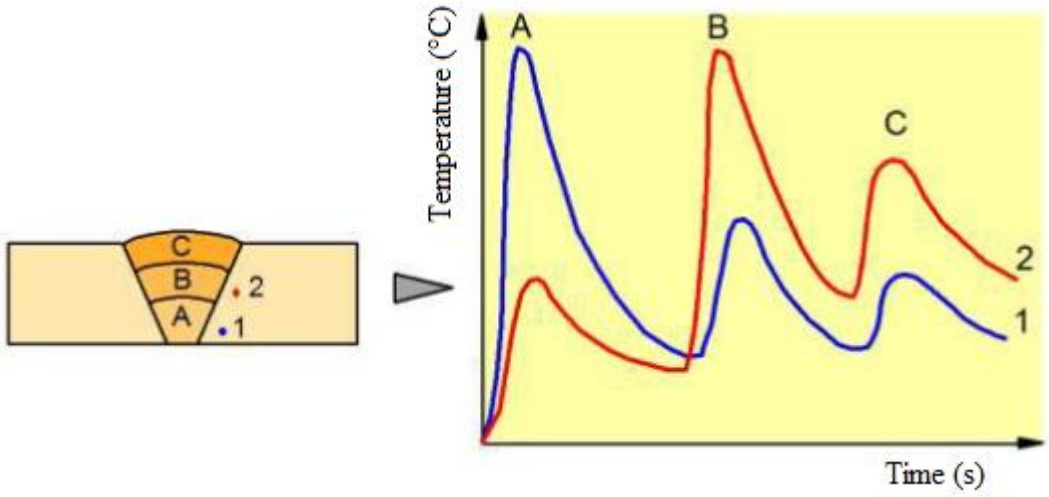

Figure 3.49 - Schematic representation of thermal cycles at two generic points (1 and 2) of the HAZ of a multi-pass weld. A, B and C are the first, second and third passes made, respectively. (MODENESI; MARQUES; SANTOS, 2012).

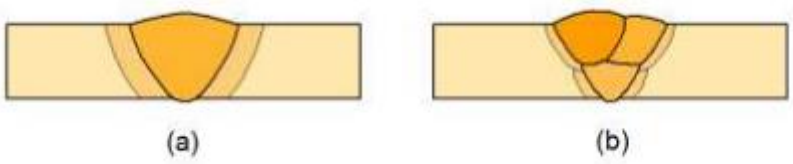

Figure 3.50 - Schematic representation of the structure of FZ and HAZ when welding with one pass (a) and with several passes (b) (MODENESI; MARQUES; SANTOS, 2012).

a) Microstructure of FZ

With a low carbon content and low alloy, the crystalline ferritic structure is the first to form with the solidification of the melt pool. Depending on the composition of the steel, an

expert reaction and the formation of austenite together with ferrite can occur. Continuing with cooling, the remaining delta ferrite will convert to austenite (MODENESI, 2012).

The newly formed austenite, due to high temperatures, undergoes a great grain growth, tending to present a columnar and coarse grain structure, similar to the original FZ microstructure. At temperature levels below 900 ° C, austenite decomposes, resulting in different products or constituents as discussed above (MODENESI, 2012).

The phases and microconstituents present in the microstructure of the molten zone of the weld metal of low carbon and low alloy steels are dependent on many factors. Such microstructure has, for example, macroscopic characteristics resulting from epitaxial and columnar growth and segregation patterns resulting from the solidification of the weld. These aspects, together with the initial state of the austenite (composition, grain size, micro-segregations and deformation state), the content of inclusions and existing precipitates and the heating and cooling conditions to which the welded joint will be exposed will influence the microstructure of the cooled weld bead (MODENESI, 2012).

In single-pass welding processes, the FZ microstructure will be formed from the products of the decomposition of austenite into ferrite, carbides and martensite during cooling, and the ferrite can assume different morphologies. As discussed earlier, several of these microconstituents are difficult to distinguish. In multipass welds, the structure will be even more complex, being formed by regions reheated and altered by the thermal cycles of the following passes and by regions that remained basically unchanged (see Figure 3.49). The characteristics of this microstructure, both on a microscopic scale and on a sub-microscopic scale, are fundamental in determining the final properties of FZ (MODENESI, 2012).

Furthermore, the FZ microstructure of C-Mn steel generally has a high number of non-metallic inclusions. Most non-metallic inclusions are basically formed by a mixture of oxides of Mn, Si and other more powerful deoxidizers (Al and Ti), when they are present. These inclusions are often heterogeneous, with regions on their surface containing Cu and Mn sulfides (MODENESI, 2012).

Another important detail is that the amount of inclusions formed per unit of weld volume is very high, approximately 10^8 mm^{-3}, its shape is generally spherical and its diameters vary between about 0.2 and 1 μm. Inclusions can act as sites for the nucleation of acicular ferrite, their action being more effective with the presence of Ti and Al (MODENESI, 2012).

The reason for the greater efficiency of inclusions with a certain chemical composition to facilitate the nucleation of ferrite is not yet well known. A possible explanation is linked to

the epitaxial growth of ferrite in inclusion regions composed of galaxite (MnO.Al2O3) or TiO2 in which there are crystalline planes that fit well with ferrite planes and, thus, facilitate their nucleation (MODENESI, 2012).

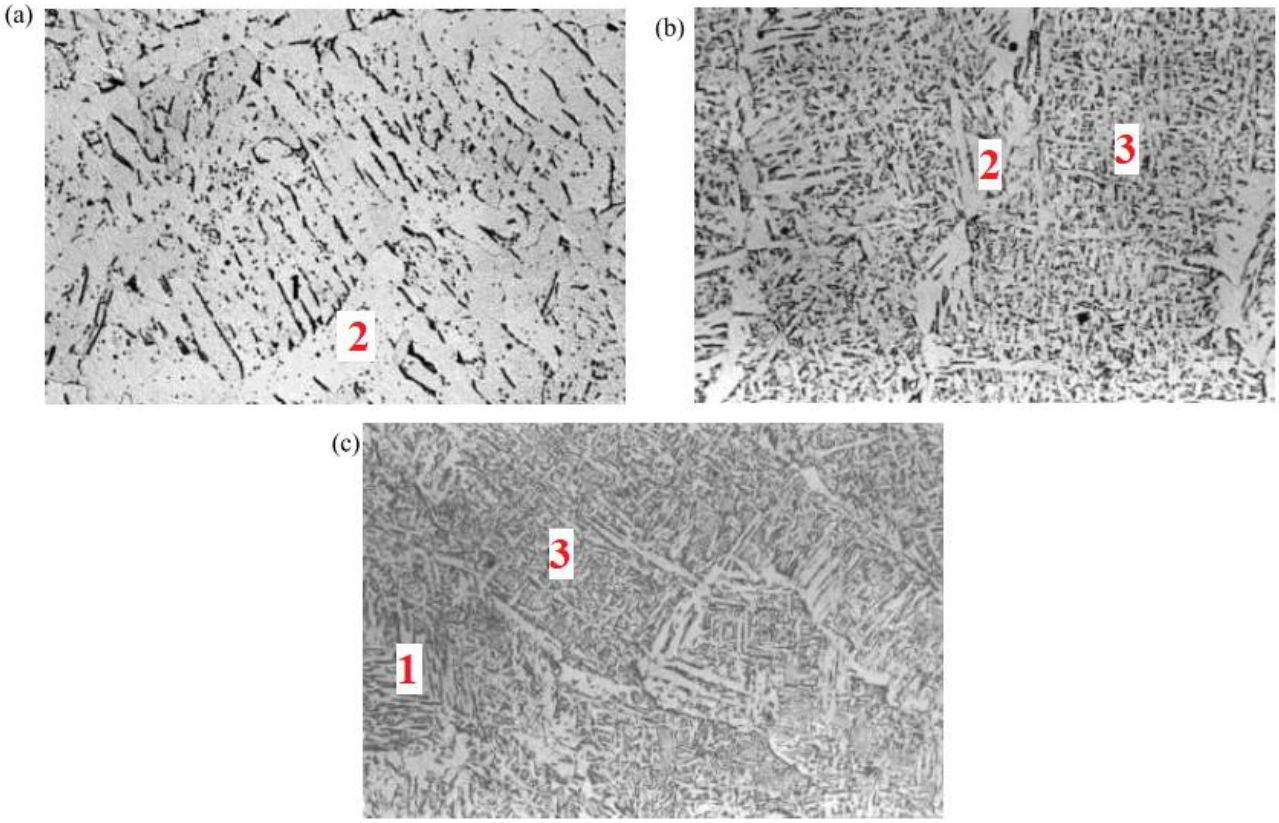

Figure 3.51 - Microstructure of the ZF obtained in SAW welding with different levels of Mn. (a) 0.86% Mn, (b) 1.50% Mn and (c) 2.17% Mn. (1) ferrite with second phase aligned. (2) primary grain boundary ferrite and (3) acicular ferrite. Attack: 2% Nital. Increase: 500X. Adapted from (MODENESI, 2012).

b) Microstructure of HAZ

The microstructure of the thermally affected zone comes from the structural transformations of the base metal associated with thermal cycles and deformations during the welding process. To simplify HAZ studies on transformable steels, this region can be divided into four sub-regions as the observation point moves away from the weld bead (MODENESI, 2012):

- Coarse-grained HAZ (CGHAZ);
- Fine-grained HAZ (FGHAZ);
- Intercritical HAZ (IHAZ) and;
- Subcritical HAZ (SHAZ).

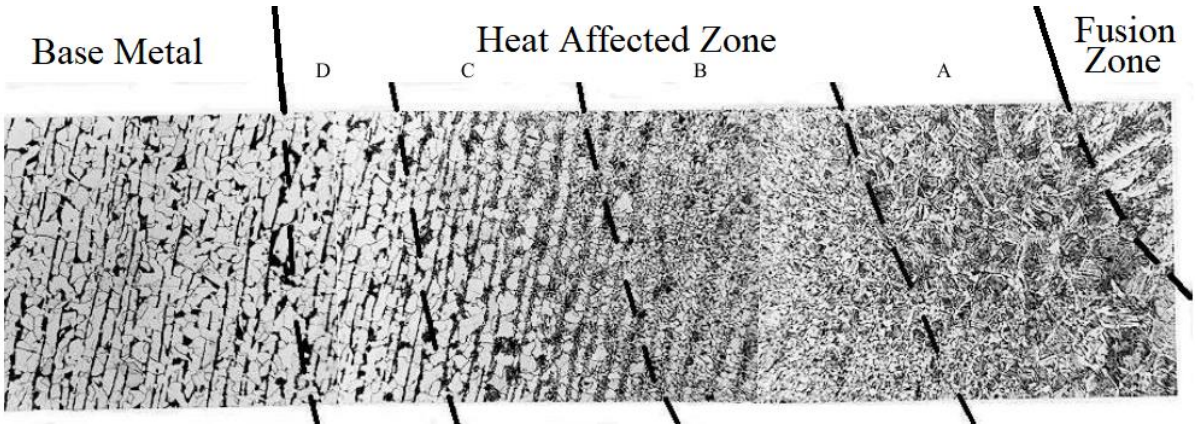

Figure 3.52 - HAZ structure of a low carbon steel. The approximate divisions correspond to: A - Coarse Grained Region, B – Fine Grained Region, C - Intercritical Region and D - Subcritical Region. Etching: nital + picral. Original magnification: 100X. Adapted from (MODENESI, 2012).

i) Coarse-grained Heat Affected Zone (CGHAZ)

The coarse-grained region - also known as the grain growth region - corresponds to the exposed base metal region at temperatures above the austenitic grain growth temperature (usually close to 1200ºC). This region presents high austenitic grain size and final microstructure resulting from the decomposition of austenite(MODENESI, 2012).

Austenitic grain size is influenced mainly by two factors:

- thermal welding cycle, particularly its peak temperature and its residence time above the grain growth temperature, and;
- austenitic grain growth temperature of the material.

Considering a given material and joint geometry, the associated thermal cycles are directly associated with the welding energy. The higher the value of the thermal input, the coarser the grains in this region will be and the greater its extension (MODENESI, 2012).

The effect of grain growth in this region, using a given set of welding parameters, can be reduced by using steels with a higher grain growth temperature. This occurs in steels treated with aluminum, since the presence of precipitates of aluminum nitride leads to the obtaining of a material with more refined grains and prevents the growth of grain up to temperatures in the order of 1250ºC (MODENESI, 2012).

Above this temperature, however, most precipitates are in solution and grain growth becomes rapid, so that, in the melting line, the grain size is not much different from that of untreated steels. Additions of niobium, vanadium or titanium can also reduce grain growth at HAZ, particularly in low-energy welding (MODENESI, 2012).

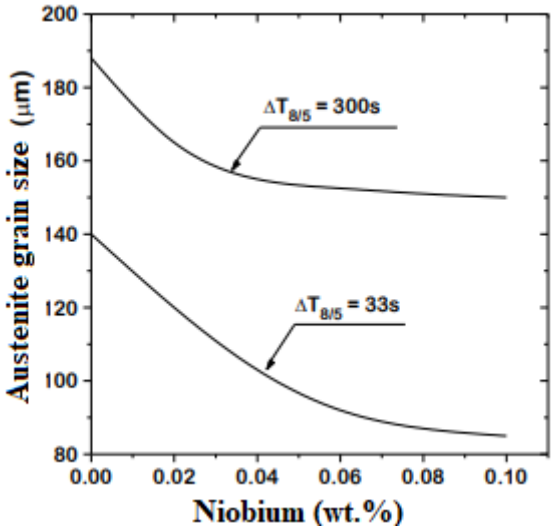

Figure 3.53 - Influence of the niobium content on the austenitic grain size of the HAZ. Adapted from (MODENESI, 2012).

The Welding Institute (TWI) has proposed a terminology for CGHAZ constituents which can be compared with terms commonly used by researchers.

Table 3.4 – Comparison between terminology proposed by TWI and terms used by other researchers. Adapted from (MODENESI, 2012).

TWI	Phase transformation Researchers
Martensite	Martensite
	Lower Bainite
Ferrite with and without MAC (Martensite-Austenite-Carbide)	Widmanstätten Ferrite
	Granular structure
	Bainite
Intragranular Widmanstätten Ferrite	Acicular Ferrite
Pro-euctetoid Ferrite	Grain boundary Ferrite
	Polygonal Ferrite
Pearlite	Pearlite
Ferrite-Carbide Aggregate	

ii) Fine Grained Heat Affected Zone (FGHAZ)

The fine-grained heat affected zone (FGHAZ) or normalization zone is located further from the melting line than that of coarse grains, being subjected during welding, to peak temperatures between about 1200°C (grain growth temperature) and A3 (start temperature of ferrite formation).

This region is characterized by a fine-grained structure, similar to that of steel standardized. This region is not considered problematic for most steels, except for tempered

and tempered ones, where it may present less mechanical strength than the base metal (MODENESI, 2012).

iii) Intercritical Heat Affected Zone (IHAZ)

IHAZ shows partial transformation of its original structure and is subjected to peak temperatures between A3 and A1. In some cases, particularly in multipass welding, constituents of high hardness and low toughness can form in this region (MODENESI; MARQUES; SANTOS, 2012).

iv) Subcritical Heat Affected Zone (SHAZ)

This zone corresponds to the base metal heated to temperatures below A1. When welding heat-treated steels, this region can undergo over-tempering and a loss of mechanical strength or hardness (concerning to the base metal) (MODENESI; MARQUES; SANTOS, 2012).

4. MATERIALS AND METHODS

The methodology adopted in this work is based on the deposition of weld beads from an AWS ER70S-6 wire on SAE-AISI 1020 steel plates using the GMAW process. Welding parameters and thermographic information during bead deposition are stored using an open-loop control data acquisition system. Subsequently, the samples are metallurgically characterized (scanning electron microscopy and X-Ray diffraction analysis) and the extensions of the thermally affected zones are collected every 5 mm from the longitudinal axis of each weld bead by optical microscopy and scanning electron microscopy analysis. Finally, the weld beads had their microstructural features evaluated and associated with the welding parameters used in their production. Also, estimation models were developed to predict microstructural parameters in the FZ and the HAZ as functions of the welding parameters.

4.1. EQUIPMENT USED

In this work, an experimental system was used to collect the values of the selected variables and to control the GMAW process, allowing an open loop control and data storage in a personal computer. The methods and tools used to data processing and estimate the extension of fusion zone and sub-regions of heat affected zone of the weld bead are discussed in this chapter.

The variables evaluated are: welding voltage, welding current, infrared thermography and welding torch (or work piece) position. The system controls of the travel speed and sends several set points to the welding power source such as the set point of welding voltage and the set point of the wire feed speed. Despite this, the control used was in open loop due the system does not use the measurements to change the welding parameters and follows a sequence defined by the user.

An open-loop control and data acquisition system was used to acquire welding and thermographic parameters and for control the start and the end of welding operation. It was composed of five parts: a welding power source, a robotic welding table, data acquisition and control interfaces, a thermographic camera and a computer with data acquisition and image processing software (BESTARD; ALFARO, 2017).

The welding power source used was the Inversal 450 (IMC-SOLDAGEM, 2005). An algorithm based on RS232 protocol developed by Bestard, Sampaio and Alfaro (2018) was used

to establish communication required for remote control and data acquisition. The same authors developed a state machine and a data acquisition software in Visual Studio to monitor and control the status of welding power source and the operation sequence of welding process.

The robotic welding table used was developed by GRACO students (FRANCO, 2008) and it is responsible for fixing components such as the welding torch, thermographic camera and profilometry system, and to promoting the displacement of the workpiece. It consists in a linear axis which presents step of 5 mm/revolution equipped with a stepper motor which provides 1,8 degrees/step. A driver circuit controls the motor by pulses of signals that modify its speed (stepper time) and direction. Furthermore, other signals indicate the status of the driver and act as protection against overload. The maximum load supported by the structure is about 147 N and the maximum travel speed is 15 mm/s (FRANCO, 2008).

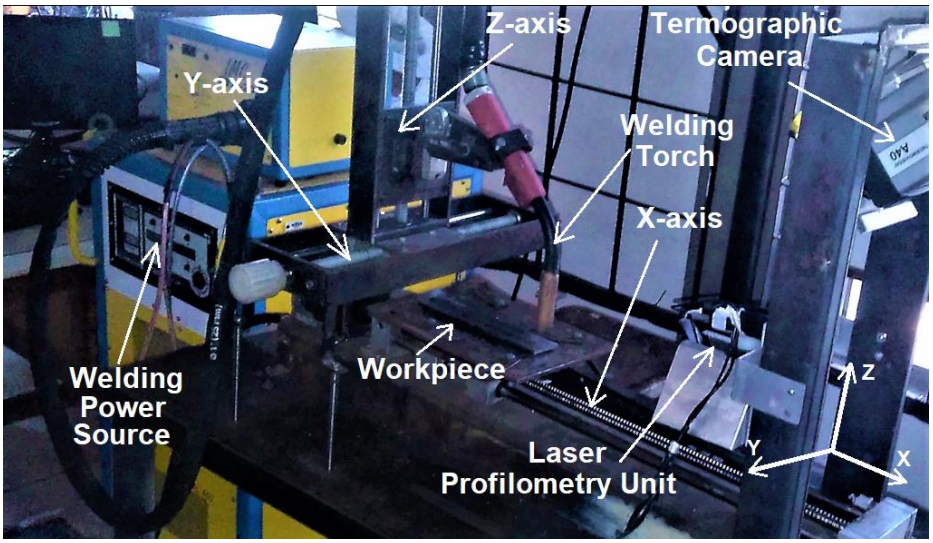

Figure 4.1 - Robotic welding table with welding torch and thermographic camera (BESTARD; SAMPAIO; ALFARO, 2018).

In this way, data acquisition and control interface synchronize the welding sequence and the operation of the power source with the displacement of the workpiece, to obtain real-time measurements of the welding parameters. The welding source is connected to interface by a RS232 port. Moreover, the interface is connected to stepper motor's driver circuit and to a computer by digital signals and USB port, respectively.

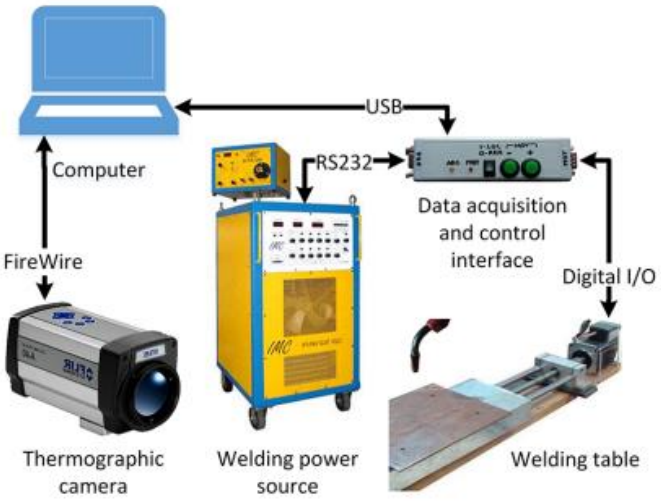

Figure 4.2 - Schematic overview of components and connections of data acquisition and open loop control system(BESTARD; SAMPAIO; ALFARO, 2018).

It was used also a FLIR Thermo Vision A40M camera (FLIR-SYSTEMS, 2004) to obtain thermographic information about weld pool. Through a Firewire interface, the temperature of each pixel is collected in a matrix format. This model of thermographic camera uses a semiconductor sensor of focal plane array uncooled microbolometer technology and has temperature range between -40°C and 2000°C. The sampling time used was 30 ms.

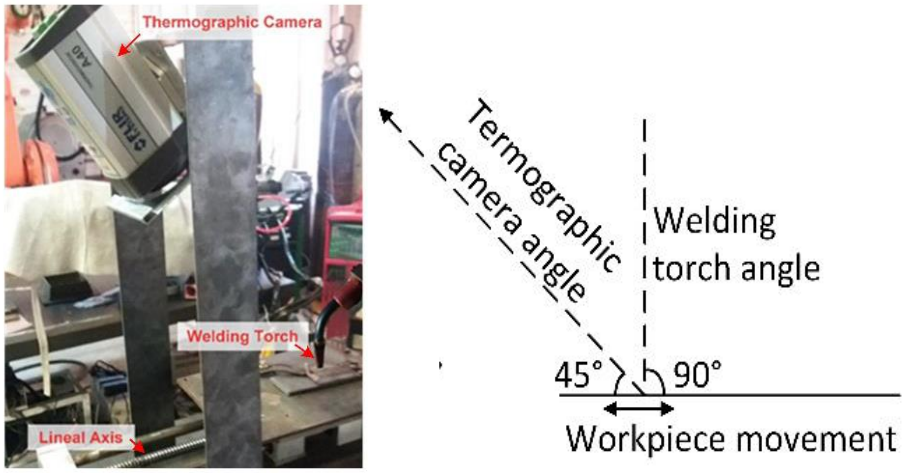

The emissivity of the weld pool and surroundings assumes different values when the temperature is varied, especially when the alloy solidifies. Therefore, temperature measurements of the weld pool using a thermographic camera should be considered approximate. Furthermore, accurate measurements of absolute temperature values are not part of the objectives of this work. We chose to analyze absolute values regarding the emission of infrared radiation by the weld pool and not the calculated temperature values based on the emissivity coefficient.

The camera was mounted at an angle of 45 degrees to enable the emission profile of infrared radiation in the xy plane. Nevertheless, there is a portion of radiation which is emitted by the plasma column of the arc and which is reflected by the workpiece surface.

The data acquisition software called as Thermo Data Welding (TDW) was developed in Visual Studio by Bestard, Sampaio and Alfaro (2018). This software allows to set thermographic camera configurations, adjustment of fixed welding parameters and of robotic welding table, welding sequence for producing specimens, to configurate USB communication port in the PC used where the data acquisition interface is connected and choose the datafile storage location. Three files are created when the welding sequence ends: a system configuration file, a stimulus sequence file and a datafile with measurements collected.

4.2. WELDING PROCEDURE

The selected material for the production of the weld beads was the AWS ER70S-6 wire with a diameter of 1 mm and SAE 1020 steel plates with 6 mm of thickness as the base metal. The composition of alloys used are shown in Table 4.1.

Table 4.1 - Compositions of alloys used.

Alloy	Chemical Composition Limits (%)				
	C	Mn	P (Max)	S (Max)	Si
OK Autrod 12.51 ER70S-6	0,08	1,50	-	-	0,90
SAE 1020	0,18 to 0,23	0,30 to 0,60	0,30	0,50	-

Three samples are produced using shielding gas composed by 96% Ar and 4% CO_2. Despite being a material and gas composition not commonly used in industry, this research aims to evaluate the microstructure produced and the applicability of ANN in the microstructural estimation of low carbon and low alloy steels. The contact tip to workpiece distance (CTWD) used was 15 mm. The process input variables were travel speed (w_s), welding voltage (U_w), welding current (I_w) and wire feed speed (w_f).

Table 4.2 shows the welding parameters used in the production of the samples. In each sample produced, a single pass weld bead was deposited varying the travel speed and wire feed speed. In each sample produced, a single pass weld bead was deposited varying the travel speed and wire feed speed.

Table 4.2 - Welding parameters used in the production of samples

Sample 1					Sample 2					Sample 3				
Position (mm)	w_s (mm/s)	U_w (V)	w_f (m/min)	Arc open	Position (mm)	w_s (mm/s)	U_w (V)	w_f (m/min)	Arc open	Position (mm)	w_s (mm/s)	U_w (V)	w_f (m/min)	Arc open
5	6	30	4	1	5	6	30	6	1	5	6	30	6	1
30	12	30	8	1	30	12	30	12	1	30	6	30	12	1
55	6	30	4	1	55	6	30	6	1	55	6	30	6	1
80	10	20	3	0	80	10	20	3	0	80	10	20	3	0

Normally studies for mapping the behavior of a process are carried out using the same conditions for the fixed parameters during welding (wire diameter, composition of the shielding gas, pre- and post-heating temperature of the joint, room temperature and humidity, etc.) However, the variation in welding parameters during the welding process changes the substrate temperature after a certain length of metal deposition, as expected. However, by varying the parameters during deposition, it is possible to study the behavior of the material's microstructure formation during the transient regime and evaluate its impact on modeling.

The welding sequences in positions 80 mm and 120 mm took into account adequate values of w_s and w_f so that the wire exit occurs before the weld pool solidifies. At these positions the arc was closed. The sampling period used to collect the welding parameters was 20 ms. The first 5 mm and the crater region of the samples do not represent the behavior of the process, as shown in Figure 4.3. These regions were not considered in the study. The lengths analyzed ranged from 5 mm to 65 mm, 70 mm and 75 mm for samples 1, 2 and 3, respectively.

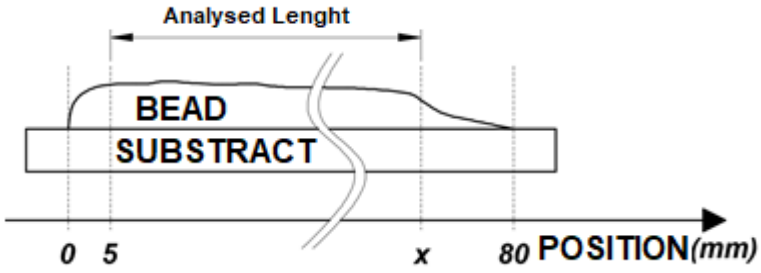

Figure 4.3 - Definition of the total length analyzed in the weld beads.

After deposition the samples were cut in order to avoid heating the metal. In this work it was decided to use the longitudinal section of the weld beads although the most efficient way to analyze the HAZ extension is through the evaluation of the weld bead cross section. However, the longitudinal cut allows to continuously evaluate the microstructure morphology along the weld bead.

The workpiece was positioned on the robotic welding table on a 6.25 mm thick steel plate. Initially, this plate tends to behave as a heat drain for the process, generating a three-dimensional heat transfer process in the substrate, increasing the vertical extension of HAZ. In addition, the width of the substrate plates is 50 mm, making the heat transfer process three-dimensional.

The samples underwent metallographic testing consisting of sanding and subsequent polishing using 1 μm grain size alumina. After polishing, a chemical attack was carried out on the three samples using a 5% Nital solution to identify the ferritic phase and Picral to identify the austenitic phase.

After the preparation, measurements of the extent of the FAZ and HAZ sub-regions were performed on the 3 samples. The analyzes were performed at the Microscopy Laboratory of the University of Brasília using an Olympus LEXT OLS4000 confocal laser microscope equipment. Measurements were taken using the measurement tool of the microscope in FZ and in all sub-regions of HAZ every 5 mm along the longitudinal axis of the samples. Figure 4.4 shows a scheme of microstructure identification and extension measurement using optical microscopy.

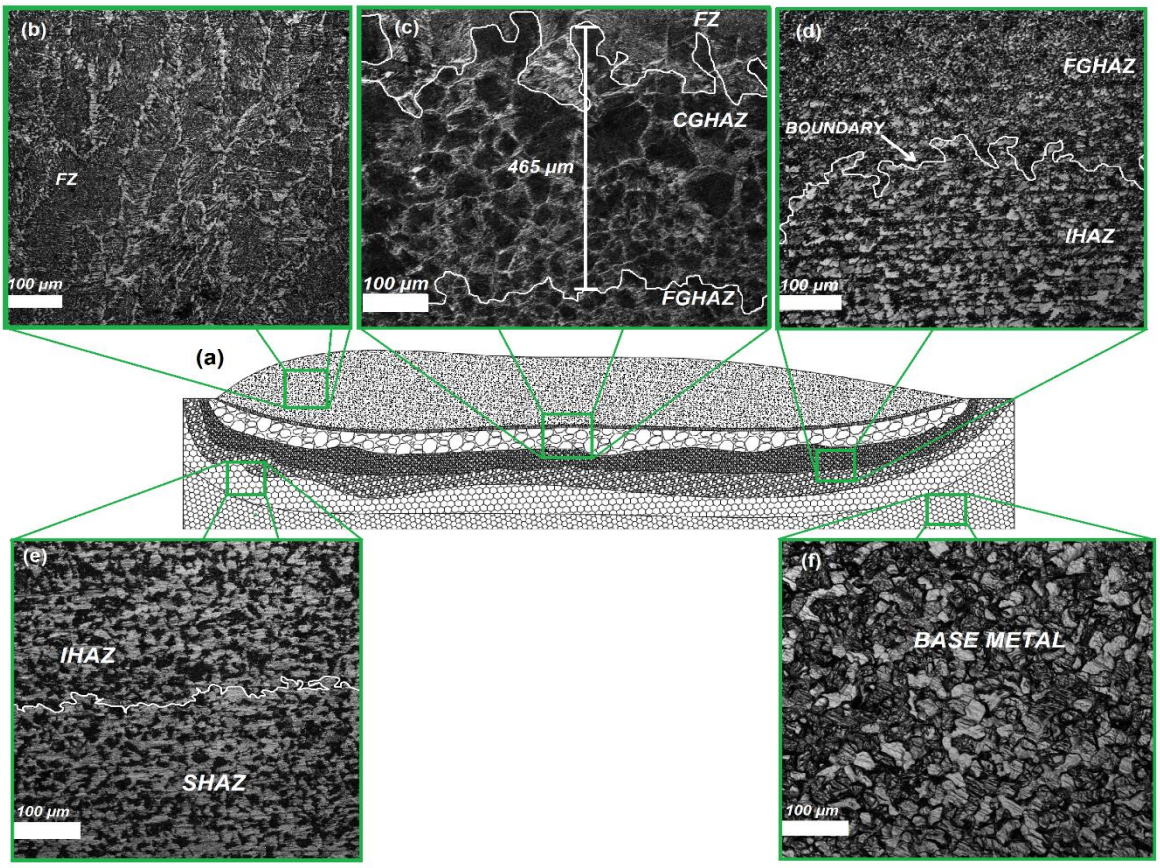

Figure 4.4 - Scheme of zones analyzed. (a) schematic transversal section of weld bead; (b) FZ; (c) FZ, CGHAZ (an its extension measurement methodology) and FGHAZ; (d) FGHAZ/IHAZ boundary; (e) IHAZ/SHAZ boundary; (f) base metal.

Simultaneous to this stage, analysis of extension of the regions and microstructural characterization were performed using Scanning Electron Microscopy (SEM) tests. Using this technique, it was possible to identify more clearly the phases present in the microstructure of each region of the material

In this stage of the study, the Scanning Electron Microscopy (SEM) analyzes were performed at the Microscopy Laboratory of the University of Brasília. The SEM tests were performed on JEOL JSM-7100 equipment. Before these tests, the samples were sanded, polished and etched with 5% Nital.

The X-Ray Diffraction (XRD) analyses was carried out in three different zones in each sample: FZ, CGHAZ and IHAZ. These analyses aimed to evaluate the chemical composition of each region and the phases present in microstructure. XRD were performed using RIGAKU diffractometer, model D/MAX-2A/C, with Cu Kα radiation, operating at 35 kV and 15 mA. The diffraction patterns were carried out in the range of 20 to 100° (2θ), with 0.1° step. The phase identification was performed using Xpert Hiscore software.

4.4. NEURAL NETWORK MODELING

The ANN model adopted to implement the sensor fusion algorithm was the Multilayer Perceptron with Backpropagation algorithm, with 9 inputs. The input variables are U_w, I_w, w_s, w_f, and the 5 thermographic parameters defined before. Several layer configurations using 1 and 2 hidden layers in order to estimate the extensions of analyzed zones.

Furthermore, 5 output variables were defined as extensions of between FZ, CGHAZ, FGHAZ, IHAZ and SHAZ (based on the longitudinal axis of the samples). Six different models were used to estimate the extensions of the modeled regions: development of 5 models with only 1 output (A, B, C, D and E) and a model with all 5 outputs.

Models A to F consist of a microstructure prediction algorithm for FZ, CGHAZ, FGHAZ, IHAZ and SHAZ, respectively, all with the same configurations varying only the output. Model F represents the ANN for forecasting the four zones described above in the same algorithm.

All possible combinations between 12 and 18 neurons were tested in networks with 1 and 2 hidden layers, totaling 56 combinations per model. The quantity and size of the hidden

layers were selected by balancing the computational cost (neuron quantity) and the estimation error, by previously testing different configurations.

Also, each of the models was simulated using two training methods: Levenberg-Marquardt approximation algorithm (LM) and Bayesian Regularization (BR). The number of training cycles was varied between 1 and 5 to refine the results in each network.

The results are then displayed for each group and for all data. The results were evaluated by comparing the performance regarding the mean squared error (MSE) value presented by each network. Table 4.1 presents a summary of the test matrix adopted for tests with ANN algorithms.

Table 4.3 - Test matrix for all ANN models and their network type settings (LM or BR) and number of training runs (ranging from 1 to 5) for 12 neurons in the 1st and 2nd hidden layers.

Neurons in 1st hidden layer	Neurons in 2nd hidden layer	ANN Method	Training Cycles	ANN algorithm model					
				FZ (A)	CGHAZ (B)	FGHAZ (C)	IHAZ (D)	SHAZ (E)	ALL (E)
12 to 18	0 or from 12 to 18	LM	1	A-LM1	B-LM1	C-LM1	D-LM1	E-LM1	F-LM1
			2	A-LM2	B-LM2	C-LM2	D-LM2	E-LM2	F-LM2
			3	A-LM3	B-LM3	C-LM3	D-LM3	E-LM3	F-LM3
			4	A-LM4	B-LM4	C-LM4	D-LM4	E-LM4	F-LM4
			5	A-LM5	B-LM5	C-LM5	D-LM5	E-LM5	F-LM5
		BR	1	A-BR1	B-BR1	C-BR1	D-BR1	E-BR1	F-BR1
			2	A-BR2	B-BR2	C-BR2	D-BR2	E-BR2	F-BR2
			3	A-BR3	B-BR3	C-BR3	D-BR3	E-BR3	F-BR3
			4	A-BR4	B-BR4	C-BR4	D-BR4	E-BR4	F-BR4
			5	A-BR5	B-BR5	C-BR5	D-BR5	E-BR5	F-BR5

The neural network proposed for estimating the extensions of FZ and sub-regions of HAZ in weld bead, was trained and validated using the experimental data. Each experiment data set was divided in 70% to train, 15% to validate and 15% to accuracy test for LM training mode. For BR networks, the data set was divided in 70% to train and 30% to test the accuracy of the models.

5. RESULTS AND DISCUSSION

In this section, the results of the microstructural evaluation and ANN modeling will be presented and discussed taking into account the objectives of this work. In each sample produced, a single pass weld bead was deposited (see Figure 5.1)

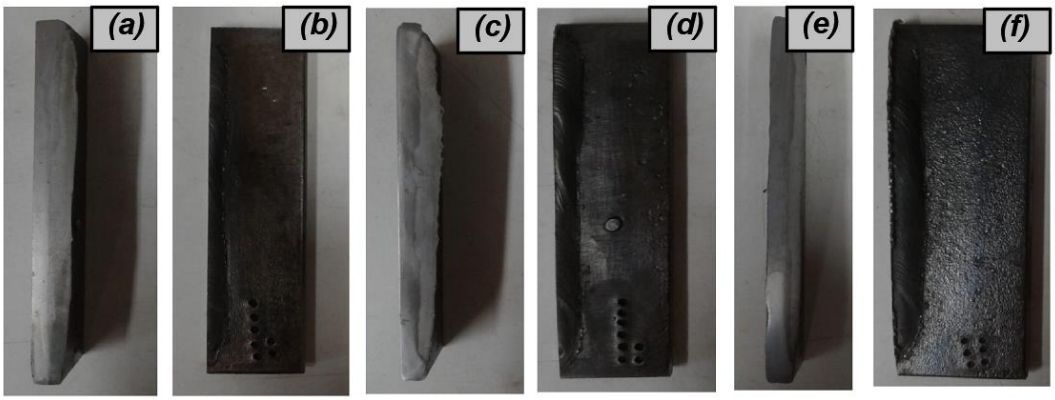

Figure 5.1 - Metallographic preparation in (a) sample 1, (c) sample 2 and (e) sample 3. Top views of samples 1,2 and 3 are shown in(b), (d) and (f), respectively.

5.1. THERMOGRAPHY AND ANALYSIS OF ZONE EXTENSIONS

During the deposition of the samples, information about the thermal field generated was captured. This captured information refers to a thermographic value associated with the intensity of infrared radiation emitted by different parts of the weld bead surface. The profiles of emission of IR radiation were recorded and used to determine the values of intensity, width and emission area. The higher the temperature, the greater the intensity of the signal captured by the lens of the thermal camera.

5.1.1. Thermographic results

Before carrying out this analysis, it is necessary to check the emissivity of the filler metal in the liquid state so that there is no distortion in the behavior of the graphics. Thermographic data (BESTARD et al., 2018) were collected from the three samples along their entire longitudinal axis. These thermographic parameters are: thermographic peak (t_p), thermographic base (t_b), thermographic width (t_w), thermographic area (t_a) and thermographic volume (t_v)

Figure 5.2 shows an example of this information obtained for sample 3 in the 30.0 mm position. The welding parameters set and the actual measurements from the welding source sensors are shown in Table 5.1.

Table 5.1 - Parameters inserted in the welding source and sensor measurements for sample 3 in the 30.0 mm position.

	w_s (mm/s)	U_w (V)	w_f (m/min)
Setpoint	6.0	30.0	12.0
Real	6.0	30.1	10.3

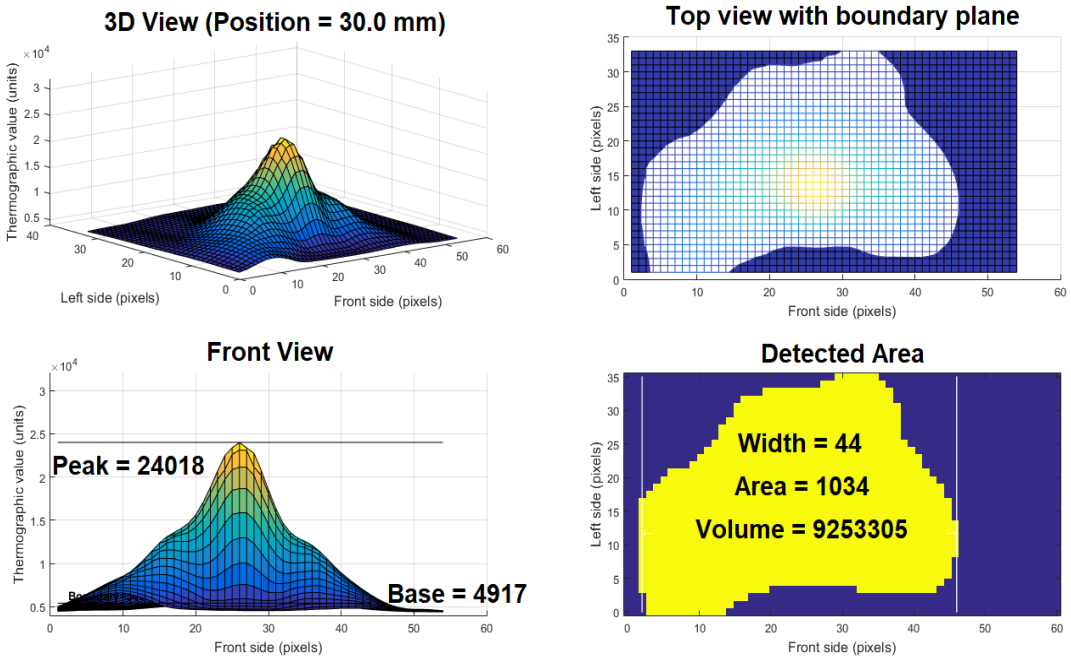

Figure 5.2 - Thermographic parameters for the 30.0 mm position

Table 5.2, Table 5.3 and Table 5.4 present thermographic parameters and welding parameters obtained for the samples.

Table 5.2 - Thermographic parameters and welding parameters obtained for sample 1.

Sample 1										
Position (mm)	Thermographic Data					Welding data acquired				
	T_p (un.)	T_b (un.)	T_w (pixels)	T_a (pixel²)	T_v (u.a.)	w_s (mm/s)	U_w (V)	I_w (A)	w_f (m/min)	Welding Energy (J/mm)
5	16444	4441	33	661	5382119	6,0	29,8	130,8	4,0	650,7
10	17372	4512	39	839	6863613	6,0	29,9	144,9	4,0	722,3
15	13695	4623	43	897	7462487	6,0	29,9	150,2	4,0	749,3
20	16539	4674	42	858	7559899	6,0	30,0	139,2	4,0	695,5
25	15078	4774	47	892	7688202	10,3	30,0	137,0	5,1	399,0
30	23491	4691	43	803	7015321	12,0	29,5	204,1	8,0	502,1
35	21616	4633	42	793	6812866	12,0	30,0	209,1	8,0	522,2
40	18186	4594	41	790	6531906	12,0	30,8	206,1	8,0	528,3
45	16467	4568	37	773	6116508	12,0	30,0	202,6	8,0	507,0
50	22683	4529	34	740	6214925	7,7	29,9	204,9	5,1	796,5
55	15419	4563	40	935	7888818	6,0	29,9	133,3	4,0	664,9
60	15317	4605	43	964	7925552	6,0	30,0	137,0	4,0	684,9
65	18944	4447	34	677	5855322	6,0	30,0	134,0	4,0	667,4

In the three samples there were no significant changes in the values of Ta, Tb, Tw and Tv with changes in welding parameters during metal deposition. In sample 1, increasing w_s and w_f values occurs a reduction in thermal input, as shown in Table 5.2. Analyzing the thermographic data, it is noticed a reduction in the value of T_a with the variation of the parameters in this region. The reduction in the value of T_a can be explained by the increase in travel speed, which reduces the dimensions of the weld pool.

Table 5.3 shows the data obtained for sample 2. The data set presented follows the same trend as those shown in sample 1. In other words, increasing the travel speed, causes a reduction in T_a value.

Table 5.3 - Thermographic parameters and welding parameters obtained for sample 2.

Sample 2										
Position (mm)	Thermographic Data					Welding data acquired				
	T_p (un.)	T_b (un.)	T_w (pixels)	T_a (pixel²)	T_v (u.a.)	w_s (mm/s)	U_w (V)	I_w (A)	w_f (m/min)	Welding Energy (J/mm)
5	15207	4406	28	468	3587370	6,0	28,7	173,7	6,0	831,3
10	22608	4477	39	811	6876864	6,0	29,8	176,6	6,0	876,9
15	13837	4561	42	868	6594372	6,0	29,9	185,6	6,0	925,9
20	13380	4670	43	879	6968771	6,0	30,0	183,6	6,0	916,8
25	14848	4764	44	855	6831362	6,0	30,0	172,2	6,0	862,1
30	17450	4667	42	771	5971642	12,0	29,8	235,1	12,0	583,2
35	16755	4627	42	679	5214867	12,0	30,0	250,3	12,0	624,8
40	18031	4566	40	599	4471517	12,0	29,9	249,7	12,0	621,5
45	18353	4568	33	560	4453864	12,0	29,9	252,2	12,0	628,9
50	17739	4522	30	539	4279085	12,0	29,9	249,8	12,0	623,0
55	14741	4589	43	796	6223925	6,0	30,0	169,1	6,0	844,7
60	13483	4531	43	892	6878881	6,0	30,0	173,7	6,0	868,2
65	12948	4541	41	903	6746481	6,0	29,9	180,4	6,0	899,5
70	12343	4605	43	904	6967255	6,0	30,0	180,8	6,0	905,2

In sample 3, travel speed was kept constant. In this case, there was no change in the value of Ta. However, there was an increase in welding energy, as shown in Table 5.4.

Table 5.4 - Thermographic parameters and welding parameters obtained for sample 3.

Sample 3										
Position (mm)	Thermographic Data					Welding data acquired				
	T_p (un.)	T_b (un.)	T_w (pixels)	T_a (pixel²)	T_v (u.a.)	w_s (mm/s)	U_w (V)	I_w (A)	w_f (m/min)	Welding Energy (J/mm)
5	23126	4569	34	836	6550168	6,0	29,7	166,9	6,0	826,4
10	16239	4488	37	950	7267990	6,0	30,0	169,3	6,0	845,0
15	22090	4668	41	1056	8979127	6,0	29,9	187,7	6,0	934,4
20	16168	4739	42	1027	8171044	6,0	30,0	165,3	6,0	827,1
25	17790	4962	44	987	8687823	6,0	29,3	177,4	6,0	866,1
30	20851	4705	41	1020	8079270	6,0	30,1	234,8	10,3	1178,1
35	11466	4580	38	871	5652817	6,0	29,3	246,5	12,0	1202,1
40	12613	4594	39	940	6249875	6,0	29,3	237,9	12,0	1163,0
45	23266	4613	41	986	7819267	6,0	29,0	258,3	12,0	1247,9
50	23880	4584	41	989	7721161	6,0	29,3	244,9	12,0	1195,9
55	16621	4593	43	1062	8439358	6,0	29,9	174,1	7,7	868,0
60	18087	4588	43	1119	9475023	6,0	30,0	173,9	6,0	868,4
65	17141	4586	42	1094	9322964	6,0	29,9	177,3	6,0	884,7
70	16304	4581	43	958	7930689	6,0	30,0	172,6	6,0	862,3
75	14869	4642	44	887	7132757	6,0	30,0	178,7	6,0	892,2

5.1.2. Zone extensions

After preparation, the samples were analyzed using a confocal microscope and the mapping of the extension of FZ and sub divisions of HAZ was carried out. Measurements were taken in for all the zones described above (see Figure 4) every 5 mm along the longitudinal axis of the samples. The results of these measurements and the welding parameters collected by the interface are shown in Table 5.5, Table 5.6 and Table *5.7*.

Observing the values obtained for the extension of each zone in sample 1, the increase in travel speed and wire-feed speed, both in 2x, caused a reduction in thermal input. However, there was an increase in the extension of FZ and a reduction in the extension of CGHAZ and FGHAZ.

Table 5.5 - Measurements corresponding to sample 1.

Position (mm)	Sample 1									
	PROCESS INPUTS					PROCESS OUTPUTS				
	w_s (mm/s)	U_w (V)	I_w (A)	w_f (m/min)	H (J/mm)	FZ (µm) ↑	CGHAZ (µm) ↓	FGHAZ (µm) ↓	IHAZ (µm)	SHAZ (µm)
5	6.0	29.8	130.8	4.0	555.3	2515	556	442	703	2502
10	6.0	29.9	144.9	4.0	570.8	1855	1094	960	793	3011
15	6.0	29.9	150.2	4.0	521.2	2092	1195	794	939	2448
20	6.0	30.0	139.2	4.0	557.7	2520	1188	789	818	2015
25	10.3	30.0	137.0	5.1	308.8	2585	718	799	904	2324
30	12.0	29.5	204.1	8.0	389.1	3385	378	303	583	2989
35	12.0	30.0	209.1	8.0	377.7	3347	260	291	714	3033
40	12.0	30.8	206.1	8.0	373.9	2996	232	314	1320	2578
45	12.0	30.0	202.6	8.0	379.7	2725	303	265	720	3524
50	7.7	29.9	204.9	5.1	600.4	2031	1020	1000	779	3416
55	6.0	29.9	133.3	4.0	527.9	2110	979	714	889	3363
60	6.0	30.0	137.0	4.0	516.7	2115	228	1094	1091	3194
65	6.0	30.0	133.6	4.0	557.8	2131	754	522	970	3192

For sample 2, the wire-feed speed was initially raised to 6 mm/s. The increase in travel speed and wire-feed speed, both in 2x, caused an increase in thermal input. As a result, there was an increase in the FZ extension and a reduction in the extensions of CGHAZ e IHAZ. Sample 2 presented a greater extension of FZ due to the increase in the wire feed speed and of welding energy.

Table 5.6 - Measurements corresponding to sample 2.

Position (mm)	Sample 2									
	PROCESS INPUTS					PROCESS OUTPUTS				
	w_s (mm/s)	U_w (V)	I_w (A)	w_f (m/min)	H (J/mm)	FZ (µm) ↑	CGHAZ (µm) ↓	FGHAZ (µm) ↓	IHAZ (µm)	SHAZ (µm)
5	6.0	28.7	173.7	6.0	357.1	3685	465	318	573	2746
10	6.0	29.8	176.6	6.0	495.6	3706	611	733	453	2877
15	6.0	29.9	185.6	6.0	513.4	3691	502	505	783	1647
20	6.0	30.0	183.6	6.0	489.3	4907	723	463	1009	3442
25	6.0	30.0	172.2	6.0	493.1	6151	476	416	994	3254
30	12.0	29.8	235.1	12.0	494.0	4812	607	525	958	1511
35	12.0	30.0	250.3	12.0	772.1	4777	540	588	715	1479
40	12.0	29.9	249.7	12.0	773.7	4454	375	879	749	1502
45	12.0	29.9	252.2	12.0	803.0	3598	610	352	789	2717
50	12.0	29.9	249.8	12.0	806.4	3301	611	1050	825	1544
55	6.0	30.0	169.1	6.0	626.6	3627	718	747	800	1783
60	6.0	30.0	173.7	6.0	510.5	3445	640	864	941	2160
65	6.0	29.9	180.4	6.0	503.0	3329	635	770	1191	1914
70	6.0	30.0	180.8	6.0	486.7	2895	733	785	1415	1513

In sample 3, the 2x increase in wire-feed speed caused an increase in thermal input and, consequently, an increase in the FZ extension and a reduction in the CGHAZ and IHAZ extensions.

Table 5.7 - Measurements corresponding to sample 3.

Position (mm)	Sample 3									
	PROCESS INPUTS					PROCESS OUTPUTS				
	w_s (mm/s)	U_w (V)	I_w (A)	w_f (m/min)	H (J/mm)	FZ (µm)	CGHAZ (µm)	FGHAZ (µm)	IHAZ (µm)	SHAZ (µm)
5	6.0	29.7	166.9	6.0	554.9	4109	564	633	649	3060
10	6.0	30.0	169.3	6.0	650.6	4152	1019	1164	1271	1819
15	6.0	29.9	187.7	6.0	652.6	4507	1209	1546	1847	955
20	6.0	30.0	165.3	6.0	610.2	5087	1074	1364	1819	914
25	6.0	29.3	177.4	6.0	646.2	4833	1695	813	1639	1000
30	6.0	30.1	234.8	10.3	681.6	6600	739	1104	1454	754
35	6.0	29.3	246.5	12.0	839.5	5601	889	1364	730	1017
40	6.0	29.3	237.9	12.0	887.3	5141	814	1741	637	846
45	6.0	29.0	258.3	12.0	885.8	5399	790	1610	895	649
50	6.0	29.3	244.9	12.0	906.2	5574	804	1194	908	724
55	6.0	29.9	174.1	7.7	897.2	4747	839	1644	800	698
60	6.0	30.0	173.9	6.0	649.3	3701	995	1422	719	959
65	6.0	29.9	177.3	6.0	657.9	3561	1264	697	2317	589
70	6.0	30.0	172.6	6.0	660.8	3586	1104	1071	1908	573
75	6.0	30.0	178.7	6.0	645.8	3421	603	312	1573	1744

This behavior is in line with that observed in the literature, showing that the increase in welding energy tends to increase the dimensions of the HAZ. However, in the case of the materials and set of parameters used, no differences were found in the morphologies of the microstructures obtained, as will be demonstrated in the next section.

5.2. MICROSTRUCTURAL ANALYSIS

The base metal microstructure is shown in Figure 5.3. The presence of primary ferrite (equiaxed), PF, and pearlite, P, is observed with a proportion of approximately 76% and 24%, respectively.

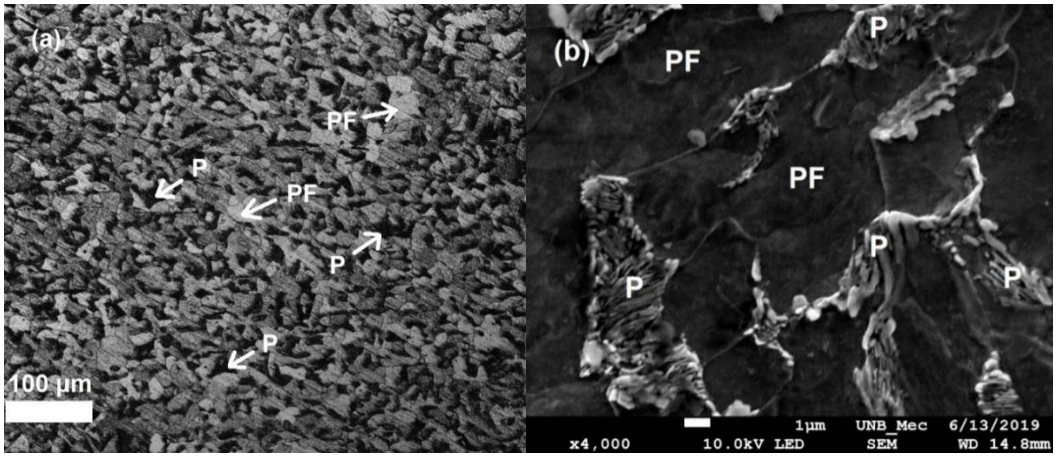

Figure 5.3 - (a) Optical microscopy (magnification 200x) and (b) scanning electron microscopy (magnification 4000x) of base metal in sample 1. Etching: Nital 5%. P = Pearlite, PF = Primary Ferrite

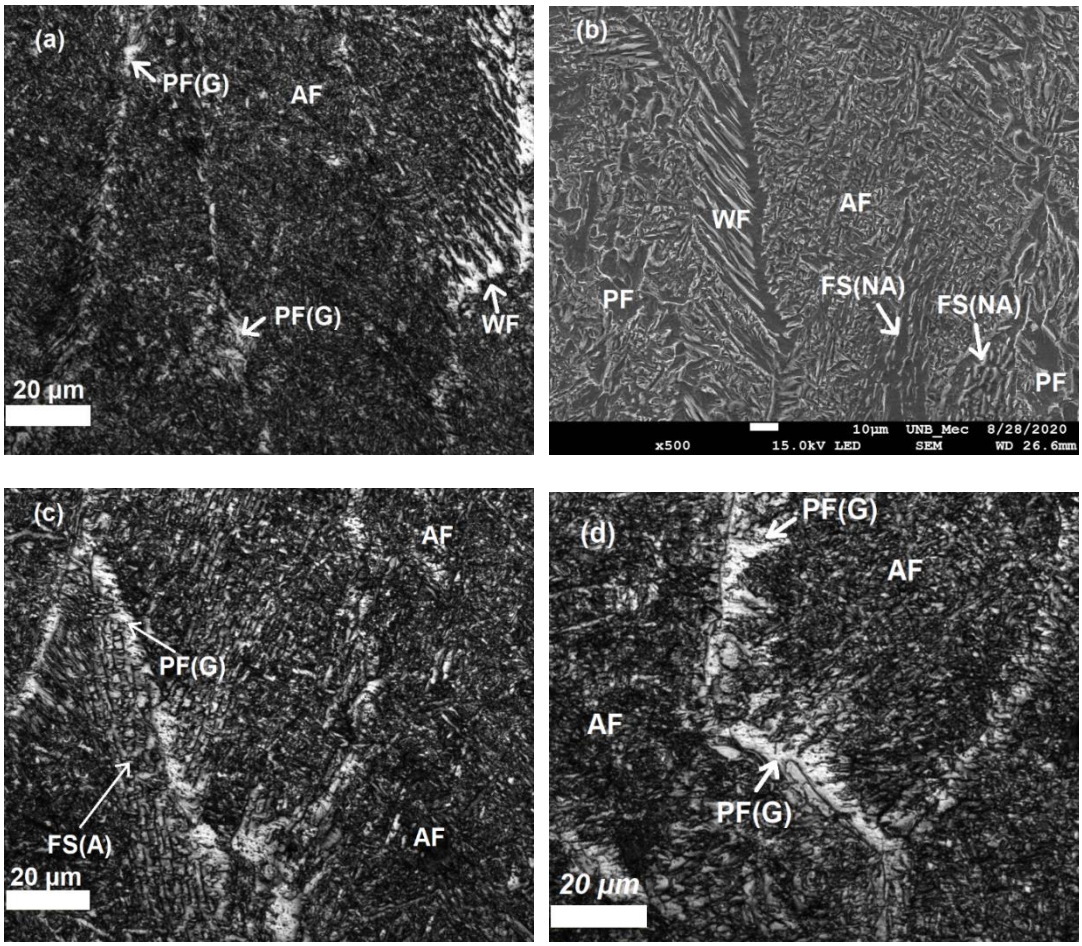

Figure 5.4 - Confocal microscopy (magnification 1000x) and SEM (magnification 500x) images from microstructures of FZ in sample 1 which 7a and 7b shows Widmanstätten Ferrite (WF) and Acicular Ferrite (AF). In 7b also is possible to identify presence of intragranular PF and Ferrite with Non-Aligned Second phase (FS(NA)). Figures 7c and 7d shows grain boundary ferrite (PF(G)) and AF. Etching: Nital 5%.

Weld microstructure is composed by grain boundary ferrite PF(G), acicular ferrite (AF) Widmanstätten ferrite (WF), ferrite with aligned second phase (FS(A)) and with non-aligned second phase (FS(NA)).

For many authors both bainite and Widmanstätten ferrite evolve from the same nucleus, the nucleation process being displacive with only carbon partitioning during the nucleation stage. The nucleus is only able to grow into bainite when diffusionless growth (with an adequate allowance for the stored energy of bainite) can be sustained at the transformation temperature; otherwise Widmanstätten ferrite forms (REES; BHADESHIA, 1994). This model is based in martensite nucleation theory - activation energy of nucleation is then predicted and found to vary linearly with chemical driving force - contrasts with classical nucleation theory, where activation energy of nucleation is inversely proportional to some power of the chemical driving force.

The nucleation mechanism for acicular ferrite is quite complex and has given rise to several studies in recent years. What can be gauged from this process is that it seems unlikely that the inclusion / austenite interface can in general be glissile and dissociate directly into an embryo of ferrite (REES; BHADESHIA, 1994). This does not, however, make a displacive nucleation process impossible because the dislocation debris generated in the austenite adjacent to the inclusion, perhaps due to differential thermal expansion effects, could provide the necessary arrays which might dissociate into appropriate embryos. Whatever the detailed issues at the inclusion/austenite interface, it would be extremely useful to be able to predict the acicular ferrite start temperature an experimentally access quantitative data on the thermodynamics of acicular ferrite nucleation. Rees and Bhadeshia (REES; BHADESHIA, 1994) demonstrated in their work the linear relationship between activation energy and driving force. It in turn implies that driving force at transformation start temperature should vary linearly with start temperature.

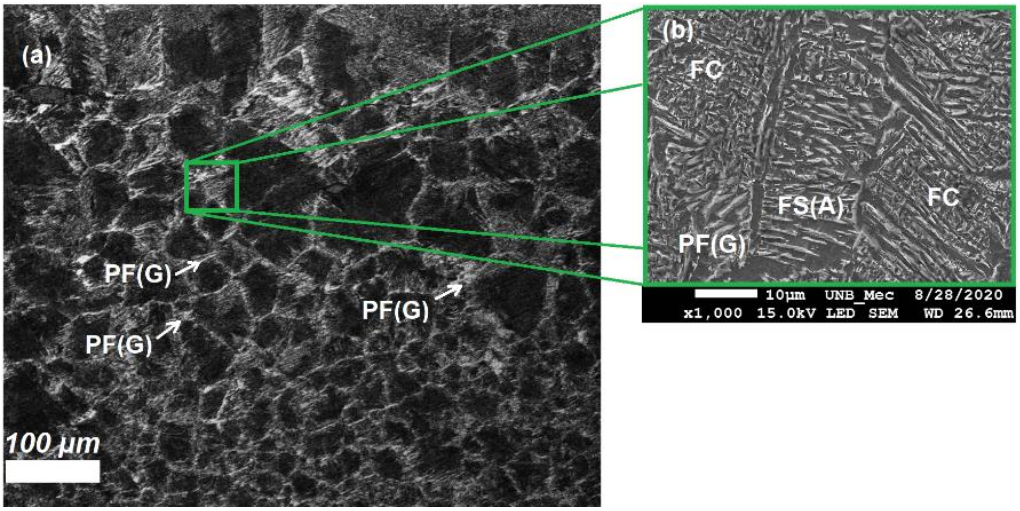

Figure 5.5 - Microstructure of CGHAZ in (a) optical microscopy at 200x and (b) SEM at 1000x showing formation of grain boundary ferrite (PF(G)), Ferrite with Aligned Second phase (FS(A)) and aggregate ferrite-carbide (FC). Etching: Nital 5%.

For HAZ, the microstructures observed are PF (primary and grain boundary), FS(NA), AF and pearlite. The phase balance in HAZ remained similar to the base metal although the morphology and grain size showed variations induced by the multiple cooling rates presented by the samples with the FZ distancing. Figure 5.5a and Figure 5.5b shows images of CGHAZ. Is possible to see presence of degenerate pearlite P(D), PF(G) and aggregate ferrite-carbide (FC) in large grain colonies.

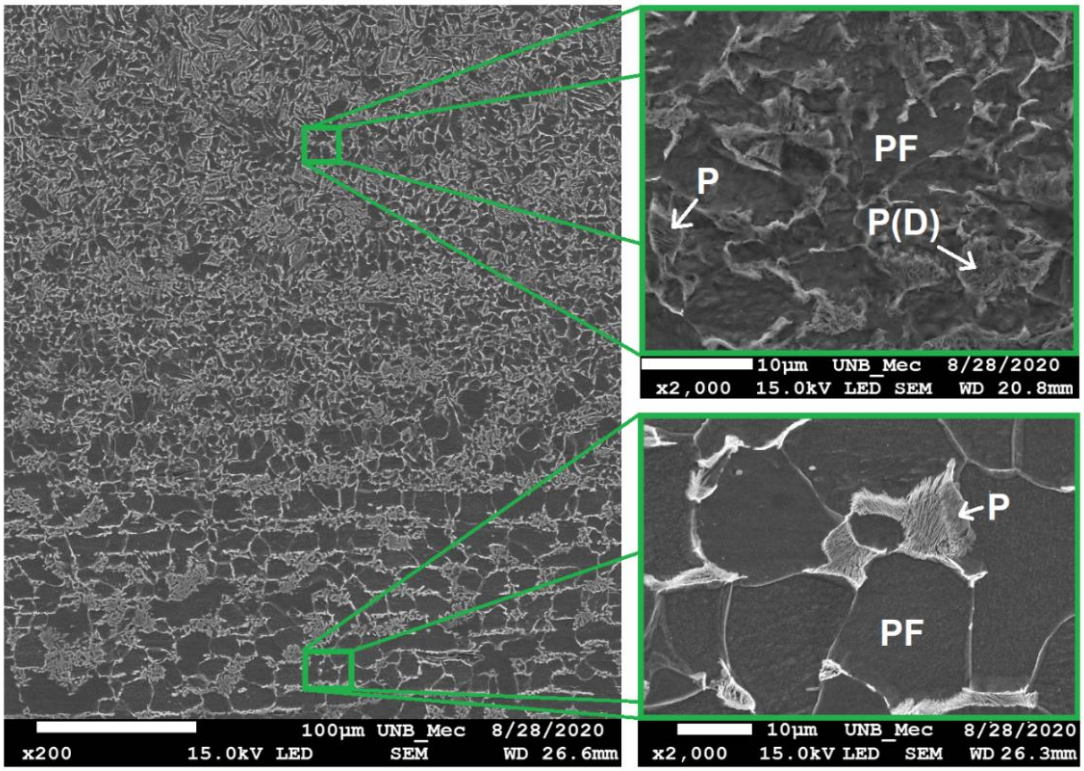

Figure 5.6 - SEM images of (a) boundary FGHAZ/IHAZ (with 200x ampliation), (b) FGHAZ and (c) IHAZ (2000x ampliation both). Etching: Nital 5%.

Figure 5.6 shows the microstructures of boundary FGAZ/IHAZ, FGHAZ and IHAZ. It is possible to observe the formation of P, P(D) and PF. The microstructure formed in CGHAZ and FGHAZ has apparently regions of degenerate pearlite well delimited by regions of acicular ferrite (AF). This is probably due to the phase transformation of the austenite (γ) to an acicular phase. In these parts of HAZ there might be an intense diffusional process of electrode wire alloying elements to the base metal.

With the removal of the fusion line, therefore, a reduction in fractions of acicular ferrite and degenerate perlite was observed in the microstructure of CGHAZ, FGHAZ and IHAZ. However, the fractions of perlite and primary ferrite increase with the removal of the melting line due to the greater temperature gradient to which the material is exposed. Higher temperature gradients provide less energy available for the process of nucleation of perlite grains, favoring the growth of grains through the diffusion of carbon atoms giving rise to orderly lamellae.

Figure 5.7 shows the microstructure of SHAZ. It basically consists of a ferritic matrix (PF) with fine pearlite grains (P). This morphology similar to that of the base metal was already expected because this region is the least affected by the heat of the process.

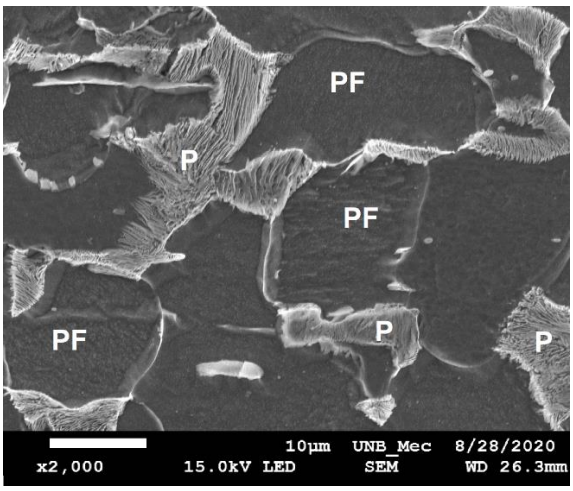

Figure 5.7 - SEM image of SHAZ (200x ampliation). Etching: Nital 5%.

5.3. X-RAY DIFFRACTION ANALYSIS

Figure 5.8a shows the XRD spectrum obtained for samples in three regions: FZ, CGHAZ and IHAZ. Three diffraction peaks can be observed, which are related to the planes (110), (200) and (211) of α-Fe (JCPDS 89-7194). The obtained spectrum indicates that no residual austenite was found, as observed in the microscopy analysis. However, as shown in Figure 5.8b, Figure 5.8c and Figure 5.8d, in comparison with IHAZ, the diffraction peaks for the regions show greater intensity and width. Furthermore, although there are no obvious changes in the intensities of α (200) and α (211), the intensity of the α (110) peak is significantly increased from the IHAZ region to CGHAZ and reaches its highest value for FZ. This is the result of the refinement of the grain presented by the microstructures of FZ and CGHAZ since they present the occurrence of AF. In general, the widening of the full width at half maximum (FWHM) results from a decrease in grain size and an increase in displacement density.

According to the relationship established by Bragg's law, increasing 2θ angle indicates an increase in the spacing of a pair of adjacent network planes, suggesting that the α-Fe phase network parameter was changed due to the increase in the content of solid solution elements throughout the α-Fe matrix during the deposition of the filler metal in FZ. Also, dislocations of the peaks can be associated to oxides formation in FZ.

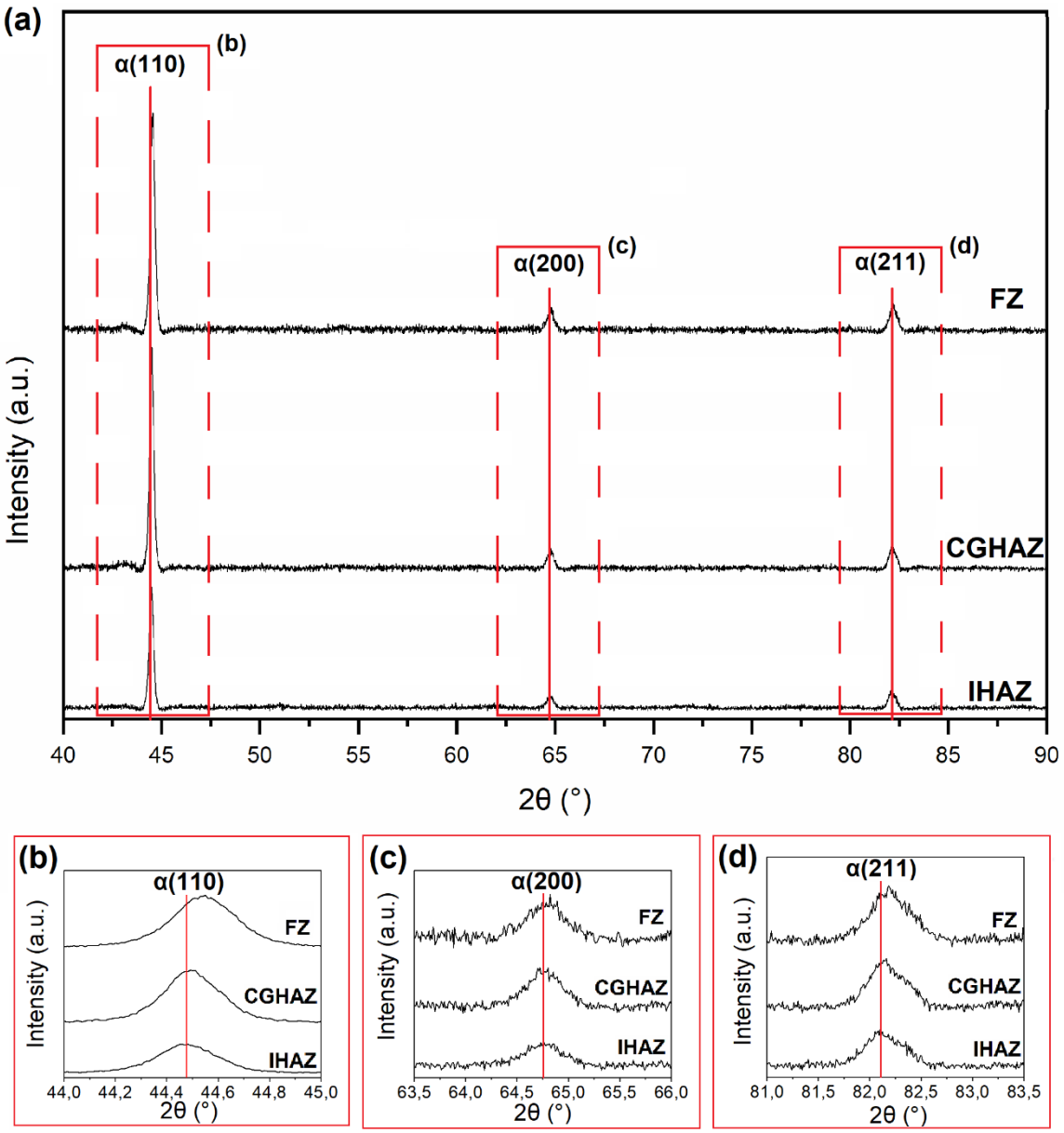

Figure 5.8 - Comparison of (a) full XRD spectra of FZ, CGHAZ and IHAZ, (b) α(110) peaks, (c) α(200) peaks and (d) α(211) peaks.

5.2. ANN ANALYSIS

In the present work, the test structure for the ANN algorithms described in the section was adopted, 560 different configurations were proposed for each of the models from A to F.

Tables 5.5 to 5.10 shows the results of the 10 algorithm configurations with the lowest MSE for each of the models from A to F.

Table 5.8 - Comparison between the 10 ANN algorithm configurations with lowest MSE for Model A.

1st Hidden Layer Size	2nd Hidden Layer Size	Training Method	Training Cycles	MSE			
				Overall Performance	Training	Test	LM Validation
15	14	BP	2	6,50E+03	2,87E-10	4,55E+04	-
12	14	BP	5	8,59E+03	1,01E-09	6,02E+04	-
18	15	LM	3	1,02E+04	9,40E+02	5,08E+04	1,61E+04
13	17	BP	4	1,23E+04	2,42E+03	7,16E+04	-
17	13	LM	3	1,38E+04	3,76E+03	3,28E+04	4,51E+04
12	13	BP	5	1,71E+04	9,85E-25	1,19E+05	-
15	12	LM	1	1,73E+04	3,77E+03	7,41E+04	2,84E+04
17	12	BP	2	1,74E+04	4,58E+02	1,19E+05	-
18	12	BP	1	1,86E+04	8,40E+03	8,00E+04	-
12	15	BP	3	1,92E+04	1,67E-09	1,34E+05	-

Table 5.9 - Comparison between the 10 ANN algorithm configurations with lowest MSE for Model B.

1st Hidden Layer Size	2nd Hidden Layer Size	Training Method	Training Cycles	MSE			
				Overall Performance	Training	Test	LM Validation
14	13	BP	4	2,94E+04	2,46E+04	5,82E+04	-
14	18	LM	5	3,03E+04	3,74E+02	1,28E+05	8,21E+04
17	13	LM	4	3,24E+04	3,53E+03	7,87E+04	1,30E+05
18	12	BP	4	3,30E+04	3,39E+04	2,79E+04	-
12	15	BP	4	3,32E+04	2,21E-09	2,32E+05	-
13	16	LM	4	3,32E+04	2,72E+03	1,70E+05	4,87E+04
18	12	LM	1	3,46E+04	1,25E+04	1,47E+05	3,27E+04
15	0	BP	2	3,54E+04	3,51E+04	3,74E+04	-
16	0	BP	4	3,72E+04	3,03E+04	7,85E+04	-
14	17	LM	2	3,93E+04	2,26E+04	7,58E+04	8,62E+04

Table 5.10 - Comparison between the 10 ANN algorithm configurations with lowest MSE for Model C.

1st Hidden Layer Size	2nd Hidden Layer Size	Training Method	Training Cycles	MSE			
				Overall Performance	Training	Test	LM Validation
14	13	LM	1	2,50E+04	1,43E+04	6,38E+04	3,97E+04
13	12	LM	3	2,80E+04	1,73E+03	4,69E+04	1,41E+05
18	17	BP	3	5,06E+04	4,65E+04	7,49E+04	-
12	17	LM	1	5,07E+04	1,79E+04	1,54E+05	1,12E+05
13	17	LM	3	5,25E+04	1,53E+04	1,37E+05	1,54E+05
12	14	BP	4	5,53E+04	4,67E+04	1,07E+05	
16	17	BP	4	5,55E+04	5,38E+04	6,58E+04	-
13	18	BP	1	5,64E+04	5,32E+04	7,58E+04	-
17	13	LM	2	5,68E+04	5,47E+02	3,37E+05	5,83E+04
15	14	BP	4	5,92E+04	4,63E+04	1,37E+05	-

Table 5.11 - Comparison between the 10 ANN algorithm configurations with lowest MSE for Model D.

1st Hidden Layer Size	2nd Hidden Layer Size	Training Method	Training Cycles	MSE			
				Overall Performance	Training	Test	LM Validation
14	14	LM	2	9,11E+04	5,60E+04	2,63E+05	9,46E+04
16	15	BP	3	1,08E+05	6,05E+04	3,96E+05	-
17	14	LM	2	1,09E+05	1,32E-15	7,38E+05	2,71E+04
17	17	LM	1	1,11E+05	4,21E+04	4,00E+05	1,69E+05
17	13	LM	4	1,16E+05	3,15E+03	4,16E+05	3,78E+05
17	12	LM	3	1,20E+05	4,56E+04	1,29E+05	4,86E+05
15	13	BP	1	1,22E+05	1,29E+05	7,60E+04	-
14	14	BP	2	1,33E+05	5,32E+04	6,12E+05	-
18	13	LM	5	1,34E+05	2,20E+04	7,41E+05	8,67E+04
13	13	BP	1	1,34E+05	5,36E+04	6,18E+05	-

Table 5.12 - Comparison between the 10 ANN algorithm configurations with lowest MSE for Model E.

1st Hidden Layer Size	2nd Hidden Layer Size	Training Method	Training Cycles	MSE			
				Overall Performance	Training	Test	LM Validation
16	14	LM	3	9,01E+04	2,43E+04	3,43E+05	1,66E+05
18	13	LM	2	1,15E+05	2,18E+04	2,52E+05	4,48E+05
17	14	BP	3	1,18E+05	7,56E+04	3,73E+05	-
18	18	BP	3	1,22E+05	6,36E+04	4,70E+05	-
18	12	BP	5	1,23E+05	1,30E+05	7,54E+04	-
13	17	BP	5	1,24E+05	1,24E+05	1,21E+05	-
15	17	BP	5	1,30E+05	1,24E+05	1,72E+05	-
16	0	BP	1	1,31E+05	1,02E+05	3,04E+05	
15	16	LM	3	1,40E+05	3,25E+04	1,39E+05	6,77E+05
12	14	LM	1	1,41E+05	1,71E+05	5,79E+04	7,88E+04

In model F is possible to observe that all the 10 first results with lower MSE has BR training mode.

Table 5.13 - Comparison between the 10 ANN algorithm configurations with lowest MSE for Model F.

1st Hidden Layer Size	2nd Hidden Layer Size	Training Method	Training Cycles	MSE			
				Overall Performance	Training	Test	LM Validation
17	15	BP	4	1,97E+04	1,08E-06	1,38E+05	-
17	16	BP	3	2,09E+04	3,89E-08	1,46E+05	-
18	14	BP	3	2,44E+04	3,00E-06	1,71E+05	-
15	14	BP	5	3,01E+04	2,73E-10	2,11E+05	-
15	15	BP	3	3,12E+04	1,04E-06	2,18E+05	-
16	13	BP	1	3,16E+04	5,34E-05	2,21E+05	-
14	12	BP	5	3,26E+04	4,23E-07	2,29E+05	-
12	13	BP	1	3,29E+04	3,71E-06	2,30E+05	-
14	18	BP	1	3,48E+04	2,38E-09	2,43E+05	-
17	14	BP	3	3,55E+04	6,71E-08	2,48E+05	-

A comparison of the best MSE value for each layer size combination is shown in Figure 5.9.

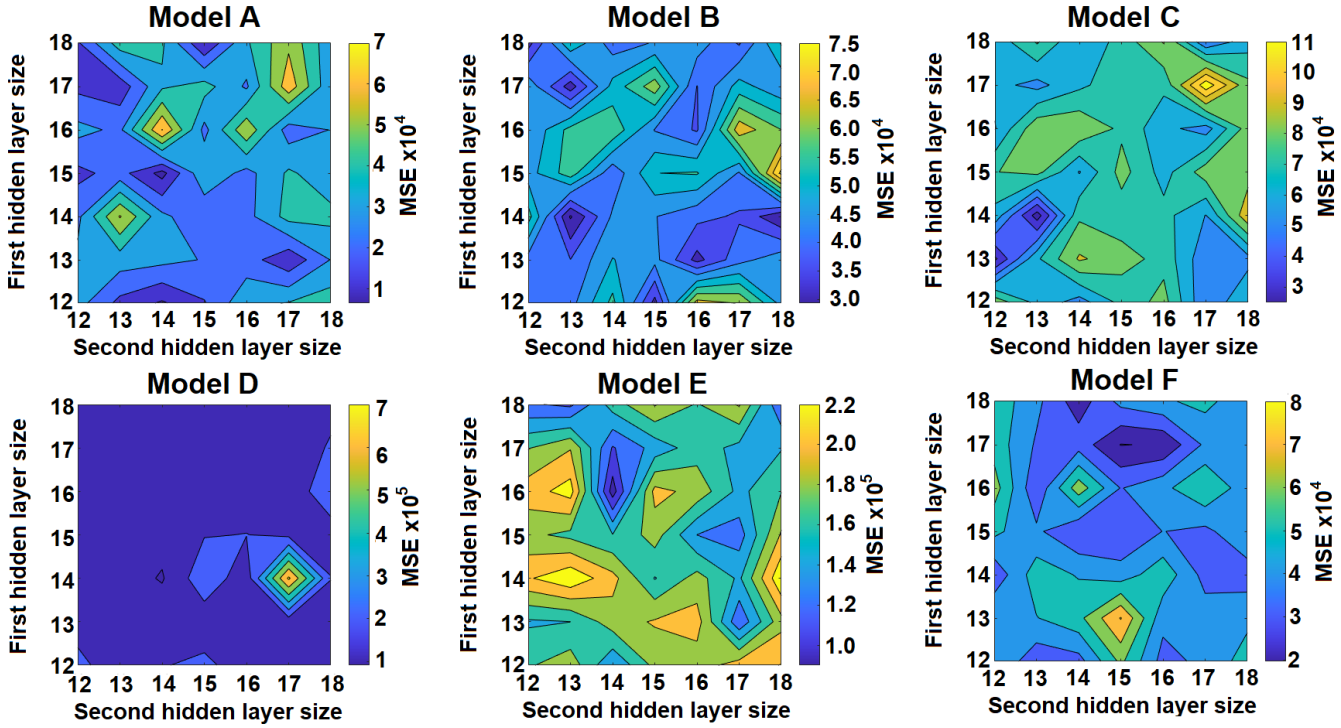

Figure 5.9 - ANN with best results (lower MSE value) in each combination of the size of hidden layers, changing the training method and training cycles

In addition to the MSE, the square root of the MSE, or Root of the Mean Square Error (RMSE), is commonly used to express the accuracy of the numerical results with the advantage that RMSE presents error values in the same dimensions of the analyzed variable. Table 5.14

shows the results with lower MSE and RMSE considering hidden layer sizes, training mode and retrain cycles for each model.

Table 5.14 – Configurations with lower MSE for each model.

Model	Zone	Hidden Layer 1	Hidden Layer 2	Training Mode	Number of Training	MSE (µm²)	RMSE (µm)
A	FZ	15	14	BR	2	6499	81
B	CGHAZ	14	13	BR	4	29395	171
C	FGHAZ	14	13	LM	1	25007	158
D	IHAZ	14	14	LM	2	91116	302
E	SHAZ	16	14	LM	3	90131	300
F	ALL	17	15	BR	4	19660	140

The values obtained from RMSE demonstrate that the modeling has a relevant error range in determining the CGHAZ and FGHAZ extensions. This was already expected since the formation of these regions occurs according to a chaotic and non-linear process of microstructural formation.

The lowest RMSE value was obtained for model A – FZ as output – which uses 15 and 14 neurons in the first and second hidden layers, respectively. This hidden layer combination showed lower RMSE for BR training mode and 2 training runs configuration.

However, model F – 5 zones as outputs – showed good fit with 17 and 15 neurons in the first and second hidden layers, respectively, and with BR training mode and 4 training runs. A scheme of the structure of model F is shown in Figure 5.10.

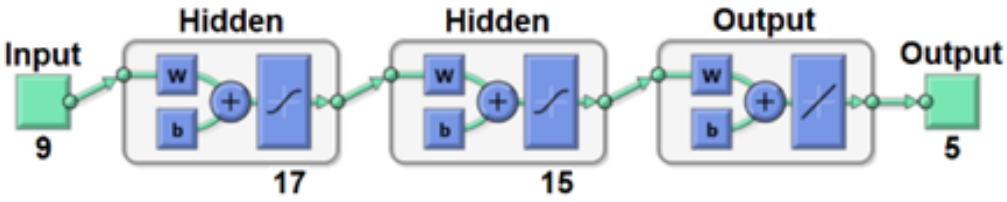

Figure 5.10 - Scheme of ANN structure of model F.

The training performance in Model F showed perfect correlation (see Figure 5.11). This fact confirms that the training method is effective and totally applicable for the estimation of the extension of each of the zones studied.

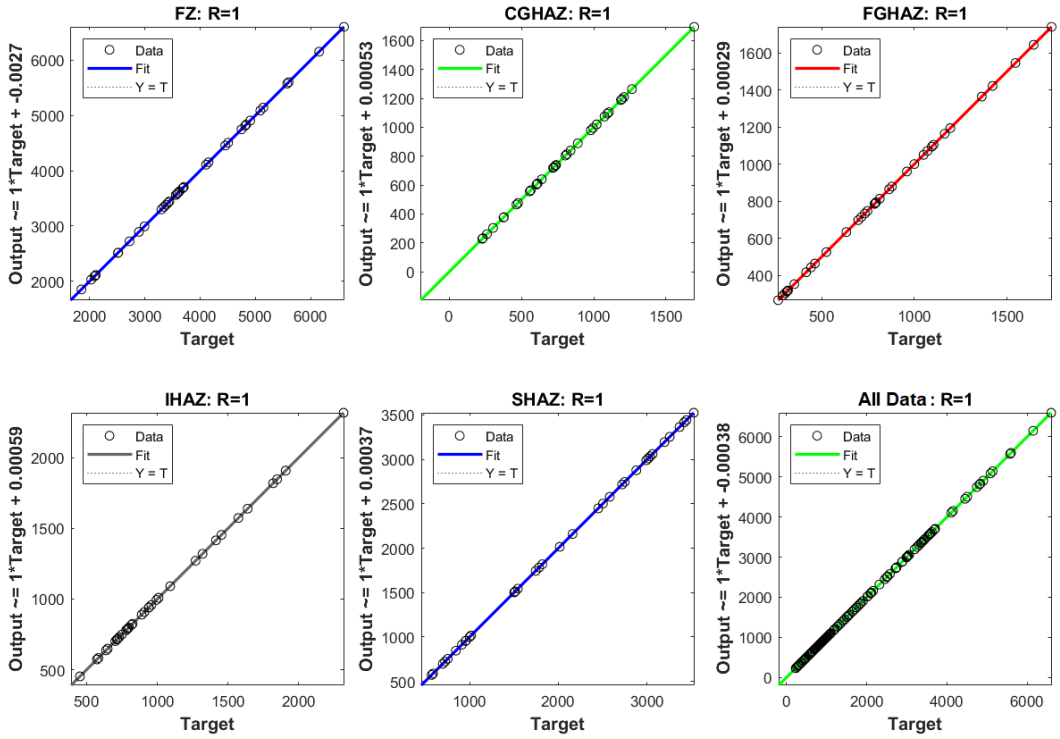

Figure 5.11 - Comparison of linear regressions of targets by variable relative to outputs in model F in training with 17 and 15 neurons in 1st and 2nd hidden layers, respectively.

The linear regressions relative to outputs for training and overall performance for model F is showed in Figure 5.12.

The F model is more advantageous than other single output models because it integrates the 5 outputs or model layers in a single model but with a similar structure. This model requires similar computing resources to estimate all 5 layers as individual models to estimate only one layer. It has 32 neurons in hidden layers, and the simpler models have 27 neurons. Another significant judgment to select this model is the fit (0.99472), which is better than CGHAZ (0.86041), FGHAZ (0.93911), IHAZ (0.92771) and SHAZ (0.99394), surpassed only by FZ (0.99681).

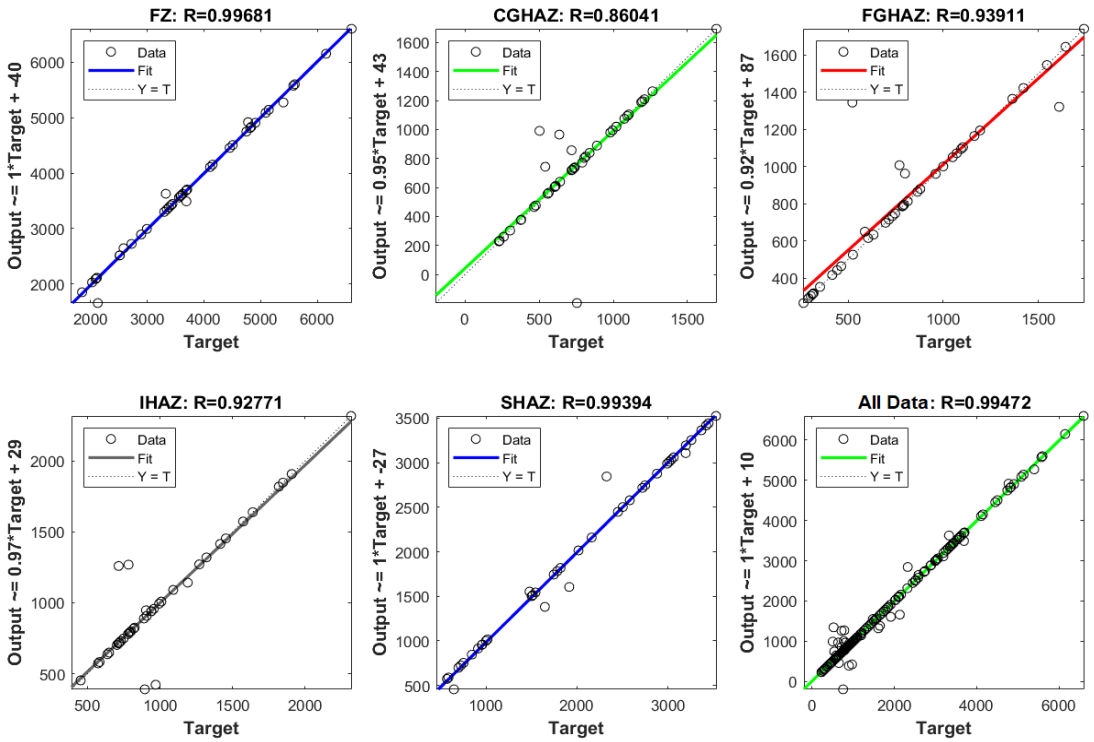

Figure 5.12 - Comparison of linear regressions of targets by variable relative to outputs in model F combining training and tests with 17 and 15 neurons in 1st and 2nd hidden layers, respectively.

Table 5.15 presents a comparison between the Overall Performance average, standard deviation, minimum, maximum and amplitude of RMSE values for all models from A to F.

Table 5.15 - Comparison between the standard deviation and the average, minimum and maximum MSE values for all models from A to F.

ANN Model	A	B	C	D	E	F
Average MSE Overall Performance (μm)	328,63	367,42	421,90	781,02	786,77	481,66
Standard Deviation (μm)	342,05	325,58	477,49	777,17	725,95	564,80
Minimum MSE (μm)	**80,62**	**171,46**	**158,11**	**301,83**	**300,17**	**140,36**
Maximum MSE (μm)	1113,55	1174,73	1962,14	2385,37	2224,86	2076,05
MSE Amplitude (μm)	1113,55	1187,43	1967,23	2404,16	2244,99	20, 78,46

The results found indicates that the model with lower RMSE values is Model A (except or the standard deviation, which presented the second lower RMSE). The standard deviation of all models indicates that there is a high dispersion for the RMSE values. This dispersion might be associated to the variations of precision in output estimation in the algorithms when the configurations of 1st and 2nd hidden layer sizes changes. This fact highlights the relevance of the results founds for the network configurations with lower RMSE value.

Table 5.16 shows the average errors relative to each zone for Model F. The final error of the model is about 12,9%, which represents a relatively good fit for estimation of zone

extents. However, model F is able to estimate the extent of FZ with an error of only 4% which represents a satisfactory result.

Table 5.16 - Comparison between the average errors relative to each zone for Model F.

Region	Sample 1 Avg. Error	Sample 2 Error	Sample 3 Error	Average Sample Error
FZ	5,6%	3,5%	3,0%	4,0%
CGHAZ	20,4%	23,8%	14,6%	19,6%
FGHAZ	22,0%	22,0%	11,9%	18,6%
IHAZ	16,2%	16,8%	11,0%	14,7%
SHAZ	4,8%	5,6%	12,9%	7,8%
Average microstructural error per sample	13,8%	14,3%	10,7%	12,9%

To obtain a more accurate result when estimating the FZ extension, Model A could be used in comparison to the result provided by Model F.

6. CONCLUSIONS

At the end of this work, the following conclusions can be expressed:

- Increasing the wire speed causes an increase in the FZ extension. This effect was observed even with the reduction of thermal input in sample 1. The increase in FZ tends to reduce the extension of CGHAZ, as was observed in all 3 samples.
- Microstructural analysis using SEM and XRD revealed that, apparently, there is no presence of residual austenite in the samples. In FZ the predominant phases are AF, PF(G) and WF, as expected for the material used. Initially, at CGHAZ, the presence of AF, PF and P (D) was verified. As the thermally affected zone moves away from the material, the fractions of AF and PD decrease as grains of P begin to appear and the presence of PF increases. In the IHAZ and SHAZ regions, only the presence of PF and P was found, which corroborates with the microstructure initially presented in base metal.
- Displacement in the diffraction peaks in XRD analyses indicates a possible increase in the lattice constant comparing FZ with IHAZ due to the higher content of Mn and Si. The displacements may also be associated with the formation of oxides. The reduction in the IHAZ peaks observed may be due to the increase in the average size of the PF grains in relation to the AF microstructure existing in the FZ and CGHAZ.
- The prediction of the extension of the FZ and HAZ regions in low-carbon and low-alloy steel welds was possible with the use of ANN modeling. The inputs of the neural network were defined as measurements of the total extension of each of the zones along the bead cross-section, operational parameters of the welding process as the travel speed, welding voltage, welding current and wire-feed speed. The thermographic peak, thermographic base, thermographic width, thermographic area and thermographic volume also are inputs. These characteristics were obtained by a thermographic image feature extraction algorithm.
- Then, such experimental data obtained were used to train and test the multi-layer backpropagation ANN algorithms in 6 different models named from A to F. Model F was considered the one with the most satisfactory results for microstructural estimation. The model A with 15 and 14 neurons in the 1st and 2nd hidden layers, respectively and Bayesian Regularization and 2 trainings configuration showed the lowest MSE value among all models. Nevertheless, model F gives all 5 zones as outputs and showed good results with 17 and 15 neurons in the 1st and 2nd hidden layers.

- Furthermore, it becomes more convenient to deal with a model that provides all 5 outputs instead of using 5 individual models in estimating the microstructure of the welded region.
- It is important to note that the modeling presented here is valid for the welding conditions established in the methodology of this work (composition of the alloys used, substrate dimensions and wire diameter, composition of the shielding gas, tension, variation of parameters in a short measurement interval). In addition, the applied methodology is valid for analyzes of microstructural evolution in the direction perpendicular to that of travel speed.
- The F model presents an overall error of approximately 12.9%, which is a result considered satisfactory considering the complexity of the modeling of the different regions of the microstructure. Furthermore, Model F presented an error of 4% in the modeling of the ZF extension, which represents a great adjustment of the adopted estimation model.

The use of this sensor fusion algorithm to processing the thermographic information and welding arc variables, allows a better understanding of microstructural characteristics of the welded joint, helping in the design and dimensioning of welded structures.

The results show that the modeling methodology to estimate the microstructure of the welded region, using the implementation of sensor fusion with ANN, is a valuable result to material area research and to process control.

7. FUTURE WORKS

The results presented in this work are extremely relevant to improve the understanding about the complexity of models for estimating the extent of molten zone and the heat affected zone in weld beads produced via GMA welding. However, some gaps have been observed which have deviated from the scope of this work and which may give rise to future work. In future researches, is intended:

a) Evaluate the impact of parameter changes during deposition on the transverse profile of the weld beads microstructure;

b) Carry out studies on the modeling of the microstructure of the initial and crater regions of the weld beads;

c) Carry out studies on the emission of IR radiation related to the formation of the microstructure at HAZ;

d) Carry out the modeling of the ZAC area with a cross section of the weld beads;

e) Apply the methodology presented in this study to a multipass welding process or wire-arc additive manufacturing.

BIBLIOGRAPHY

AHMED, A. A. M. Prediction of dissolved oxygen in Surma River by biochemical oxygen demand and chemical oxygen demand using the artificial neural networks (ANNs). **Journal of King Saud University - Engineering Sciences**, v. 29, n. 2, p. 151–158, 2017.

AI, Q.; ZHOU, Y.; XU, W. Adaline and its application in power quality disturbances detection and frequency tracking. **Electric Power Systems Research**, v. 77, n. 5–6, p. 462–469, 2007.

ANDRADE, A. L. DE. **Estabilidade microestrutural da liga AI – 2,4 Li – 1,2 Cu – 0,6 Mg – 0,12 Zr (8090) submetida a tratamentos de retrogressão e reenvelhecimento**. [s.l.] Pontifícia Universidade Católica do Rio de Janeiro, 2003.

BABU, S. S. The mechanism of acicular ferrite in weld deposits. **Current Opinion in Solid State and Materials Science**, v. 8, n. 3–4, p. 267–278, 2004.

BALASUBRAMANIAN, M.; JAYABALAN, V.; BALASUBRAMANIAN, V. Developing mathematical models to predict grain size and hardness of argon tungsten pulse current arc welded titanium alloy. **Journal of Materials Processing Technology**, v. 196, n. 1–3, p. 222–229, 2008.

BESTARD, G. A. **Sensor fusion and embedded devices to estimate and control the depth and width of the weld bead in real time**. [s.l.] Universidade de Brasília, 2017.

BESTARD, G. A. et al. Sensor fusion to estimate the depth and width of the weld bead in real time in GMAW processes. **Sensors (Switzerland)**, v. 18, n. 4, 1 abr. 2018.

BESTARD, G. A. Online Measurements in Welding Processes (Online First). In: [s.l.] IntechOpen, 2020. p. 1–23.

BESTARD, G. A.; ALFARO, S. C. A. Sensor Fusion: Theory review and applications. **23rd ABCM International Congress of Mechanical Engineering COBEM**, 2015.

BESTARD, G. A.; ALFARO, S. C. A. Propuesta de diseño de un sistema de control de la geometría del cordón en procesos de soldadura orbital. **Taller de Cibernética Aplicada TCA 2016**, p. 9, 2016.

BESTARD, G. A.; ALFARO, S. C. A. Measurement and estimation of the weld bead geometry in arc welding processes: the last 50 years of development. **Journal of the Brazilian Society of Mechanical Sciences and Engineering**, v. 40, n. 9, 2018.

BESTARD, G. A.; SAMPAIO, R. C.; ALFARO, S. C. A. Open loop control system and tools for data acquisition and estimation of the weld bead depth in GMAW process. **Proceedings XXII Congresso Brasileiro de Automática**, 2018.

BHADESHIA, H.; HONEYCOMBE, R. **STEELS: Microstructure and Properties**. 4. ed. [s.l.] Butterworth-Heinemann, 2017.

BHADESHIA, H. K. D. H. A rationalisation of shear transformations in steels. **Acta Metallurgica**, v. 29, n. 6, p. 1117–1130, 1981.

BHADESHIA, H. K. D. H. **Bainite in Steels - Transformations, Microstructure and Properties**. 2. ed. London: The University Press, Cambridge, 2001.

BHADESHIA, H. K. D. H. **Bainite in Steels - Theory and Practice**. 3. ed. London: Taylor and Francis Group, 2015.

BHADESHIA, H. K. D. H.; SVENSSON, L. E.; GRETOFT, B. A model for the development of microstructure in low-alloy steel (Fe-Mn-Si-C) weld deposits. **Acta Metallurgica**, v. 33, n. 7, p. 1271–1283, 1985.

BRACARENSE, A. Q.; MARQUES, P. V.; MODENESI, P. J. **Soldagem Fundamentos e Tecnologia**. [s.l: s.n.].

BRIEN, A. O. **Welding Handbook**. [s.l: s.n.]. v. 2

CALLISTER JR., W. D. **Ciência e Engenharia de Materiais - Uma Introdução**. 7th. ed. Rio de Janeiro: [s.n.].

CASTRO, R. S. DE. **Aspectos microestruturais e cristalográficos da ferrita acicular obtida por meio de sequencias termomecânicas em aço api 5l x-80**. [s.l: s.n.].

CHAN, B.; PACEY, J.; BIBBY, M. Modelling gas metal arc weld geometry using artificial neural network technology. **Canadian Metallurgical Quarterly**, v. 38, n. 1, p. 43–51, 1999.

CRUZ, J. A. G. **Uma Metodologia Para Modelagem E Controle Da Altura Do Reforço E Da Largura Do Cordão De Solda No Processo Gmaw**. [s.l.] Universidade de Brasília, 2014.

DE MIRANDA, H. C.; SCOTTI, A.; FERRARESI, V. A. Identification and control of metal transfer in pulsed GMAW using optical sensor. **Science and Technology of Welding and Joining**, v. 12, n. 3, p. 249–257, 2007.

EDWIN RAJA DHAS, J.; KUMANAN, S. Modeling and prediction of HAZ using finite element and neural network modeling. **Advances in Production Engineering & Management**, v. 8, n. 1, p. 13–24, 2013.

EROĞLU, M.; AKSOY, M.; ORHAN, N. Effect of coarse initial grain size on microstructure and mechanical properties of weld metal and HAZ of a low carbon steel. **Materials Science and Engineering A**, v. 269, n. 1–2, p. 59–66, 1999.

FLIR-SYSTEMS. **ThermoVision ™ A40 V Manual del usuario**. [s.l: s.n.].

FRANCO, F. D. **Monitorização e localização de defeitos na soldagem TIG através do sensoriamento infravermelho**. [s.l.] Universidade de Brasília, 2008.

GANJIGATTI, J. P.; PRATIHAR, D. K.; ROY CHOUDHURY, A. Global versus cluster-wise regression analyses for prediction of bead geometry in MIG welding process. **Journal of Materials Processing Technology**, v. 189, n. 1–3, p. 352–366, 2007.

GANJIGATTI, J. P.; PRATIHAR, D. K.; ROY CHOUDHURY, A. Modeling of the MIG welding process using statistical approaches. **International Journal of Advanced**

Manufacturing Technology, v. 35, n. 11–12, p. 1166–1190, 2008.

GUNARAJ, V.; MURUGAN, N. Prediction of heat-affected zone characteristics in submerged arc welding of structural steel pipes. **Welding Journal (Miami, Fla)**, v. 81, n. 3, 2002.

GUTIÉRREZ, P. H. et al. Thermo-mechanic and Microstructural Analysis of an Underwater Welding Joint. **Soldagem & Inspeção**, v. 21, n. 2, p. 156–164, 2016.

IBRAHIM, I. A. et al. The effect of Gas Metal Arc Welding (GMAW) processes on different welding parameters. **Procedia Engineering**, v. 41, n. Iris, p. 1502–1506, 2012.

IMC-SOLDAGEM. **Manual de Instruções Inversal 450/600**. Disponível em: <https://www.imc-soldagem.com.br/images/documentos/manuais/inversal_450-600_manual_instrucoes_2ed_(1998).pdf>. Acesso em: 14 mar. 2020.

IORDACHESCU, D. et al. Influence of shielding gases and process parameters on metal transfer and bead shape in MIG brazed joints of the thin zinc coated steel plates. **Materials and Design**, v. 27, n. 5, p. 381–390, 2006.

JORGE, J. C. F. et al. Influence of welding procedure and PWHT on HSLA steel weld metals. **Journal of Materials Research and Technology**, v. 8, n. 1, p. 561–571, 2019.

KARADENIZ, E.; OZSARAC, U.; YILDIZ, C. The effect of process parameters on penetration in gas metal arc welding processes. **Materials and Design**, v. 28, n. 2, p. 649–656, 2007.

KARSAI, G. et al. Neural network methods for the modeling and control of welding processes. **Journal of Intelligent Manufacturing**, v. 3, n. 4, p. 229–235, 1992.

KIM, I. S. et al. Sensitivity analysis for process parameters in GMA welding processes using a factorial design method. **International Journal of Machine Tools and Manufacture**, v. 43, n. 8, p. 763–769, 2003a.

KIM, I. S. et al. Sensitivity analysis for process parameters influencing weld quality in robotic GMA welding process. **Journal of Materials Processing Technology**, v. 140, n. 1- 3 SPEC., p. 676–681, 2003b.

KIM, I. S. et al. Optimal design of neural networks for control in robotic arc welding. **Robotics and Computer-Integrated Manufacturing**, v. 20, n. 1, p. 57–63, 2004.

KIM, I. S.; BASU, A.; SIORES, E. Mathematical models for control of weld bead penetration in the GMAW process. **International Journal of Advanced Manufacturing Technology**, v. 12, n. 6, p. 393–401, 1996.

KIM, Y. M.; LEE, H.; KIM, N. J. Transformation behavior and microstructural characteristics of acicular ferrite in linepipe steels. **Materials Science and Engineering A**, v. 478, n. 1–2, p. 361–370, 2008.

KOLHE, K. P.; DATTA, C. K. Prediction of microstructure and mechanical properties of multipass SAW. **Journal of Materials Processing Technology**, v. 197, n. 1–3, p. 241–

249, 2008.

LEE, J. I.; RHEE, S. Prediction of process parameters for gas metal arc welding by multiple regression analysis. **Proceedings of the Institution of Mechanical Engineers, Part B: Journal of Engineering Manufacture**, v. 214, n. 6, p. 443–449, 2000.

LIMA JÚNIOR, D. R. **Caracterização microestrutural e mecânica de juntas soldadas utilizando os processos GTAW, FCAW e SMAW**. [s.l.] Universidade Federal de Pernambuco, 2013.

MACHADO, I. G. **Soldagem e Técnicas Conexas: Processos**. [s.l: s.n.].

MANRICH, S.; ZANOTTO, E. D.; HAGE JR., E. Aplicabilidade da Teoria Clássica de Nucleação Modificada (CO-CNT) à Cristalização de Polímeros. **Polímeros Ciência e Tecnologia**, v. 2, n. 1, p. 15–20, 1992.

MEDEIROS, J. S. DE. **Bancos de Dados Geográficos e Redes Neurais Artificiais: Tecnologias de Apoio à Gestão do Território**. [s.l.] Universidade de São Paulo, 1999.

MENESES, L. Y. H.; SILVA, A. M. A.; ALFARO, S. C. A. Modeling and simulation of the metal transfer on GMAW-S process. **Journal of the Brazilian Society of Mechanical Sciences and Engineering**, v. 41, n. 12, 2019.

MODENESI, P. J. **Soldabilidade dos Aços Transformáveis**. Belo Horizonte: Universidade Federal de Minas Gerais, 2012. v. 1

MODENESI, P. J.; BRACARENSE, A. Q. **Introdução à Física do Arco Elétrico E sua Aplicação na Soldagem dos Metais**. Belo Horizonte: Universidade Federal de Minas Gerais - UFMG, 2004.

MODENESI, P. J.; MARQUES, P. V.; SANTOS, D. B. **Introdução à metalurgia da soldagem**. Belo Horizonte: UFMG, 2012.

MURUGAN, N.; PARMAR, R. S. Effects of MIG process parameters on the geometry of the bead in the automatic surfacing of stainless steel. **Journal of Materials Processing Technology**, v. 41, p. 381–398, 1994.

OLABI, A. G.; ALASWAD, A.; BENYOUNIS, K. Y. 6.06 – Mathematical Modeling of Weld Phenomena, Part 2: Design of Experiments and Optimization. 2014.

OLIVEIRA, B. F. DE. **Efeito dos tratamentos térmicos sobre a microestrutura e as propriedades de um aço ARBL microligado com estrutura bruta de solidificação**. Campos dos Goytacases: Universidade Estadual do Norte Fluminense Darcy Ribeiro, 2014.

PALANI, P. K.; MURUGAN, N. Development of mathematical models for prediction of weld bead geometry in cladding by flux cored arc welding. **International Journal of Advanced Manufacturing Technology**, v. 30, n. 7–8, p. 669–676, 2006.

PASQUA, N. H. **Sobre o Fenômeno da Nucleaçao**, 2003. Disponível em: <http://www.teses.usp.br/teses/disponiveis/76/76132/tde-09042008-090832/en.php>

PAULA, M. P. M. DE; MODENESI, P. J.; TRINDADE, V. B. Análise da Influência

de Parâmetros de Soldagem em Características Microestruturais e Mecânicas de Juntas Soldadas de um Tubo de Aço API X70Q para Aplicação Sour Service. **Soldagem & Inspeção**, v. 23, n. 2, p. 180–190, 2018.

PAVLYK, V.; DILTHEY, U. Simulation of weld solidification microstructure and its coupling to the macroscopic heat and fluid flow modelling. **Modelling and Simulation in Materials Science and Engineering**, v. 12, n. 1, 2004.

REES, G. I.; BHADESHIA, H. K. D. H. Thermodynamics of acicular ferrite nucleation. **Materials Science and Technology**, v. 10, p. 353–358, 1994.

RICKS, R. A.; HOWELL, P. R.; BARRITTE, G. S. The nature of acicular ferrite in HSLA stells weld metals. **Journal of Materials Science**, v. 17, p. 732–740, 1982.

SAVAGE, W. F.; LUNDIN, C. D.; ARONSON, A. H. Weld Metal Solidification Mechanics. **The Welding Journal**, v. 44, n. 4, p. 175–181, 1965.

SHAHIAND, A. S.; PANDEY, S. Welding current prediction in GMAW and UGMAW processes using response surface methodology. **Science and Technology of Welding and Joining**, v. 11, n. 3, p. 341–346, 2006.

SILVA, A. M. A. **Obtenção e Caracterização de Cerâmicas Porosas pelo Processo de Freeze Casting**. [s.l.] Universidade Federal de Minas Gerais, 2015.

SILVA, L. N. DE C. **Analise e sintese de estrategias de aprendizado para redes neurais artificiais**. Campinas: Universidade Estadual de Campinas, 1998.

SOARES, G. G. **Caracterização da junta dissimilar em solda de materiais do tipo estrutural e ARBL**. [s.l.] Universidade de Passo Fundo, 2015.

SOTELA, F. C. **Fusión de Datos Distribuida en Redes de Sensores Visuales Utilizando Sistemas Multi-Agente Federico Castanedo Sotela**. [s.l.] Universidad Carlos III de Madrid, 2010.

TANG, Z.; STUMPF, W. The role of molybdenum additions and prior deformation on acicular ferrite formation in microalloyed Nb-Ti low-carbon line-pipe steels. **Materials Characterization**, v. 59, n. 6, p. 717–728, 2008.

TEIXEIRA, G. S. **Análise da influência dos parâmetros de soldagem sobre a geometria do cordão de solda depositado pelo processo de soldagem TIG – MAG em tandem**. [s.l.] Universidade Federal do Rio Grande do Sul, 2011.

TERASAKI, H.; SIMPSON, S. W. Modelling of the GMAW system in free flight and short circuiting transfer. **Science and Technology of Welding and Joining**, v. 10, n. 1, p. 120–124, 2005.

THEWLIS, G. Materials perspective: Classification and quantification of microstructures in steels. **Materials Science and Technology**, v. 20, n. 2, p. 143–160, 2004.

THEWLIS, G.; WHITEMAN, J. A.; SENOGLES, D. J. Dynamics of austenite to ferrite phase transformation in ferrous weld metals. **Materials Science and Technology**, v.

13, n. 3, p. 257–274, 1997.

TOTTEN, G. E. **Steel Heat Treatment Handbook - Metallurgy and Technologies**. 2. ed. Portland: Taylor and Francis Group, 2006.

WU, J. et al. On achieving a better understanding of the polygonal ferrite microstructure in if steel using image quality analysis. **Materials and Manufacturing Processes**, v. 22, n. 2, p. 281–285, 2007.

XAVIER, P. P. S. **Efeitos de Diferentes Regiões Urbanas na Propagação de Sinais de Sistemas de Comunicações Pessoais Baseados em Redes de Satélites Não Geoestacionários**. [s.l.] Pontifícia Universidade Católica do Rio de Janeiro, 2005.

XIONG, J. et al. Modeling of bead section profile and overlapping beads with experimental validation for robotic GMAW-based rapid manufacturing. **Robotics and Computer-Integrated Manufacturing**, v. 29, n. 2, p. 417–423, 2013.

YANG, Z.; DEBROY, T. Modeling Macro-and Microstructures of Gas-Metal-Arc. **Metallurgical and Materials Transactions B**, v. 30, n. June, p. 483–493, 1999.

ZHANG, M. et al. Simulation of temperature distribution and microstructure evolution in the molten pool of GTAW Ti-6Al-4V alloy. **Materials**, v. 11, n. 11, 2018.